Rentao Mu

Construction and Reactivity of Pt-Based Bi-component Catalytic Systems

Springer

Springer Theses

Recognizing Outstanding Ph.D. Research

Aims and Scope

The series "Springer Theses" brings together a selection of the very best Ph.D. theses from around the world and across the physical sciences. Nominated and endorsed by two recognized specialists, each published volume has been selected for its scientific excellence and the high impact of its contents for the pertinent field of research. For greater accessibility to non-specialists, the published versions include an extended introduction, as well as a foreword by the student's supervisor explaining the special relevance of the work for the field. As a whole, the series will provide a valuable resource both for newcomers to the research fields described, and for other scientists seeking detailed background information on special questions. Finally, it provides an accredited documentation of the valuable contributions made by today's younger generation of scientists.

Theses are accepted into the series by invited nomination only and must fulfill all of the following criteria

- They must be written in good English.
- The topic should fall within the confines of Chemistry, Physics, Earth Sciences, Engineering and related interdisciplinary fields such as Materials, Nanoscience, Chemical Engineering, Complex Systems and Biophysics.
- The work reported in the thesis must represent a significant scientific advance.
- If the thesis includes previously published material, permission to reproduce this must be gained from the respective copyright holder.
- They must have been examined and passed during the 12 months prior to nomination.
- Each thesis should include a foreword by the supervisor outlining the significance of its content.
- The theses should have a clearly defined structure including an introduction accessible to scientists not expert in that particular field.

More information about this series at http://www.springer.com/series/8790

Rentao Mu

Construction and Reactivity of Pt-Based Bi-component Catalytic Systems

🐴 Springer

Author
Dr. Rentao Mu
Dalian Institute of Chemical Physics
Chinese Academy of Sciences
Dalian, Liaoning
China

Supervisors
Prof. Xinhe Bao
Dalian Institute of Chemical Physics
Chinese Academy of Sciences
Dalian, Liaoning
China

Prof. Qiang Fu
Dalian Institute of Chemical Physics
Chinese Academy of Sciences
Dalian, Liaoning
China

Supervisors' Foreword

As a core technology of modern chemical industry, catalysis has been involved in more than 80% of industrial processes and approximately 35% of global GDP. In such a process catalysts play the most important role, which alter reaction path of chemical processes, improve selectivity of aimed products and reduce the amount of by-products. In the past decades many works have been performed to rational design of highly efficient catalysts. The structural complexity of the supported nanocatalysts has impeded understanding of reaction mechanisms and identification of active sites. With the aid of modern surface science techniques, people can construct model catalytic systems with well-defined surface structure, understand the reaction mechanism at molecular level, and thus guide the rational design of practically supported catalysts.

This book focuses on surface catalysis studies in bimetallic catalysts, which is organized into seven chapters. Chapter 1 reviews recent developments of fundamental understanding of heterogeneous catalysis from single crystal surfaces to supported nanoparticle catalysts and also includes the motivation of this thesis. Chapter 2 describes applied surface science methods and techniques. In Chaps. 3 and 4, the correlation between the structure and catalytic performance of Pt–Ni bi-component catalysts are investigated. We find that the surface structure of Pt–Ni bi-component catalysts can be modulated by reduction and oxidation (redox) treatments. A "sandwich-like" structure with surface Ni(O) and subsurface metallic Ni shows the best reactivity for CO oxidation reaction at low temperature. Chapter 5 compares the reactivity and stability of Pt–Fe and Pt–Ni bi-component catalysts from model catalytic systems to supported nanoparticle catalysts. The confinement effect of single layer graphene on the surface chemistry of Pt catalyst is explored in Chap. 6. In the end Chap. 7 concludes the correlations between the structure and performance of Pt-based bi-component catalysts, including Pt–Fe, Pt–Ni and Pt-graphene.

On behalf of other authors, we sincerely acknowledge the efforts of editorial team to make this book printed and published. We sincerely hope that you would find this book useful in your research/professional endeavors.

Dalian, China   Prof. Xinhe Bao
January 2017   Prof. Qiang Fu

Parts of this thesis have been published in the following journal articles:

[1] **Rentao Mu**, Qiang Fu*, Li Jin, Liang Yu, Guangzong Fang, Dali Tan and Xinhe Bao*, Visualizing Chemical Reactions Confined Under Graphene, Angew. Chem. Int. Ed., 2012, (51):4856–4859

[2] **Rentao Mu**, Qiang Fu*, Hong Xu, Hui Zhang, Yuying Huang, Zhen Jiang, Shuo Zhang, Dali Tan and Xinhe Bao*, Synergetic Effect of Surface and Subsurface Ni Species at Pt-Ni Bimetallic Catalysts for CO Oxidation, J. Am. Chem. Soc., 2011, (133):1978–1986

[3] **Rentao Mu**, Xiaoguang Guo, Qiang Fu* and Xinhe Bao*, Oscillation of Surface Structure and Reactivity of PtNi Bimetallic Catalysts with Redox Treatments at Variable Temperatures. J. Phys. Chem. C, 2011, (115):20590–20595

[4] **Rentao Mu**, Qiang Fu*, Hongyang Liu, Dali Tan, Runsheng Zhai and Xinhe Bao*, Reversible Surface Structural Changes in Pt-based Bimetallic Nanoparticles During Oxidation and Reduction Cycles, Appl. Surf. Sci., 2009, (255):7296–7301

[5] Li Jin, Qiang Fu*, Hui Zhang, **Rentao Mu**, Yanhong Zhang, Dali Tan and Xinhe Bao, Tailoring the Growth of Graphene on Ru(0001) via Engineering of the Substrate Surface, J. Phys. Chem. C, 2012, (116):2988–2993

[6] Li Jin, Qiang Fu, **Rentao Mu**, Dali Tan and Xinhe Bao, Pb Intercalation Underneath a Graphene Layer on Ru(0001) and Its Effect on Graphene Oxidation, Phys. Chem. Chem. Phys., 2011, (13):16655–16660

[7] Teng Ma, Qiang Fu, Haiyan Su, Hongyang Liu, Yi Cui, Zhen Wang, **Rentao Mu**, Weixue Li, and Xinhe Bao, Reversible Structural Modulation of Fe-Pt Bimetallic Surfaces and Its Effect on Reactivity, ChemPhysChem, 2009, (10):1013–1016

[8] Yanhong Zhang, Qiang Fu, Yi Cui, **Rentao Mu**, Li Jin, and Xinhe Bao, Enhanced Reactivity of Graphene Wrinkles and Their Function as Nanosized Gas Inlets for Reactions under Graphene, Phys. Chem. Chem. Phys., 2013, (15):19042–19048

Acknowledgements

Contents

Chapter 1
Introduction

The rapid consumptions of coal, oil, and other fossil energies have resulted in globally environmental pollution and climate warming issues. As a core technology of modern chemical industry, catalysis is involved in more than 80% of the industrial processes and 60% of the products manufacturing. Therefore, the catalytic process is of great importance in the sustainable development of national economy, protection of environment, and public health [1, 2]. Catalysis, as an interdisciplinary science, includes the design, preparation, and characterization of catalysts, investigation of catalytic reaction mechanisms, and application of innovative catalytic theories in biomedicine, green chemistry, etc. Acting as a critical part of chemical industry, catalysts may alter the reaction path of chemical processes, improve the selectivity of aimed product, and reduce the amount of by-product. In order to achieve the environmental friendly catalytic reaction processes, many works are needed to be carried out on the reasonable and scientific design of efficient catalysts. However, the structural complexity of the supported nanoparticle catalysts has made the direct studies of their properties very challenging. As thus, the progress in heterogeneous catalysis is often hampered by the difficulties in understanding the reaction mechanisms and identifying the active sites. Fortunately, with the aid of modern surface science techniques, we can construct model catalytic systems with well-defined surface structures, understand the reaction mechanism at molecular level, and thus guide the rational design of practical supported catalysts.

1.1 Modulating the Performance of Heterogeneous Catalysts

1.1.1 Size Effect

Nanosized materials often exhibit novel physical and chemical properties when their sizes are reduced to a certain value (5 $\sim$ 50 nm). In general, size effect
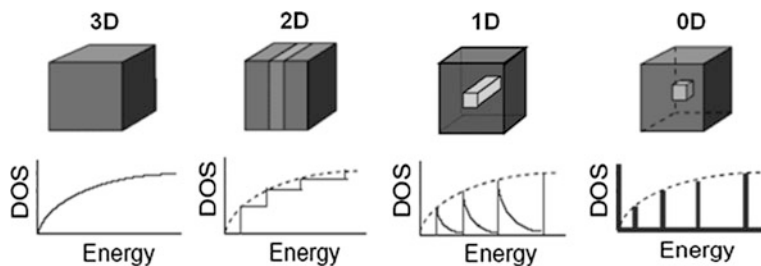
Fig. 1.1 Schematic diagram of energy level splitting as the size of solid material decreased from 3D bulk structure to 0D nanoparticle

includes surface effect and quantum size effect (QSE) [3]. Surface effect means that when the size of catalyst decreases the fraction of coordinatively unsaturated surface atoms increases. Quantum size effect was illustrated in Fig. 1.1. When the size of a solid material is decreased to the Fermi wavelength of electron, the movement of electron will be confined in a potential well, resulting in the discretion of energy level (Fig. 1.1). Therefore, the nanosized materials often show novel magnetic, optical, acoustic, thermal, electric, and other properties.

The size effect is also very important to heterogeneous catalysis, because the size of nanoparticles often influences the performance of heterogeneous catalysts [5, 6]. For example, Haruta et al. have found that the Au nanoparticles can catalyze CO oxidation below room temperature [7–10]. In contrast, bulk Au is a well-known chemically inert material. Goodman et al. have prepared model Au catalysts with different sizes on a planar $TiO_2(110)$ surface ($Au/TiO_2(110)$) [11]. As shown in Fig. 1.2, a significant size effect was observed on $Au/TiO_2(110)$ model system for CO oxidation reaction [4]. The TOF (turnover frequency) of CO oxidation reaction reached the maxima when the diameter of Au nanoparticles was 3 nm. STM results indicated that the 3 nm-Au nanoparticles exhibited bilayer structure [12].

Fig. 1.2 Catalytic activity for CO oxidation as a function of the Au particle size on $TiO_2(110)$ at 353 K, Reprinted with permission from Ref. [4]. Copyright (2006) American Chemical Society
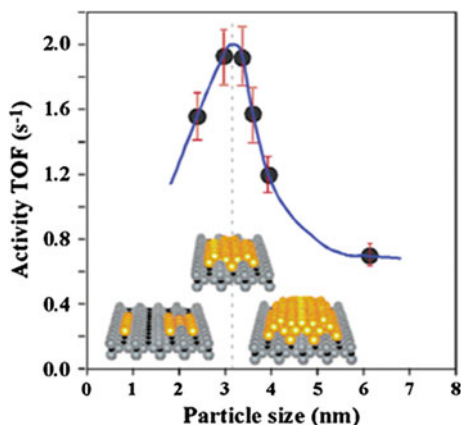
Subsequently, Hutchings et al. have studied practical Au/FeO_x catalyst and found the active structure was also Au bilayer structure [13]. This finding was well consistent with the results of model catalytic system.

Combination of $Au/TiO_2(110)$ model catalytic systems and supported Au/FeO_x catalysts demonstrated that the thickness of Au catalysts was a more important factor for CO oxidation reaction rather than the diameter of Au catalysts. Furthermore, the direct participation of Ti^{4+} in CO oxidation reaction was excluded by binding Au atoms on the top of Ti^{4+} sites [4]. DFT calculations have shown that Au nanoparticles provided the active sites for CO oxidation reaction [14]. It has been generally suggested that the catalytic activity of Au catalyst is derived from three main aspects: (1) coordinatively unsaturated surface Au atoms, (2) charge transfer between Au and substrate, and (3) quantum size effect of Au nanoparticle. But the relative proportion of these three factors in specific catalytic system is still not clear. For example, Freund et al. have investigated the CO adsorption on Au/FeO(111) model surface. By comparison with CO adsorption on the surface of bulk Au material, they found that the strong interaction of CO with Au nanoparticles can be attributed to the coordinatively unsaturated surface atoms rather than quantum size effect [15].

Another interesting example is the size effect of MoS_2 catalysts [16–18]. For nanosized catalysts, coordinatively unsaturated surface atoms often perform not only superior catalytic activity, but also high selectivity. Therefore, it is of highly importance to efficiently construct and characterize the surface structure of nanosized catalysts. Besenbacher et al. have prepared nanosized MoS_2 islands on Au(111) surface, which presented the tri-layer structure with one Mo layer sandwiched between two S layers [19]. They found that the edge termination of MoS_2 islands could be nicely modulated by the size of islands. As shown in Fig. 1.3, when the number of Mo edge atoms was <6, Mo atoms terminated the edge of MoS_2 nanosized islands. In contrast, when the number of Mo edge atoms was >6, S atoms terminated the edge of MoS_2 nanosized islands. When the number of Mo edge atoms was 6 (size = 1.5 nm), both situations have been observed. Hydrogen exposure of MoS_2 nanosized islands produced vacancies at different positions. For example, the vacancies were found at the corner sites of the MoS_2 triangle islands with the size of islands smaller than 1.5 nm. Increasing the size of MoS_2 nanosized islands to more than 1.5 nm, vacancies appeared on the straight edge shown in Fig. 1.3b, c. Subsequently, the authors studied the adsorption of dibenzothiophene (DBT) and found that DBT molecules were adsorbed on the vacancies at the corners, but not on those at straight edges. The reason should be attributed to the steric hindrance of vacancies at straight edge [16, 17]. This finding implies that very small (<1.5 nm) MoS_2 nanocatalysts may have high performance in hydrodesulfurization of fossil fuels.

In addition, the preparations and catalytic properties of Au_{55} [20–22], Pd_{20} [23, 24], Al_N-(N = 16, 17, 18) [25–27], Rh [28], Ru [29], Pt [30–32], nanocatalysts have been also studied. The above results show the size effect can often modulate
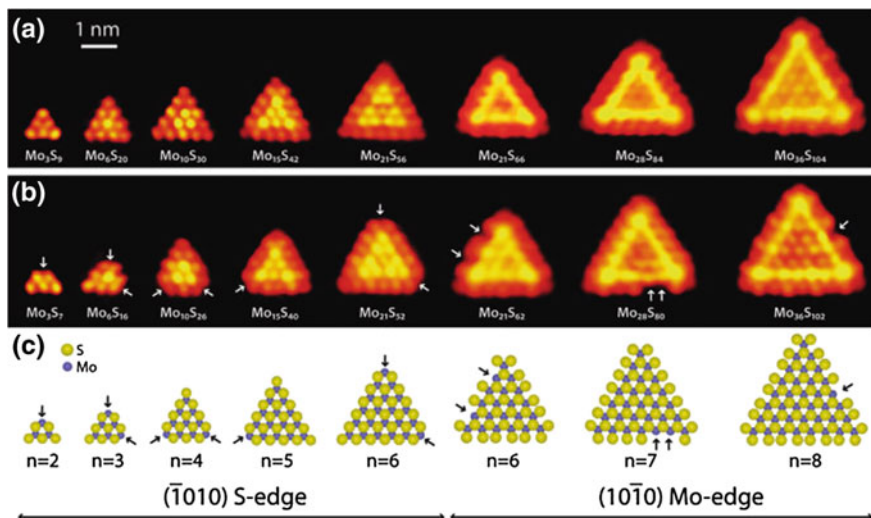
Fig. 1.3 **a** STM images of fresh MoS$_2$ nanoclusters before exposure to atomic hydrogen. Clusters with n < 6 expose the S edge termination, while clusters with n > 6 expose the Mo edge termination. **b** STM images of MoS$_2$ nanoclusters after exposure to atomic hydrogen at 300 K. The *arrows* indicate sulfur vacancies. **c** Ball models of the MoS$_2$ nanoclusters in (**b**). Reprinted with permission from Ref. [16]. Copyright (2010) American Chemical Society

the performances of nanosized catalysts. However, how to prevent these nanosized catalysts from sintering under working condition is still a big challenge in many catalytic processes.

1.1.2   Surface Structure

The heterogeneous catalytic reactions occur on the surface of catalysts, so the surface structure of catalysts significantly influences their catalytic performances. Investigating the correlation between surface structure and catalytic performance of heterogeneous catalysts can help to understand the reaction mechanism and design efficient catalysts.

Based on the development of modern surface science techniques in the 1960s, the molecular level understanding of the surface reactions has emerged [33–36]. For example, Ertl et al. and Somorjai et al. have made tremendous progress in the molecular level understanding of the reaction mechanism of NH$_3$ synthesis since Fritz Haber synthesized NH$_3$ from high pressure nitrogen and hydrogen over Os catalyst in 1908. In 2007, Ertl was awarded the Nobel Prize in Chemistry for his fundamental studies of chemical processes on solid surface, especially for the

molecular level understanding of reaction mechanisms of synthesis of NH_3 on Fe catalyst and the catalytic CO oxidation on Pt catalysts [37, 38].

Somorjai et al. have prepared clean Fe crystal with different surface structures under UHV condition, and studied the correlation between surface structure and catalytic performance [39–42]. They found that the Fe(111) crystal surface exhibited the highest reactivity. The reason has been attributed to the highest concentration of seven-coordinated (C_7) Fe atoms on Fe(111) plane, which were the active sites for NH_3 synthesis [43]. Mittasch and co-workers have also prepared highly efficient α-Fe(111) structure for NH_3 synthesis by reducing Fe_3O_4 catalyst [44]. Ertl et al. studied the dissociative adsorption rate of N_2 molecules on different Fe surfaces and found that the dissociative adsorption rate of N_2 on Fe(111) surface was hundred times higher than that on (110) surface [45, 46]. Their results were well consistent with the work by Emmett and Brunauer, where the dissociation of N_2 molecules had been determined to be the rate-determining step for NH_3 synthesis [47].

The progress in heterogeneous catalysis requires the molecular level understanding of reaction mechanism and preparation of highly efficient catalysts [48–51]. In recent decades, extensive efforts have been made to prepare shape-controlled nanocatalysts and understand the shape effect on catalytic performance.

For example, the shape effect of Pt on the activity and selectivity of pyrrole and benzene hydrogenation was studied first from model catalytic systems [52–55]. Hydrogenation of benzene to cyclohexane has been observed on Pt(100) crystal surface, while both cyclohexene and cyclohexane were produced on Pt(111) surface [52, 56]. Subsequently, Somorjai and Yang et al. prepared uniform cubic and cuboctahedral Pt nanoparticles, as shown in Fig. 1.4. TEM images revealed that the cubic Pt nanoparticles exposed only (100) surface, while cuboctahedral Pt nanoparticles exposed both (100) and (111) surfaces. Interestingly, hydrogenation of benzene to cyclohexane was observed over cubic Pt nanoparticles, whereas both cyclohexene and cyclohexane were generated over cuboctahedral Pt nanoparticles. This finding was well consistent with the results of model catalytic systems [57]. El-Sayed's group and Xia's group have also conducted many pioneering works on the shape control of nanoparticles [58–61].

Recently, Shen et al. have synthesized Co_3O_4 nanorods, which showed superior CO oxidation reactivity at low temperature [62, 63]. HR-TEM characterization revealed that the concentration of (110) surface on Co_3O_4 nanorods was higher than that on nanoparticles. Shen et al. suggested that the Co_3O_4(110) surface provided active Co^{3+} sites for CO adsorption and thus promoted CO oxidation reaction.

Currently, how to efficiently synthesize new and useful catalysts with high activity, selectivity, and stability is still very challenging in heterogeneous catalysis. Therefore, the investigations of model catalytic system, computational chemistry, preparation methods of nanocatalysts, and in situ characterization are called to work together to promote environmental friendly catalysis [64, 65].
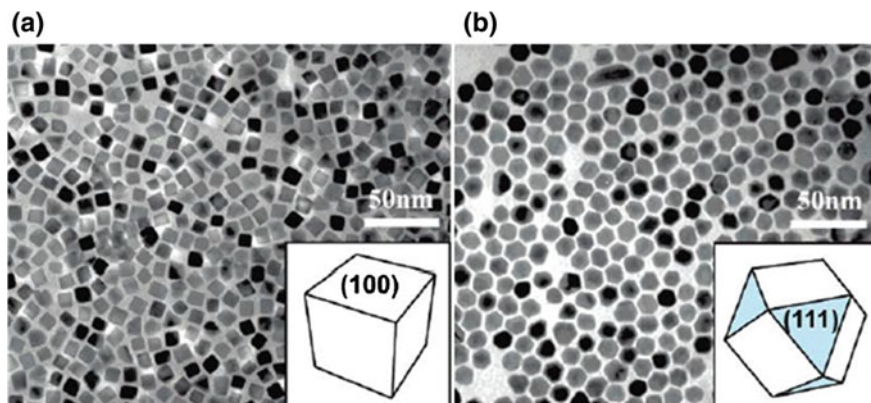
Fig. 1.4 TEM images of **a** TTAB-stabilized Pt cubic particles (average size: 12.3 ± 1.4 nm, 79% cubes, 3% triangles and 18% irregular shape) and **b** TTAB-stabilized Pt cuboctahedral particles (average size: 13.5 ± 1.5 nm, 90% cuboctahedra and 10% irregular shape). Adapted with permission from Ref. [52]. Copyright (2007) American Chemical Society

1.1.3   Support Effect

In order to prepare practical supported catalysts and reduce the usage of noble metal components, we often utilize various supports to stabilize and disperse the active components. Generally, the effects of support include, (1) reducing the usage of noble metal components and the cost of catalysts, (2) improving the mechanical strength of catalysts, (3) promoting the activity and selectivity of catalysts, and (4) improving the stability of catalysts. In this section, the support effect on the activity, selectivity, and stability of catalysts will be discussed.

In 1978, Tauster and co-workers studied the adsorption laws of H_2 and CO on Group-VIII noble metal catalysts [66]. They first time found that the strong interaction between metal catalysts and reducible oxide support (strong metal-support interaction, SMSI) could result in the distinct adsorption behaviors of H_2 and CO. This is because the SMSI often induces the charge and mass transfer between metal catalysts and reducible oxide support, which may further influence the performance of catalysts [67–69].

As shown in Fig. 1.5, charge transfer behavior can be observed between Au catalysts and different supports [4, 70]. Depositing Au on MgO(100) surface with high concentration of defects leads to the formation of negatively charged Au species ($Au^{\delta-}$). According to Blyholder model, the adsorbed CO molecules donate isolated electron pair to the empty d orbital of metal and form σ bond, meanwhile the d electrons of metal atoms are fed back to the empty $2\pi^*$ orbital of CO and form π bond [71, 72]. So the feedback of more charges to empty $2\pi^*$ orbital of adsorbed CO induces the lower shift of vibration frequency of C–O bond. In contrast, the vibration frequency of C–O bond shifts to higher wavenumber on positively charged $Au^{\delta+}$ surface.

Fig. 1.5 The stretching frequencies of CO adsorbed at Au catalysts on different supports. Reprinted with permission from Ref. [4]. Copyright (2006) American Chemical Society
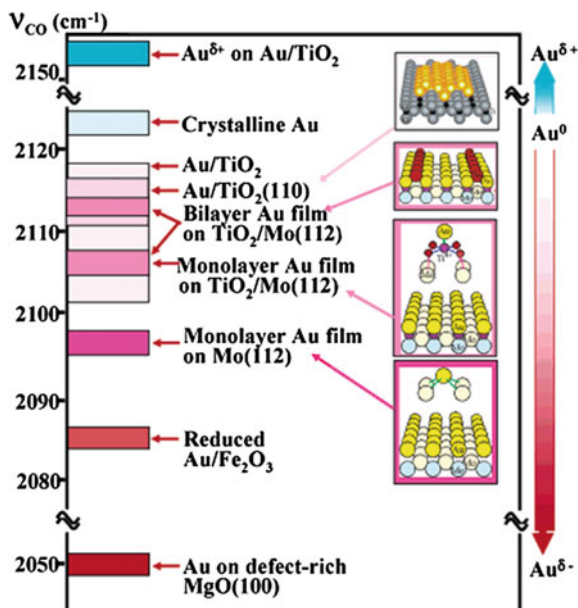
Recently, Hensen et al. prepared Rh nanoparticles on different oxide supports and observed distinct CO oxidation reactivity on these catalysts [73]. When the size of Rh nanoparticles was smaller than 2.5 nm, the reactivity of CO oxidation was highly dependent on the type of oxide supports, $Rh/SiO_2 < Rh/ZrO_2 < Rh/CeZrO_2 < Rh/CeO_2$. When the size of Rh nanoparticles was larger than 4 nm, the reactivity of CO oxidation was independent of the type of oxide supports. In previous studies, the oxide formed on the surface of Rh nanoparticles has been suggested to be the active species for CO oxidation reaction [51, 74]. EXAFS characterization revealed that the Rh nanoparticles with the size smaller than 2.5 nm were easily oxidized in CO oxidation reaction. The reducible oxide supports, such as $CeZrO_2$ and CeO_2, play a critical role in stabilizing oxidized nanoparticles and thus promoting CO oxidation reaction. However, Rh nanoparticles with the size larger than 4 nm maintained metallic state in CO oxidation reaction. So their reactivity was not influenced by the type of oxide supports.

It is well known that the reactivity of pure MgO, Al_2O_3, TiO_2 and many other oxide supports is very low, but the promotion effect of these oxides is significant for a variety of catalytic reactions [75]. Therefore, the so-called inverse model catalysts are prepared by depositing oxide (in the form of cluster, island, or film) on metal crystal surfaces [75–78]. Recently, Bao's group found that Pt–Fe bicomponent catalysts showed high reactivity and selectivity of CO oxidation in excess H_2 [77]. Surface science studies combined with DFT calculations revealed that the edge structures of interface-confined FeO_{1-X} nanoislands provided the active sites for O_2 dissociative adsorption, which resolved the CO poisoning problem of Pt surface at room temperature. By comparison, FeO_X was also prepared on HOPG surface. As

expected, the weakly interfacial interaction between FeO_X and HOPG surface resulted in the formation of 3D FeO_X clusters [76].

Similarly, the electrocatalytic reactivity of MoS_2/Au(111) model systems increased linearly with the edge length of 2D MoS_2 nanoislands, indicating the edge structures of MoS_2 nanoislands were active sites for electrocatalytic reaction [79].

Rodriguez et al. also prepared 2D CeO_{2-X} and TiO_{2-X} nanoislands on Au(111) surface which showed high water-gas shift reactivity [75]. These examples illustrated that the strong metal-oxide interfacial interaction could stabilize active oxide species, whereas the earlier works had mainly focused on how oxide supports promote the performance of noble metal catalysts.

At present, the studies of support effect mainly focus on two aspects. First, the molecular and atomic level understanding of support effect and rational synthesis of efficient catalyst support systems. Second, development and application of new and useful supports, such as perovskite type oxides, [80–82] carbon nanotubes, [83, 84] graphene related materials, [85, 86] silicon carbide, etc.

1.1.4   Promotion Effect of Secondary Components

In order to improve the performance of metal catalysts, the secondary components are often added, forming bicomponent catalysts. Compared to mono-component catalysts, bicomponent catalysts often exhibit novel electronic properties, superior reactivity and better structural stability [87, 88]. Therefore, bicomponent catalysts are widely used in petrochemical industry, fuel cell, air purification, automobile exhaust treatment, just to name a few.

Norskov et al. have proposed "*d*-band center" theory of transition metal (TM) catalysts, which provided a useful guidance for interpreting the bond formation and distinct activity of TM catalysts (Fig. 1.6) [90, 91]. They suggested that the *s* band of all TMs was half filled and broad in metallic state, so the differences for the interaction between metal *s* band and absorbate was very small from one metal to another. The distinct reactivity of various TMs should be primarily derived from their *d* states.

Fig. 1.6 Schematic illustration of the formation of chemical bond between the adsorbate valence level and the *s* and *d* states of a TM surface. From Ref. [89]. With permission of Springer
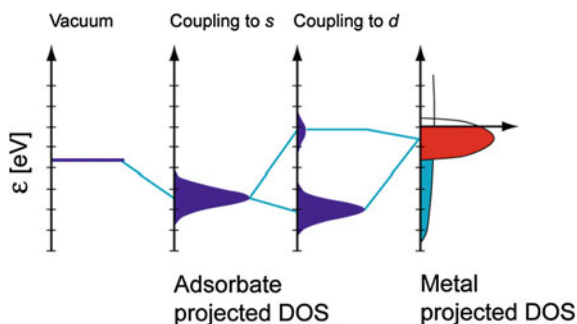
The d-band center of TMs can be influenced by electronic effect [92] and geometric effect [93, 94]. In practical catalytic processes, it is difficult to distinguish the relative contribution of electronic effect and geometric effect. Over model systems, Jakob et al. have deposited Pt layers onto Ru(0001) substrate and studied the electronic effect and geometric effect of Ru(0001) substrate on the catalytic properties of Pt layer [95]. Note that we will further discuss Pt-based bimetallic systems in Chap. 3.

The structures of bimetallic catalysts contain alloy, core–shell and side by side, [96–98] which often exhibit superior catalytic performance [98–101]. For example, alloyed Au–Ni catalysts showed high water-gas shift reactivity [102]. In model Au–Ni(111) system, STM results showed that the alloyed Au–Ni surface was formed by depositing Au atoms onto Ni(111) [102]. Since electrons transferred from Au to Ni, Ni atoms appeared bright in STM images. DFT calculations indicated that the surface-alloyed Au–Ni structure largely suppressed the coke formation, and thus maintained high performance for long time [102]. Furthermore, alloyed Pd–Au bimetallic catalysts were also found to perform high selectivity in the oxidation process of alcohol to aldehyde [87].

For catalytic CO oxidation in excess H_2, the core–shell Ru (Rh, Pd, Ir)-Pt catalysts exhibited significantly higher reactivity and selectivity than alloyed and monometallic structure [96, 103]. The reason has been attributed to the presence of subsurface 4d or 5d TMs, which altered the position of d-band center of surface Pt atoms and thus weakened the interaction between molecules and Pt surface. Mavrikakis et al. have found the activation energy of $CO + O \rightarrow CO_2$ elementary reaction on Pt-skin surface (0.41 eV) was much lower than that on Pt(111) surface (0.79 eV) [96, 103]. Li et al. have found that subsurface 3d TM could also lower the activation energy of $CO + O \rightarrow CO_2$ elementary reaction on Pt-skin surface [104].

Chen et al. have conducted DFT calculations and found subsurface 3d TM induced the d-band center of surface Pt atoms further away from Fermi level and promoted the performance of Pt catalysts (Fig. 1.7) [105]. For example, the ORR reactivity of Pt-skin surface with subsurface Ni was 90 times higher than that of commercial Pt/C catalyst [106]. Because the subsurface Ni weakened the interaction between adsorbates and Pt surface and thus provided more empty sites for O_2 dissociative adsorption [106]. The core–shell structural Pd–Pt catalyst also performed high ORR reactivity. The presence of Pd core enhanced the reactivity of Pt shell. On the other hand, the Pt shell improved the stability of Pd core in electrochemical processes. The synergetic effect of Pd core and Pt shell could enhance the reactivity and stability [98]. In addition, Pt catalysts with subsurface Fe or Co also showed superior ORR reactivity [107–109]. Furthermore, Pt-skin structure with subsurface Cu performed higher WGS reactivity than pure Pt(111) surface [110].

For the side-by-side Pt–Au bimetallic catalysts, since the nearby Au clusters increased the oxidation potential of Pt catalyst and stabilized Pt catalyst, and since the Pt surface provided the active sites for O_2 dissociative adsorption, the Pt–Au bimetallic nanoparticles showed high ORR performance [111].
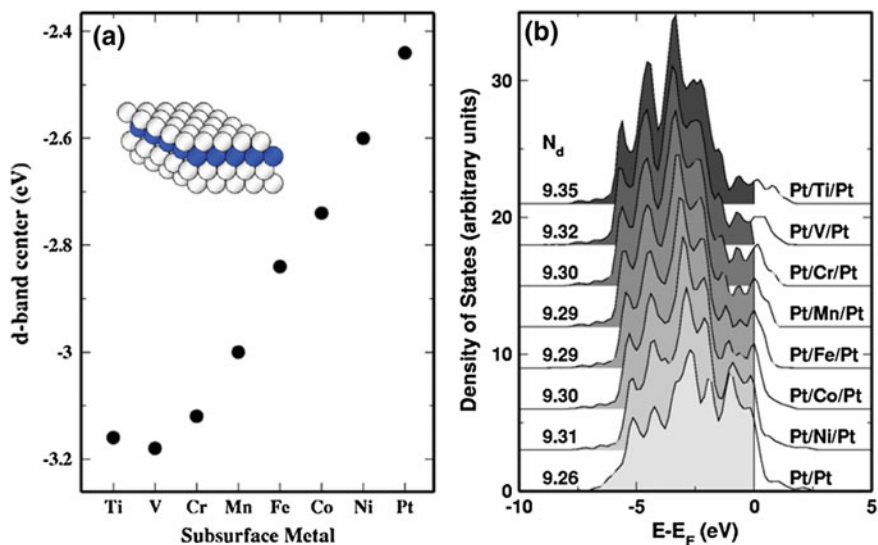
Fig. 1.7 a Changes of the surface d-band center of Pt slabs with different subsurface 3d TM.
b Calculated surface d-band DOS of Pt slabs containing subsurface 3d TM. The number of
d-electrons/surface atom is also shown. Reprinted from Ref. [105]. Copyright (2008), with
permission from Elsevier

1.2   Motivation and Conception of Thesis

Bicomponent catalysts with various structures often show superior performance in
CO oxidation, hydrogenation and dehydrogenation reactions, ORR, etc. Due to
their superior performances and wide applications, Pt-based bicomponent catalysts
have attracted more and more research interests from model catalytic system to
practical supported nanoparticles. But it is still difficult to establish the active
structures and understand the reaction mechanism of Pt-based bicomponents cata-
lysts under real working conditions, especially for Pt-3d TM catalysts. In this thesis,
we are attempting to understand the structure–performance correlation of Pt cata-
lysts modified with various secondary components from model catalytic systems to
supported nanoparticles.

(1) Constructing various Ni–Pt(111) model catalytic systems and understanding the
    correlation between surface structure and CO oxidation reactivity.
(2) Modulating the surface structure and reactivity of supported PtNi nanoparticle
    catalysts by reductive and oxidative (redox) treatments at different tempera-
    tures. Illustrating the correlation between redox temperature, surface structure
    and performance over supported PtNi nanoparticle catalysts.

(3) Studying the similarity and difference between Pt–Fe and Pt–Ni catalysts from model catalytic systems to supported nanoparticle catalysts.

(4) Modifying Pt(111) surface with single layer graphene and studying the confinement effect of graphene cover for surface reaction.

References

1. Ertl G et al (2008) Handbook of Heterogeneous Catalysis, 2nd edn, Wiley-Vch
2. Rothenberg G (2008) Catalysis: concepts and green applications. Wiley-Vch
3. Roduner E (2006) Size matters: why nanomaterials are different. Chem Soc Rev 35 (7):583–592
4. Goodman DW, Chen MS (2006) Catalytically active gold: from nanoparticles to ultrathin films. Acc Chem Res 39(10):739–746
5. Van Santen RA (2009) Complementary structure sensitive and insensitive catalytic relationships. Acc Chem Res 42(1):57–66
6. Bond GC (1991) Supported metal-catalysts—some unsolved problems. Chem Soc Rev 20 (4):441–475
7. Haruta M, Date M (2001) Advances in the catalysis of Au nanoparticles. Appl Catal A-gen 222(1–2):427–437
8. Hutchings GJ, Haruta M (2005) A golden age of catalysis: a perspective. Appl Catal A Gen 291(1–2):2–5
9. Haruta M (1997) Size- and support-dependency in the catalysis of gold. Catal Today 36 (1):153–166
10. Xu Q et al (2009) Au@ZIF-8: CO oxidation over gold nanoparticles deposited to metal-organic framework. J Am Chem Soc 131(32):11302−+
11. Goodman DW, Chen MS (2004) The structure of catalytically active gold on titania. Science 306(5694):252–255
12. Valden M, Lai X, Goodman DW (1998) Onset of catalytic activity of gold clusters on titania with the appearance of nonmetallic properties. Science 281(5383):1647–1650
13. Kiely CJ et al (2008) Identification of active gold nanoclusters on iron oxide supports for CO oxidation. Science 321(5894):1331–1335
14. Remediakis IN, Lopez N, Norskov JK (2005) CO oxidation on rutile-supported au nanoparticles. Angew Chem Int Edit 44(12):1824–1826
15. Lemire C et al (2004) Do quantum size effects control co adsorption on gold nanoparticles? Angew Chem Int Edit 43(1):118–121
16. Besenbacher F et al (2010) Size threshold in the dibenzothiophene adsorption on MoS_2 nanoclusters. ACS Nano 4(8):4677–4682
17. Besenbacher F et al (2007) Size-dependent structure of MoS_2 nanocrystals. Nat Nanotechnol 2(1):53–58
18. Lauritsen JV et al (2004) Hydrodesulfurization reaction pathways on MoS_2 nanoclusters revealed by scanning tunneling microscopy. J Catal 224(1):94–106
19. Besenbacher F et al (2000) Atomic-scale structure of single-layer MoS_2 nanoclusters. Phys Rev Lett 84(5):951–954
20. Lambert RM et al (2008) Selective oxidation with dioxygen by gold nanoparticle catalysts derived from 55-atom clusters. Nature 454(7207):981–983
21. Boyen HG et al (2002) Oxidation-resistant gold-55 clusters. Science 297(5586):1533–1536
22. Schmid G (2008) The relevance of shape and size of Au_{55} clusters. Chem Soc Rev 37 (9):1909–1930

23. Anderson SL et al (2009) Electronic structure controls reactivity of size-selected Pd clusters adsorbed on TiO_2 surfaces. Science 326(5954):826–829

24. Anderson SL et al (2010) Size-dependent oxygen activation efficiency over $Pd_n/TiO_2(110)$ for the CO oxidation reaction. J Am Chem Soc 132(38):13097–13099

25. Castleman AW et al (2009) Complementary active sites cause size-selective reactivity of aluminum cluster anions with water. Science 323(5913):492–495

26. Weiss PS et al (2011) Soft-landing deposition of Al_{17}^- on a hydroxyl-terminated self-assembled monolayer. J Phys Chem C 115(13):5373–5377

27. Leuchtner RE, Harms AC, Castleman AW (1991) Aluminum cluster reactions. J Chem Phys. 94(2):1093–1101

28. Hensen EJM, Ligthart DAJM, van Santen RA (2011) Influence of particle size on the activity and stability in steam methane reforming of supported Rh nanoparticles. J Catal 280 (2):206–220

29. Park JY et al (2010) Size effect of ruthenium nanoparticles in catalytic carbon monoxide oxidation. Nano Lett 10(7):2709–2713

30. Roduner E et al (2006) A small paramagnetic platinum cluster in an nay zeolite: characterization and hydrogen adsorption and desorption. J Phys Chem B. 110(5):2013–2023

31. Niesz K, Grass M, Somorjai GA (2005) Precise control of the Pt nanoparticle size by seeded growth using $EO_{13}PO_{30}EO_{13}$ triblock copolymers as protective agents. Nano Lett 5 (11):2238–2240

32. Shao-Horn Y et al (2009) Pt nanoparticle stability in PEM fuel cells: influence of particle size distribution and crossover hydrogen. Energy Environ Sci 2(8):865–871

33. Somorjai GA, Li YM (2011) Impact of surface chemistry. Proc Natl Acad Sci 108 (3):917–924

34. Somorjai GA (2000) The development of molecular surface science and the surface science of catalysis: berkeley contribution. J Phys Chem B. 104(14):2969–2979

35. Yates JT, Campbell CT (2011) Surface chemistry: key to control and advance myriad technologies. Proc Natl Acad Sci 108(3):911–916

36. Sinfelt JH (2002) Role of surface science in catalysis. Surf Sci 500(1–3):923–946

37. Ertl, G. (1980) surface science and catalysis—studies on the mechanism of ammonia-synthesis—the Emmett, P.H. award address. Catal Rev 21(2):201–223

38. Ertl G (2008) Reactions at surfaces: from atoms to complexity (nobel lecture). Angew Chem Int Edit 47(19):3524–3535

39. Spencer ND, Schoonmaker RC, Somorjai GA (1981) Structure sensitivity in the iron single-crystal catalyzed synthesis of ammonia. Nature 294(5842):643–644

40. Spencer ND, Schoonmaker RC, Somorjai GA (1982) Iron single-crystals as ammonia-synthesis catalysts—effect of surface-structure on catalyst activity. J Catal 74 (1):129–135

41. Somorjai GA (1994) The surface science of heterogeneous catalysis. Surf Sci 299(1–3): 849–866

42. Somorjai GA, Kim CM, Knight C (1992) Building of complex catalysts on single-crystal surfaces. Surf Sci Catal 482:108–129

43. Strongin DR et al (1987) The importance of C_7 sites and surface-roughness in the ammonia-synthesis reaction over iron. J Catal 103(1):213–215

44. Mittasch A (1950) Early studies of multicomponent catalysts. Adv Catal 2:81–104

45. Bozso F et al (1977) Interaction of nitrogen with iron surfaces.1. Fe(100) and Fe(111) J Catal 49(1):18–41

46. Bozso F, Ertl G, Weiss M (1977) Interaction of nitrogen with iron surfaces.2. Fe(110). J Catal. 50(3):519–529

47. Emmett PH, Brunauer S (1934) The Adsorption of Nitrogen by Iron Synthetic Ammonia Catalysts. J Am Chem Soc 56:35–41

48. Lee I, Zaera F (2005) Selectivity in platinum-catalyzed cis-trans carbon-carbon double-bond isomerization. J Am Chem Soc 127(35):12174–12175

49. Zaera F et al (2008) Synthesis of heterogeneous catalysts with well shaped platinum particles to control reaction selectivity. Proc Natl Acad Sci 105(40):15241–15246
50. Somorjai GA, Li YM (2010) nanoscale advances in catalysis and energy applications. Nano Lett 10(7):2289–2295
51. Somorjai GA, Park JY (2008) Molecular factors of catalytic selectivity. Angew Chem Int Edit 47(48):9212–9228
52. Somorjai GA et al (2007) Platinum nanoparticle shape effects on benzene hydrogenation selectivity. Nano Lett 7(10):3097–3101
53. Somorjai GA, Rupprechter G (1999) Molecular studies of catalytic reactions on crystal surfaces at high pressures and high temperatures by infrared-visible Sum Frequency Generation (SFG) surface vibrational spectroscopy. J Phys Chem B 103(10):1623–1638
54. Englisch M, Jentys A, Lercher JA (1997) Structure sensitivity of the hydrogenation of crotonaldehyde over Pt/SiO2 and Pt/TiO2. J Catal 166(1):25–35
55. Somorjai GA et al (2006) Sum frequency generation vibrational spectroscopic and high-pressure scanning tunneling microscopic studies of benzene hydrogenation on Pt(111). J Am Chem Soc 128(39):12810–12816
56. Somorjai GA, Bratlie KM, Kliewer CJ (2006) Structure effects of benzene hydrogenation studied with sum frequency generation vibrational spectroscopy and kinetics on Pt(111) and Pt(100) single-crystal surfaces. J Phys Chem B. 110(36):17925–17930
57. Yang PD et al (2006) Morphological control of catalytically active platinum nanocrystals. Angew Chem Int Edit 45(46):7824–7828
58. Ahmadi TS et al (1996) Shape-controlled synthesis of colloidal platinum nanoparticles. Science 272(5270):1924–1926
59. Wang ZL, Ahmad TS, ElSayed MA (1997) Steps, edges and kinks on the surfaces of platinum nanoparticles of different shapes. Surf Sci 380(2–3):302–310
60. El-Sayed MA, Narayanan R (2004) Shape-dependent catalytic activity of platinum nanoparticles in colloidal solution. Nano Lett 4(7):1343–1348
61. Xia Y et al (2009) Shape-Controlled synthesis of metal nanocrystals: simple chemistry meets complex physics? Angew Chem Int Edit 48(1):60–103
62. Xie XW et al (2009) Low-Temperature Oxidation of CO Catalysed by Co3O4 Nanorods. Nature 458(7239):746–749
63. Xie XW, Shen WJ (2009) Morphology control of cobalt oxide nanocrystals for promoting their catalytic performance. Nanoscale 1(1):50–60
64. Norskov JK et al (2009) Towards the computational design of solid catalysts. Nat Chem 1(1):37–46
65. Henry CR (1998) Surface studies of supported model catalysts. Surf Sci Rep 31(7–8):235–325
66. Tauster SJ, Fung SC, Garten RL (1978) Strong metal-support interactions—Group-8 noble-metals supported on TiO2. J Am Chem Soc 100(1):170–175
67. Tauster SJ (1987) Strong metal-support interactions. Acc Chem Res 20(11):389–394
68. Newton MA et al (2007) Dynamic in situ observation of rapid size and shape change of supported Pd nanoparticles during CO/NO cycling. Nat Mater 6(7):528–532
69. Fu Q, Wagner T (2007) Interaction of nanostructured metal overlayers with oxide surfaces. Surf Sci Rep 62(11):431–498
70. Goodman DW, Chen MS (2008) Catalytically active gold on ordered titania supports. Chem Soc Rev 37(9):1860–1870
71. Blyholder G (1964) Molecular orbital view of chemisorbed carbon monoxide. J Phys Chem 68(10):2772–2777
72. Blyholde G, Sheets R (1970) Platinum-carbon stretching frequency for chemisorbed carbon monoxide. J Phys Chem 74(25):4335–4338
73. Hensen EJM, Ligthart DAJM, van Santen RA (2011) Supported rhodium oxide nanoparticles as highly active CO oxidation catalysts. Angew Chem Int Edit 50(23):5306–5310

74. Somorjai GA et al (2008) A reactive oxide overlayer on rhodium nanoparticles during CO oxidation and its size dependence studied by in situ Ambient-Pressure X-ray photoelectron spectroscopy. Angew Chem Int Edit 47(46):8893–8896

75. Rodriguez JA et al (2007) activity of CeOx and TiOx nanoparticles grown on Au(111) in the water-gas shift reaction. Science 318(5857):1757–1760

76. Yao YX et al (2010) growth and characterization of Two-dimensional FeO nanoislands supported on Pt(111). J Phys Chem C 114:17069–17079

77. Fu Q et al (2010) Interface-confined ferrous centers for catalytic oxidation. Science 328 (5982):1141–1144

78. Surnev S et al (2002) Reversible dynamic behavior in catalyst systems: oscillations of structure and morphology. Phys Rev Lett 89(24)

79. Chorkendorff I et al (2007) Identification of active edge sites for electrochemical H_2 evolution from MoS_2 Nanocatalysts. Science 317(5834):100–102

80. Nishihata Y et al (2002) Self-regeneration of a Pd-perovskite catalyst for automotive emissions control. Nature 418(6894):164–167

81. Tanaka H et al (2006) Intelligent catalyst having the self-regenerative function of Pd, Rh and Pt for automotive emissions control. Catal Today 117(1–3):321–328

82. Guilhaume, N. and M. Primet (1997) Three-way catalytic activity and oxygen storage capacity of perovskite $LaMn_{0.976}Rh_{0.024}O_3$. J Catal 165(2):197–204

83. Pan XL et al (2007) Enhanced ethanol production inside carbon-nanotube reactors containing catalytic particles. Nat Mater 6(7):507–511

84. Chen W, Pan XL, Bao XH (2007) Tuning of redox properties of iron and iron oxides via encapsulation within carbon nanotubes. J Am Chem Soc 129(23):7421–7426

85. Li YG et al (2011) MoS_2 nanoparticles grown on graphene: an advanced catalyst for the hydrogen evolution reaction. J Am Chem Soc 133(19):7296–7299

86. Nakamura J et al (2009) Enhanced electrocatalytic activity of Pt subnanoclusters on graphene nanosheet surface. Nano Lett 9(6):2255–2259

87. Rodriguez JA, Goodman DW (1992) The nature of the metal metal bond in bimetallic surfaces. Science 257(5072):897–903

88. Rodriguez JA (1996) Physical and chemical properties of bimetallic surfaces. Surf Sci Rep 24(7–8):225–287

89. Nilsson A et al (2005) The electronic structure effect in heterogeneous catalysis. Catal Lett 100(3–4):111–114

90. Holloway S, Lundqvist BI, Norskov JK (1984) Electronic factors in catalysis. Proceedings of the eighth conference on catalysis, Springer, 1984

91. Hammer B, Norskov JK (1995) Why gold is the noblest of all the metals. Nature 376 (6537):238–240

92. Kitchin JR et al (2004) Role of strain and ligand effects in the modification of the electronic and chemical properties of bimetallic surfaces. Phys Rev Lett 93(15)

93. Norskov JK et al (2009) Trends in CO oxidation rates for metal nanoparticles and close-packed, stepped, and kinked surfaces. J Phys Chem C 113(24):10548–10553

94. Kibler LA et al (2005) Tuning reaction rates by lateral strain in a palladium monolayer. Angew Chem Int Edit 44(14):2080–2084

95. Schlapka A et al (2003) Surface strain versus substrate interaction in heteroepitaxial metal layers: Pt on Ru(0001). Phys Rev Lett 91(1)

96. Alayoglu S, Eichhorn B (2008) Rh–Pt bimetallic catalysts: synthesis, characterization, and catalysis of core-shell, alloy, and monometallic nanoparticles. J Am Chem Soc 130 (51):17479–17486

97. Strasser P et al (2010) Lattice-strain control of the activity in dealloyed core-shell fuel cell catalysts. Nat Chem 2(6):454–460

98. Sasaki K et al (2010) Core-protected platinum monolayer shell high-stability electrocatalysts for fuel-cell cathodes. Angew Chem Int Edit 49(46):8602–8607

99. Zhou WP et al (2009) Improving electrocatalysts for O_2 reduction by fine-tuning the Pt-support interaction: Pt monolayer on the surfaces of a $Pd_3Fe(111)$ single-crystal alloy. J Am Chem Soc 131(35):12755–12762

100. Strasser P (2009) Dealloyed core-shell fuel cell electrocatalysts. Rev Chem Eng 25 (4):255–295

101. Mayrhofer KJJ et al (2009) Adsorbate-induced surface segregation for core-shell nanocatalysts. Angew Chem Int Edit 48(19):3529–3531

102. Norskov JK et al (1998) Design of a surface alloy catalyst for steam reforming. Science 279 (5358):1913–1915

103. Nilekar AU et al (2010) Preferential CO oxidation in hydrogen: reactivity of core-shell nanoparticles. J Am Chem Soc 132(21):7418–7428

104. Su HY, Bao XH, Li WX (2008) Modulating the reactivity of Ni-containing Pt(111)-skin catalysts by density functional theory calculations. J Chem Phys 128(19):194707

105. Chen JG, Menning CA, Zellner MB (2008) Monolayer bimetallic surfaces: experimental and theoretical studies of trends in electronic and chemical properties. Surf Sci Rep 63 (5):201–254

106. Stamenkovic VR et al (2007) Improved oxygen reduction activity on $Pt_3Ni(111)$ via increased surface site availability. Science 315(5811):493–497

107. Chen S et al (2009) Origin of oxygen reduction reaction activity on "Pt_3Co" nanoparticles: atomically resolved chemical compositions and structures. J Phys Chem C 113(3):1109–1125

108. Nilekar AU, Mavrikakis M (2008) Improved oxygen reduction reactivity of platinum monolayers on transition metal surfaces. Surf Sci 602(14):L89–L94

109. Chen S et al (2008) Enhanced activity for oxygen reduction reaction on "Pt_3CO" nanoparticles: direct evidence of percolated and sandwich-segregation structures. J Am Chem Soc 130(42):13818–13819

110. Knudsen J et al (2007) A Cu/Pt near-surface alloy for water-gas shift catalysis. J Am Chem Soc 129(20):6485–6490

111. Zhang J et al (2007) Stabilization of platinum oxygen-reduction electrocatalysts using gold clusters. Science 315(5809):220–222

Chapter 2
Experimental Section

The work is mainly carried out in ultrahigh vacuum (UHV) systems and fixed-bed microreactor. The UHV systems include an Omicron Multi-NanoProbe System, a DUV-PEEM/LEEM System, and a Leybold XPS System. The fixed-bed microreactor for reactivity test of supported nanoparticles was designed and installed in laboratory.

2.1 Model Samples and Precursors of Supported Nanoparticles

Pt(111), φ (Diameter) = 10 mm, thickness = 2 mm
Fe wire, φ = 0.1 mm, Johnson Matthey, 99.998%
Ni wire, φ = 0.1 mm, Alfa Aesar, 99.994%
W wire, φ = 0.15 mm, Johnson Matthey, 99.95%
Highly orientated pyrolyitc graphite (HOPG), size = 10 × 10 × 2 mm^3.

Hexachloroplatinic acid ($H_2PtCl_6 \cdot 6H_2O$) and 3d transition metal nitrate salts ($Fe(NO_3)_3$, $Co(NO_3)_3$, $Ni(NO_3)_2$, $Cu(NO_3)_2$) are analytical grade.

2.2 UHV Systems

2.2.1 Omicron Multi-nanoProbe System

Figure 2.1 shows the photograph of the Omicron Multi-NanoProbe System. The base pressure of this system is below 1.0×10^{-10} mbar during STM and XPS
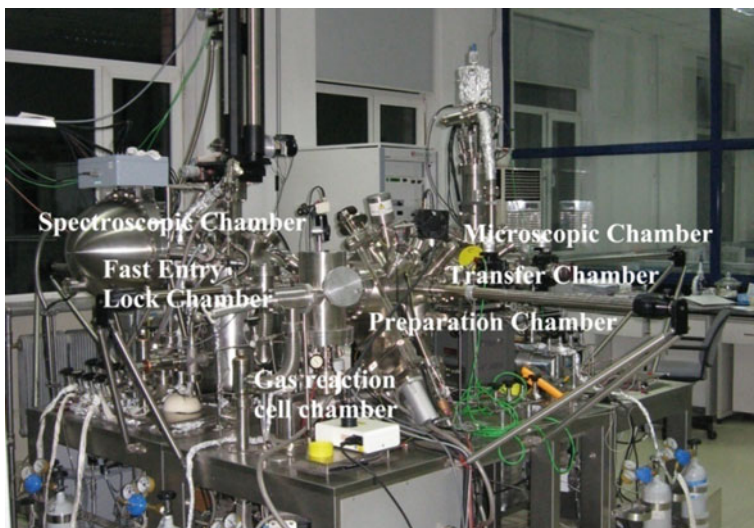
Fig. 2.1 Photograph of Omicron Multi-NanoProbe System

measurement. This Multi-NanoProbe UHV system consists of a preparation chamber, a spectroscopy chamber, a microscopy chamber, and a load lock for sample entering. Preparation chamber includes Ar^+ ion gun and various evaporation sources (Fe, Ni, and Pt) for sample cleaning and preparation. The sample temperature can be controlled between 150 and 1100 K in preparation chamber. Spectroscopy chamber equips with hemispheric energy analyzer (Omicron EA 125 5-channeltron), X-ray source (Omicron DAR400), UV light source (VUV source HIS13), ion gun (ISE100), and high-resolution electron energy loss spectroscopy (HREELS, LK ELS5000). Microscopy chamber contains variable temperature (VT) STM/AFM and PEEM (Focus IS-PEEM).

In Omicron Multi-NanoProbe System, the spectroscopy and microscopy data were recorded by Omicron EIS and Scala Pro5.0 software, respectively. HREELS data was acquired by LK firm software.

2.2.2   *Deep Ultraviolet Photoemission Electron Microscopy System*

As shown in Fig. 2.2, the DUV-PEEM system contains DUV laser source and ELMITEC PEEM/LEEM system. In DUV laser source, the wavelength of laser was converted from 355 nm (1 mw, 80 Hz) to 177.5 nm by a KBBF crystal (from Technical Institute of Physics and Chemistry, CAS). The DUV laser light was focused and introduced into the PEEM/LEEM system via a home-designed vacuum
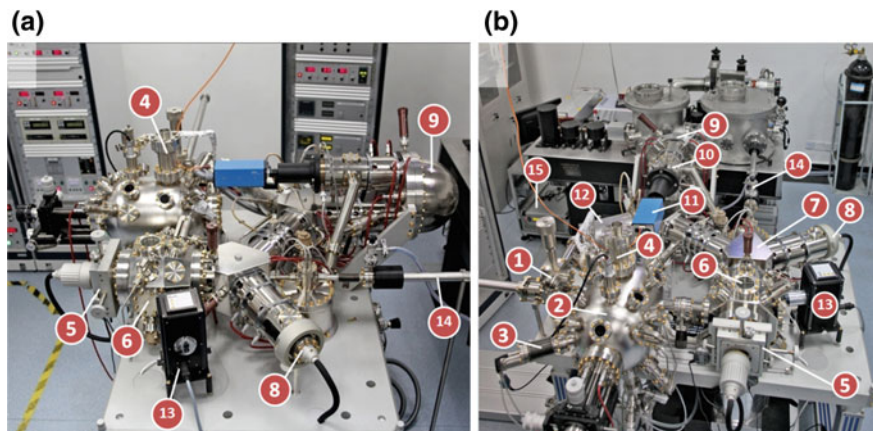
Fig. 2.2 Photographs of PEEM (LEEM-III) system. *1* load lock; *2* preparation chamber; *3* quartz oscillator; *4* mass spectroscopy; *5* Elmitec sample stage; *6* imaging chamber; *7* deflection lens; *8* electron gun; *9* energy analyzer; *10* MCP; *11* CCD; *12* aberration corrector; *13* Hg light source; *14* laser connector; *15* 355 nm laser source

laser connector. The incident angle of DUV laser to the sample surface is 90°. The PEEM/LEEM system consists of a preparation chamber and an imaging system. The imaging system includes a hemispheric energy analyzer, an aberration corrector, a field emission electron gun, and other electron lens. The base pressure of PEEM/LEEM system can be maintained below 1.0×10^{-10} mbar after sufficient baking out.

Utilizing DUV light as the incident source, the resolution of PEEM image can reach 3.9 nm by testing graphene/Ru(0001) sample. In addition, we also use Hg or deuterium lamp as the incident source for PEEM studies. For LEEM and LEED measurements, we employ a LaB_6 filament as electron source. The resolution of LEEM image can reach 1.9 nm using standard Si(100) sample.

In this DUV-PEEM/LEEM system, the PEEM, LEEM and LEED measurements can be recorded at the temperatures between 150 and 2000 K, and at a partial pressure up to 1.0×10^{-5} mbar. The parameters of various electron lens were aligned through ELMITEC LEEM2000 software. Data was acquired by U-view2000 software.

2.2.3   Leybold XPS System

As shown in Fig. 2.3, the Leybold XPS system consists of a high pressure reaction cell and a XPS chamber. Various samples can be pretreated in the high pressure reaction cell at a temperature between room temperature and 900 K. After reaction,
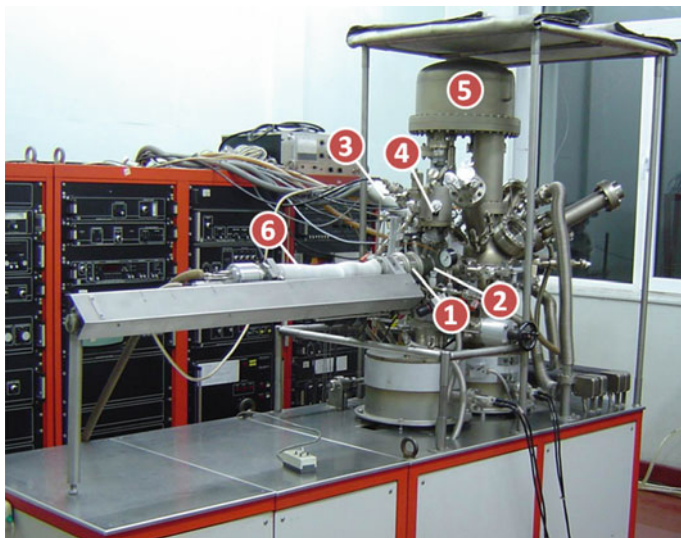
Fig. 2.3 Photograph of Leybold XPS system attached with a high pressure cell. *1* high pressure cell, *2* middle chamber, *3* X-ray source, *4* Ar$^+$ sputter gun, *5* energy analyzer, *6* sample transfer rod

the sample was transferred to XPS chamber without exposing to air. The base pressure of this system can be kept below 5.0×10^{-10} mbar during XPS measurements.

2.3 Experimental Methods of Model Systems

Cleanness of Pt(111) surface: to obtain a clean Pt(111) surface, cycles of Ar$^+$ sputtering ($P_{Ar} = 7.5 \times 10^{-6}$ mbar, 1.5 kV, 10 min), oxidation ($P_{O2} = 1.3 \times 10^{-6}$ mbar, 800 K, 5 min), and high temperature UHV annealing (1060 K, 3 min) were carried out. Finally, no contamination can be detected by XPS, STM, and LEEM.

Fabrication of Fe and Ni source: The Fe(Ni) source was made up of a W filament wrapped with metallic Fe(Ni) wire. Degassing and evaporation of Fe(Ni) source was carried out by passing constant current through W filament. The coverage of Fe (Ni) was controlled by evaporation time.

Preparation of model Fe–Pt(111) and Ni–Pt(111) model catalytic systems: Fe/Pt(111) and Ni/Pt(111) surfaces were prepared by direct evaporating Fe and Ni on Pt(111) surface at room temperature. FeO$_{1-X}$/Pt(111) and NiO$_{1-X}$/Pt(111) surfaces were constructed by depositing Fe and Ni in 1.3×10^{-6} mbar O$_2$ atmosphere. In order to prepare highly dispersed FeO$_{1-X}$ islands on Pt(111) surface, the temperature of Pt(111) surface was decreased to 170 K by using liquid nitrogen. The preparation of NiO$_{1-X}$/Pt(111) surface was carried out at room temperature.

   Gas adsorption on model catalytic systems: Reactant gas adsorption was carried out through leak valve backfilling. The adsorption amount of reactant gas was given in Langmuir (L, $1L = 1 \times 10^{-6}$ Torr $\cdot$ s).

   Data record in model catalytic systems: In Omicron system, XPS spectra were recorded using Mg Kα (1253.6 eV) radiation. UPS signals were acquired in the normal emission direction using He I (21.2 eV) or He II (40.8 eV) as the excitation source. STM images were obtained in constant current mode using a W-tip. In DUV-PEEM/LEEM system, PEEM images were acquired using Hg lamp (4.9 eV) or DUV laser source (6.9 eV). LEEM images were recorded using electron gun radiation. Each PEEM/LEEM image can be acquired in millisecond at a temperature between 150 and 2000 K.

2.4   Experimental Methods of Supported Nanoparticles

Preparation of pure Pt, Pt-3d transition metal (3d-TM: Fe, Co, Ni and Cu) nanoparticles on HOPG: First, a clean HOPG surface was obtained by using adhesive tape to peel off the outer layers. Then the surface was transferred into UHV system and slightly sputtered ($P_{Ar} = 5 \times 10^{-6}$ mbar, 2 kV, 45 s) to produce high density surface defects. Subsequently, ethanol solution of hexachloroplatinic acid (H_2PtCl_6) was dropped onto the sputtered HOPG surface and then reduced at elevated temperature (~ 473 K) in H_2 atmosphere to prepare Pt/HOPG sample. For Pt-3d TM/HOPG sample, a mixed ethanol solution of $H_2PtCl_6 \cdot 6H_2O$ and 3d transition metal nitrate salt was dropped onto the sputtered HOPG surface and then dried in air for further studies.

   Preparation of PtFe/CB and PtNi/CB catalysts: PtFe and PtNi nanoparticles supported on carbon black (CB) were prepared by co-impregnation method using H_2PtCl_6 and nitrate salt as the precursors. After aging and nucleation overnight at 60 °C, fresh PtFe/CB and PtNi/CB catalysts were obtained, in which the loading of Pt and Fe(Ni) was controlled at 4 wt% and 0.3 wt%, respectively (the molar ratio of Pt:Fe(Ni) = 4:1).

   Synchrotron-based X-ray diffraction (XRD) and X-ray absorption spectroscopy (XAS) measurements were conducted to determine the structure and chemical state of PtNi/CB and PtFe/CB in VT-redox treatments and CO oxidation conditions. These experiments were carried out at the BL14B1 and BL14W1 beamlines in Shanghai Synchrotron Radiation Facility.

   The acid leaching treatments combined with the inductively coupled plasma atomic emission spectrometry (ICP-AES) (Thermo Intrepid II) measurements were employed to study the distribution of Ni at various PtNi/CB catalysts.

   The size of PtNi/CB catalysts was characterized by transmission electron microscopy (TEM) (FEI Tecnai G2 Spirit, 120 kV). The size of Pt-3d TM/HOPG model surface was studied by scanning electron microscopy (SEM) (FEI Quanta 200F).

In situ XRD (Rigaku D/MAX-2500/PC, $\lambda = 1.5406$ Å) was employed to investigate the structure of PtNi/CB catalysts in VT-redox cycles.

CO oxidation reactivity of PtFe/CB and PtNi/CB catalysts was measured in a fixed-bed microreactor using multichannel mass spectrometer (Omnistar) or gas chromatographic (Agilent 6890) for tail gas analysis. The CO oxidation gas with excess O_2 consists of 1% CO, 20% O_2, and 79%He. The CO oxidation gas with excess H_2 consists of 1% CO, 0.5% O_2, and 98.5% H_2. The gas hourly space velocity (GHSV) of both was set at 30,000 mL g^{-1} h^{-1}.

Chapter 3
Construction and Reactivity of Pt–Ni Catalysts

We construct and study the catalytic properties of various Ni–Pt(111) model surfaces. We find the sandwich-like structure which consists of surface NiO_{1-X} and subsurface Ni performs best CO oxidation reactivity. The surface NiO_{1-X} provides active sites for O_2 dissociative adsorption. The subsurface Ni lowers the barrier for CO + O elemental reaction. As thus, the synergetic effect of surface NiO_{1-X} and subsurface Ni promotes CO oxidation on Pt. The effect of reduction temperature on the surface structure and reactivity of catalysts has often been overlooked. In our studies, we show the surface structure of Pt–Ni/CB nanoparticles can be simply modulated by reduction temperatures. The XANES investigations combined with ICP measurements indicate that the high reduction temperature can induce more Ni diffuse inward. Upon the reduction at 523 K, the sandwich-like structure with half Ni on the surface and another half Ni inside the nanoparticle can be formed, which shows high CO oxidation reactivity.

3.1 Motivation

Bicomponent catalysts often show better activity, selectivity, and stability than mono-component catalysts [1–14]. The common structures of bimetallic catalysts contain alloy, core–shell, and side-by-side [3, 4, 13, 15–25]. For example, the alloyed Pd–Au catalyst showed high selectivity in the oxidation of alcohol to aldehyde [6]. The core–shell Rh–Pt catalyst performs better reactivity and selectivity of preferential CO oxidation in excess H_2 than alloyed structure and their parent monometallic catalysts [15, 16]. Furthermore, a side-by-side structural Pt–Au catalyst also exhibited high ORR performance [11].

Pt-based bimetallic catalysts have been widely used in catalytic reactions, including ORR [9, 10, 22, 26–32], WGS [20, 33–35], and CO oxidation [14–16, 36, 37]. For example, M. Watanabe and coworkers have suggested a "bifunctional" mechanism for Pt–Fe/SiO$_2$ catalysts in CO oxidation, where Pt atoms acted as the

active sites for CO adsorption and surface Fe provided active sites for O_2 dissociative adsorption, respectively [38, 39]. Surface science studies combined with theoretical calculation and reactivity test revealed that the interface confined coordinatively unsaturated ferrous (CUF) centers were the active sites for O_2 dissociative adsorption. For Pt–Ru, Rh, Pd, Ir bimetallic catalysts, the subsurface component (Ru, Rh, Pd, or Ir) promotes CO oxidation reactivity of Pt surface [15, 16]. In contrast, the isolated Pt and Co (Ni) bimetallic structure of Pt–Co(Ni) catalysts was proposed to be the active structure for preferential CO oxidation in excess H_2. Therefore, the identification of active sites and the understanding of reaction mechanism of Pt-based bimetallic catalysts in catalytic CO oxidation are still in debates, especially for Pt-3d TM bimetallic catalysts [40, 41].

In this chapter, various Ni–Pt(111) model catalytic systems are constructed in UHV chambers. We find the sandwich-like NiO_{1-X}/Pt/Ni/Pt(111) model surface shows best CO oxidation reactivity. Based on the results from model systems, the surface structure and reactivity of supported Pt–Ni/CB catalysts are investigated after reduction treatment at different temperatures. The results of supported Pt–Ni/CB catalysts are well consistent with the findings of model catalytic systems.

3.2   Pt–Ni Model Catalytic Systems

3.2.1   Preparation of Various Ni–Pt(111) Structures

First, various Ni–Pt(111) model surfaces were constructed by molecular beam epitaxy (MBE) methods. As shown in Fig. 3.1a, metallic Ni on Pt(111) surface (Ni/Pt(111)) was prepared by evaporating Ni source in UHV condition at room temperature. STM image shows the step of Pt(111) surface is decorated by metallic Ni, indicating Ni is prone to nucleate at step sites (Fig. 3.1a). At low coverage, Ni islands exhibit one-atomic height (~ 0.2 Å), with the size between 5 and 10 nm on Pt terraces. As the Ni coverage increases to 1.3 ML, both bi-layer and tri-layer structures can be observed in Fig. 3.1b. Therefore, the growth of Ni on Pt(111) surface does not obey a perfect layer-by-layer mode at room temperature. XPS characterizations show the binding energies of Ni2p3/2 peak from 0.16 ML Ni/Pt (111) and 1.3 ML Ni/Pt(111) surfaces both locate at 852.7 eV (Fig. 3.2a, b), indicating the Ni islands and thin films are metallic.

Subsequently, the 1.3 ML Ni/Pt(111) surface was annealed in UHV condition. XPS result shows the ratio of Ni2p/Pt4f decreases as the annealing temperature increases. When the 1.3 ML Ni/Pt(111) surface was annealed at 800 K for 5 min, the intensity of XPS Ni2p peak decreased to 33% (Fig. 3.2c). Similarly, Besenbacher and coworkers have found that the intensity of XPS Cu peak decreased to $\sim 30\%$ after annealing 1 ML Cu/Pt (111) at 800 K. Theoretical calculation indicated about 40% of Cu was presented in the subsurface while the rest was averagely dispersed in 3–11 layers after annealing [20]. After UHV annealing
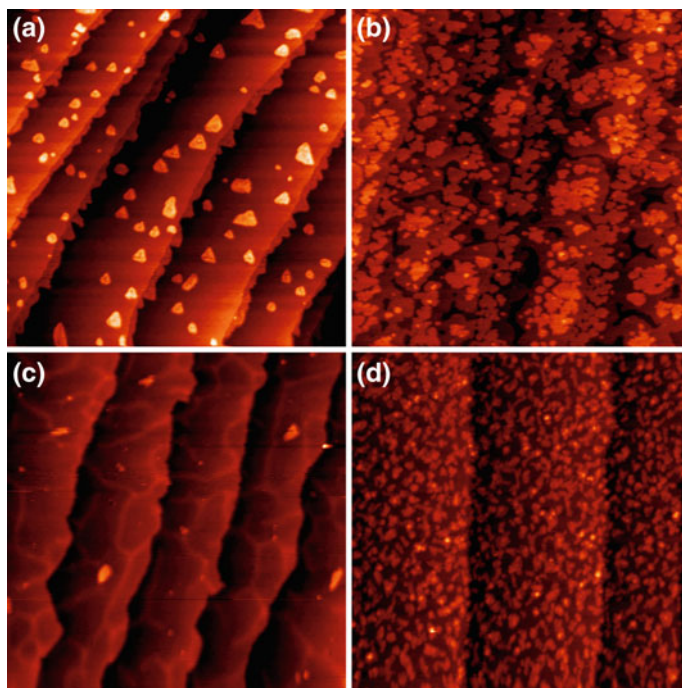
Fig. 3.1 STM images of the surfaces of **a** 0.16 ML Ni/Pt(111), **b** 1.3 ML Ni/Pt(111), **c** Pt/Ni/Pt (111), and **d** 0.16ML NiO$_{1-X}$/Pt(111). Conditions: **a** −0.350 V, 2.50 nA, 200 × 200 nm^2, **b** −0.302 V, 1.700 nA, 200 × 200 nm^2, **c** −0.275 V, 0.957 nA, 200 × 200 nm^2, **a** 2.365 V, 0.025 nA, 100 × 100 nm^2. Reprinted with permission from Ref. [42]. Copyright (2011) American Chemical Society

Fig. 3.2 XPS Ni 2p3/2 spectra of the surfaces of **a** 0.16 ML Ni/Pt(111), **b** 1.3 ML Ni/Pt(111), **c** Pt(111) with 1.3 ML subsurface Ni, Pt/Ni/Pt(111), **d** 0.16 ML NiO$_{1-X}$/Pt(111), and **e** 0.16 ML NiO$_{1-X}$ on Pt/Ni/Pt(111). To compare the line shapes, each spectrum has been multiplied by various numerical factors, which are indicated in the figure. Reprinted with permission from Ref. [42]. Copyright (2011) American Chemical Society
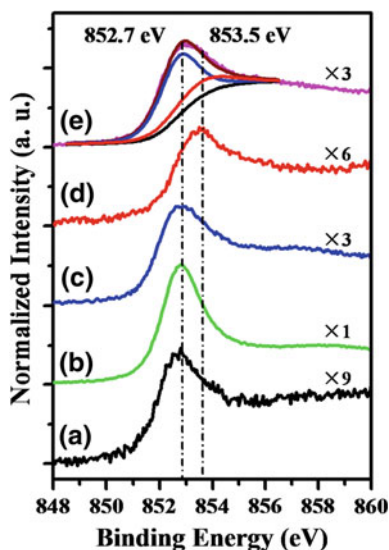
Fig. 3.3 The evolution of ISS intensity ratio, I_{Ni}/I_{Pt} of Pt/Ni/Pt(111) surface as the He$^+$ incident time increases
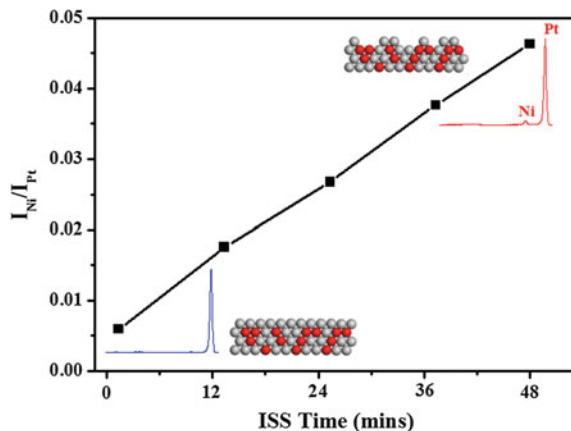
treatment of 1.3 ML Ni/Pt(111), we find that Ni films disappear from Pt(111) surface. Simultaneously, the white line structures are observed on Pt(111) surface (Fig. 3.1c). In previous studies, the similar surface features were also found on Pt-skin surface with subsurface Fe, Co, Ni, or Cu [20, 43, 44].

As is known to us, ISS characterizations have often been employed to study the surface composition of model systems. Though ISS has been considered as a slightly damaging detection technique, the ion incidence with extended time will still sputter away the surface atoms. As shown in Fig. 3.3, the ISS I_{Ni}/I_{Pt} ratio of annealed Ni/Pt(111) sample significantly increases as the detection time increases, which reveals the existence of Ni in subsurface region. Based on STM, XPS, and ISS results, we find a Pt-skin surface with subsurface Ni(Pt/Ni/Pt(111)) can be obtained by annealing Ni/Pt(111) surface in UHV condition at 800 K.

Similar to the preparation of FeO_{1-X}/Pt(111) model surface, NiO_{1-X} on Pt(111) surface was prepared by depositing Ni in 1.3×10^{-6} mbar O_2 at room temperature. Figure 3.1d shows the highly dispersed NiO_{1-X} on Pt(111) surface. The binding energy of Ni2p3/2 peak from NiO_{1-X}/Pt(111) surface locates at 853.5 eV, (Fig. 3.2d) which is close to that of Ni^{2+} in early works [45, 46]. In addition to NiO_{1-X}/Pt(111) surface, we also prepare NiO on HOPG surface (NiO/HOPG) as a reference sample. The NiO/HOPG sample was obtained by evaporating Ni in 1.3×10^{-6} mbar O_2 at room temperature, and then annealed in 1.3×10^{-6} mbar O_2 at 800 K for 10 min. NiO on HOPG surface presents three-dimensional (3D) structure with the height of 2–4 nm (Fig. 3.4).

The binding energy of Ni2p3/2 peak from NiO/HOPG sample is found to locate at 854.1 eV (Fig. 3.5), which is well consistent with that of Ni^{2+} [45, 46]. So the O/Ni ratio of NiO/HOPG sample is defined to be 1. To estimate the O/Ni ratio of NiO_{1-X}/Pt(111) model surface, we first need to eliminate the influence of O on bare Pt(111) area by exposing NiO/Pt(111) surface in CO at room temperature, because we are unable to distinguish the binding energies of XPS O1s peaks between O/Pt(111) area and NiO_{1-X}. Fortunately, the binding energy of O1s peak of NiO_{1-X}

Fig. 3.4 STM image of the NiO/HOPG(0001) sample. Imaging conditions: 5.000 V, 0.020 nA, 200 nm × 200 nm. The NiO formed on the HOPG surface exhibits 3D structure. Reprinted with permission from Ref. [42]. Copyright (2011) American Chemical Society
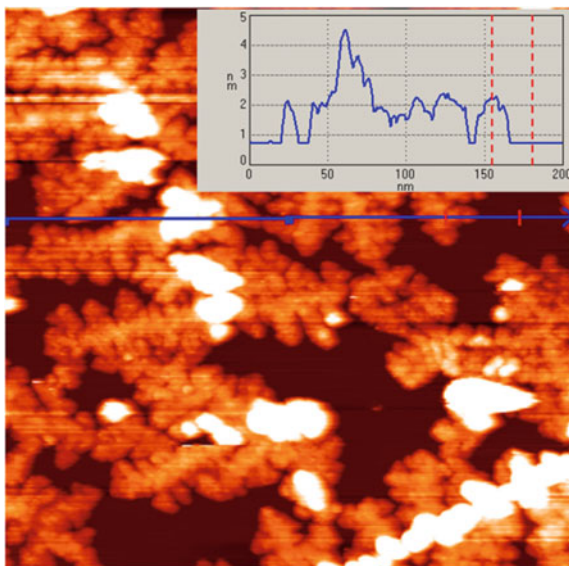
Fig. 3.5 **a** XPS O1s peak of NiO_{1-X}/Pt(111), **b** XPS Ni2p3/2 peak of NiO_{1-X}/Pt (111), **c** XPS O1s peak of NiO/HOPG, **d** XPS Ni2p3/2 peak of NiO/HOPG. In (**a**), *green* and *gray dash lines* represent O1s peaks from NiO_{1-X} and CO, respectively. Reprinted with permission from Ref. [42]. Copyright (2011) American Chemical Society
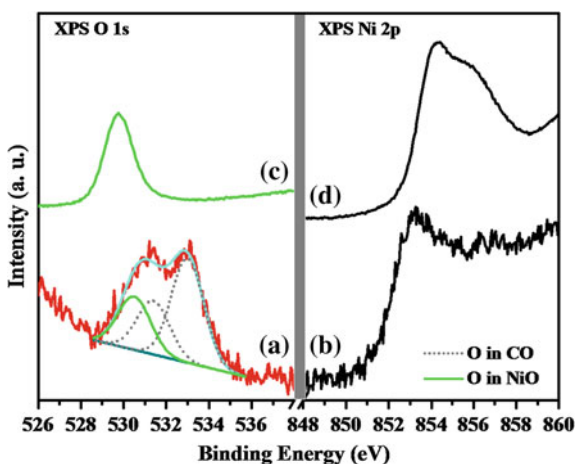
can be clearly distinguished from those of CO on Pt(111). As shown in Fig. 3.5, the binding energy of O1s peak of NiO_{1-X} locates at 530 eV, while those from bridging and linear CO locate at 531.4 and 533.0 eV, respectively [47]. Through deconvolving the XPS O1s peak of NiO_{1-X}, we find the O/Ni ratio of NiO_{1-X} is 0.65 ($NiO_{0.65}$/Pt(111)).

As shown in Fig. 3.1d, the highly dispersed NiO_{1-X} islands present monolayer height on Pt(111) surface. In previous studies, the similar monolayer NiO structures have been observed on Pt(111) [48] and Pd(100) [49] as well. Different from monolayer NiO_{1-X} islands on Pt(111), NiO presents 3D structure on HOPG surface

(Fig. 3.4). The reason can be attributed to the weakly interfacial interaction between NiO and defect-free HOPG surface. For NiO_{1-X}/Pt (111) surface, the strongly interfacial interaction between NiO_{1-X} and Pt(111) plays a critical role in stabilizing monolayer NiO_{1-X} islands.

3.2.2   Interfacial Catalysis on NiO_{1-X}/Pt(111)

In UPS HeII spectra, the binding energies of $5\sigma + 1\pi$ and 4σ orbitals of CO molecules on Pt(111) locate at 9.4 and 11.8 eV, respectively [43, 50, 51]. In order to investigate the CO oxidation reactivity of various Ni–Pt(111) model catalytic surfaces, in situ UPS HeII was employed to detect the intensity of CO on Pt(111) surface as a function of time in 4.0×10^{-8} mbar O_2 at room temperature.

For a comparison, the CO/Pt(111) surface was first exposed in O_2 at room temperature. We find the decrease of CO is negligibly small in 30 min (Fig. 3.6a), indicating Pt(111) surface is fully covered by CO molecules at room temperature.
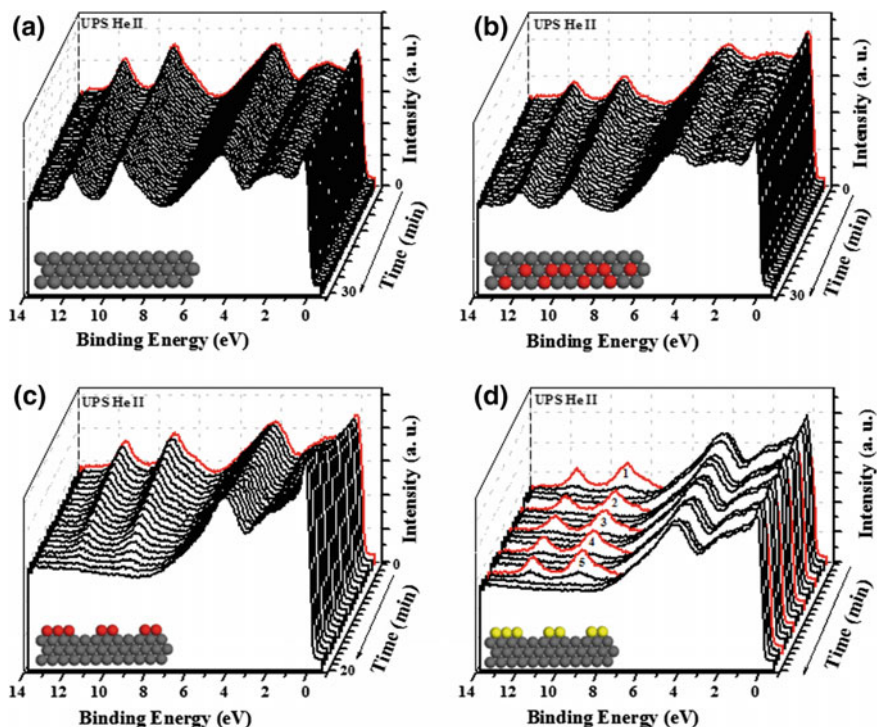
Fig. 3.6 In situ He II UPS spectra recorded from the CO saturated surfaces exposed to 4.0×10^{-8} mbar O_2 at room temperature. **a** The bare Pt(111) surface. **b** The Pt(111) with 1.3 ML subsurface Ni, Pt/Ni/Pt(111). **c** The 0.16 ML Ni/Pt(111) surface. **d** The 0.16 ML NiO_{1-X}/Pt(111) surface. The *red line* is the *onset* of the reaction. *Inset gray* Pt; *red* Ni; *yellow* NiO_{1-X}. Reprinted with permission from Ref. [42]. Copyright (2011) American Chemical Society

Figure 3.6b displays the reactivity of Pt/Ni/Pt(111) model surface, which is similar to that of pure Pt(111) surface, i.e., the UPS intensity of CO does not change in O_2 atmosphere in 30 min. Previous works have shown subsurface transitional metal weakened the interaction of CO, –OH, and O_2 adsorbates with Pt-skin surface, and thus promoted the ORR performance of Pt catalysts. For example, the adsorption energy of CO and O_2 on a pure Pt(111) surface have been determined to be −1.82 eV and −0.65 eV, while those on a Pt-skin surface with subsurface Ru decreased to −1.25 eV and −0.26 eV, respectively [15]. But we find the adsorption energy of CO is still much higher than the adsorption energy of O_2 on Pt-skin surface. Furthermore, Mavrikakis and coworkers have revealed the dissociation barrier of O_2 on Pt-skin surface (0.93 eV) with subsurface Co was higher than that on Pt(111) surface (0.77 eV) [52]. These results explain why the Pt/Ni/Pt(111) performs a similar reactivity to Pt(111) surface at room temperature.

We also study the stability of Pt/Ni/Pt(111) model surfaces in catalytic CO oxidation. As shown in Fig. 3.7b, both the binding energy and intensity of Ni2p3/2 peaks keep unchanged before and after CO oxidation in 4.0×10^{-8} mbar O_2 at 391 K. Chen and coworkers have determined the activation barrier of Ni surface segregation to be 17 ± 1 kcal/mol, [53] indicating Pt/Ni/Pt(111) was stable under low-temperature CO oxidation.

In Fig. 3.6c, we find the CO on Ni/Pt(111) can be eliminated gradually in O_2 at room temperature. XPS studies show the binding energy of Ni2p3/2 shifts from
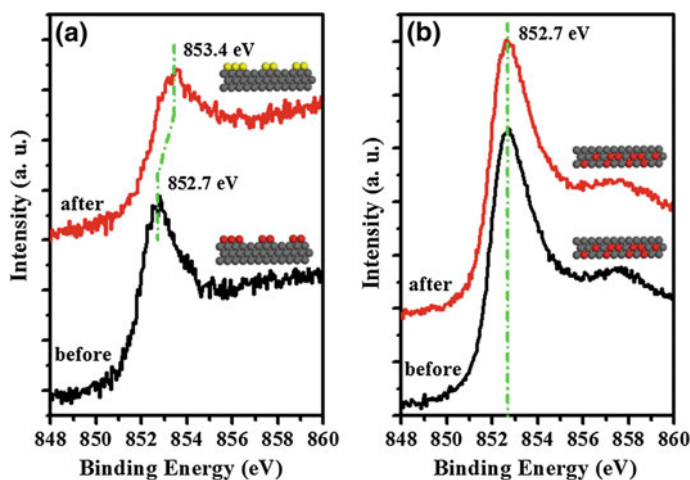
**Fig. 3.7** (a) XPS Ni2p3/2 peaks of the 0.16 ML Ni/Pt(111) before and after the CO oxidation reaction. (b) XPS Ni2p3/2 peaks of the Pt/Ni/Pt(111) before and after the CO oxidation at 391 K (10 L CO was pre-adsorbed, then the oxidation was carried out in 4.0×10^{-8} mbar O_2). Reprinted with permission from Ref. [42]. Copyright (2011) American Chemical Society

852.7 to 853.4 eV after reaction (Fig. 3.7a), indicating metallic Ni is oxidized to NiO_{1-X}.

The NiO_{1-X}/Pt(111) exhibits a better CO oxidation reactivity at room temperature as shown in Fig. 3.6d. In 4.0×10^{-8} mbar O_2 atmosphere, pre-adsorbed CO can be removed in 2 min. Through dosing CO again, the catalytic CO oxidation reactions are repeated for 5 times. We find the reactivity of NiO_{1-X}/Pt(111) model surface keeps unchanged after cycles of CO oxidation reactions. Previous works have reported the coordinative unsaturated sites at the edge of oxide islands were active sites for dissociative adsorption of reactants [54–58]. Therefore, we suggest the high reactivity of NiO_{1-X}/Pt(111) model surface can be attributed to the coordinatively unsaturated Ni atoms at the edges of NiO_{1-X} islands.

DFT calculations have revealed the activation barrier of $CO + O \rightarrow CO_2$ elementary reaction decreased by 0.49 eV on a Pt-skin surface with subsurface Ni compared to Pt(111) surface [59]. Furthermore, Nilekar and coworkers have constructed a Pt-skin layer on Ru(0001), Rh(111), Pd(111), and Ir(111) slabs, and studied the activation barrier of $CO + O \rightarrow CO_2$ elementary reaction on these various surfaces. They found the activation barrier of $CO + O \rightarrow CO_2$ elementary reaction was lower on Pt-skin surfaces than that on Pt(111) surface. For example, activation barrier of $CO + O \rightarrow CO_2$ elementary reaction was 0.79 eV on Pt(111) surface, while that decreased to 0.41 eV on a Pt-skin surface on Ru(0001) substrate [15, 16]. Both theoretical calculations and experimental results have demonstrated subsurface transition metals could weaken the interaction of molecules with Pt surface, lower the activation barrier, and thus promote $CO + O \rightarrow CO_2$ elementary reaction. However, the catalytic CO oxidation reaction is still prohibited on Pt/Ni/Pt (111) surface at room temperature due to the lack of empty sites for O_2 dissociative
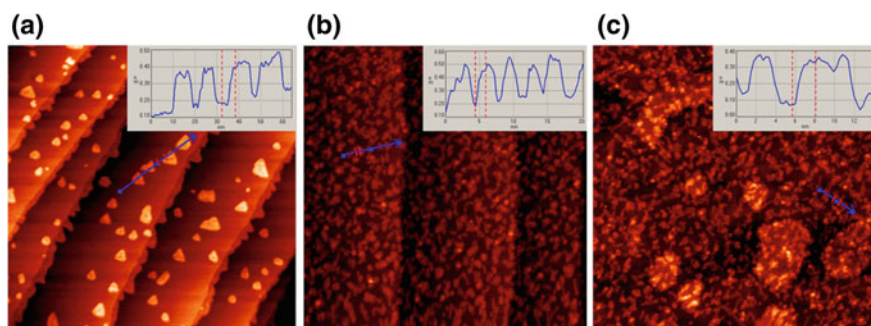
Fig. 3.8 STM images and line profiles of **a** metallic Ni islands on Pt(111) surface (Ni/Pt(111)), **b** NiO_{1-X} on Pt(111) surface (NiO_{1-X}/Pt(111)), and **c** NiO_{1-X} on the Pt-skin surface (NiO_{1-X}/Pt/Ni/Pt(111)). **a** −0.350 V, 2.50 nA, 200×200 nm^2; **b** 2.365 V, 0.025 nA, 100×100 nm^2; **c** 1.500 V, 0.025 nA, 100×100 nm^2. Reprinted with permission from Ref. [42]. Copyright (2011) American Chemical Society

adsorption. In Fig. 3.6d, we show the NiO_{1-X} nanoislands provide active sites for O_2 dissociative adsorption. So the combination of surface NiO_{1-X} nanoislands and subsurface Ni may create a promising model catalytic system for CO oxidation.

3.2.3 Synergetic Effect of Surface and Subsurface Ni

In order to investigate the synergetic effect of surface NiO_{1-X} nanoislands and subsurface Ni, we construct a new sandwich-like NiO_{1-X}/Pt/Ni/Pt(111) model surface. It is prepared by depositing 0.16 ML Ni onto Pt/Ni/Pt(111) in 1.3×10^{-6} mbar O_2 at room temperature. Through deconvolution of the XPS Ni2p3/2 peak from NiO_{1-X}/Pt/Ni/Pt(111) model surface, we find two peaks locate at 852.7 and 853.5 eV (Fig. 3.2e), which derive from subsurface Ni and surface NiO_{1-X}, respectively. In STM images, NiO_{1-X} islands on Pt-skin surface show similar dispersion as that on Pt(111) surface. More importantly, the height of NiO_{1-X} islands is also one monolayer on Pt-skin surface, i.e., one layer Ni binds with (1×1) O on top (Fig. 3.8).

The sandwich-like NiO_{1-X}/Pt/Ni/Pt(111) model surface shows high CO oxidation reactivity, which is similar to that of NiO_{1-X}/Pt(111) surface. We find that the pre-adsorbed CO can be eliminated from NiO_{1-X}/Pt/Ni/Pt(111) surface in 2 min at room temperature. To distinguish the CO oxidation reactivity between NiO_{1-X}/Pt/Ni/Pt(111) and NiO_{1-X}/Pt(111) surfaces, we carry out the experiments at 220 K. The process of low-temperature CO oxidation can be described as follows. First, NiO_{1-X}/Pt/Ni/Pt(111) and NiO_{1-X}/Pt(111) model surfaces are saturated by CO at room temperature. Then the surfaces are cooled down in UHV condition by using liquid nitrogen. At 220 K, in situ UPS spectra of CO molecules on surfaces are recorded in 4.0×10^{-8} mbar O_2. Figure 3.9a and b displays the UPS spectra of CO as a function of time on NiO_{1-X}/Pt/Ni/Pt(111) and NiO_{1-X}/Pt(111) model surfaces. Compared to the low reactivity of NiO_{1-X}/Pt(111) surface at 220 K, we find that 70% of CO can be eliminated from NiO_{1-X}/Pt/Ni/Pt(111) surface in 14 min. In situ characterizations reveal the sandwich-like NiO_{1-X}/Pt/Ni/Pt(111) model catalytic system shows the best CO oxidation reactivity. Since NiO_{1-X} islands provide active sites for O_2 dissociative adsorption, we suggest the initial stage of $CO + O \rightarrow CO_2$ reaction should happen around NiO_{1-X}. This initial process is not strongly affected by the diffusion rate of reactants. In order to exclude the influence of diffusion of reactants on apparent reaction barrier, especially for low temperature test, we estimate only initial reaction rate of $CO + O$ to compare the reactivity between NiO_{1-X}/Pt/Ni/Pt(111) and NiO_{1-X}/Pt(111) model surfaces. Through the Arrhenius plot of CO intensity, the reaction barrier of $CO + O \rightarrow CO_2$ on NiO_{1-X}/Pt/Ni/Pt (111) can be determined to be 6.8 kJ/mol lower than that on NiO_{1-X}/Pt(111).
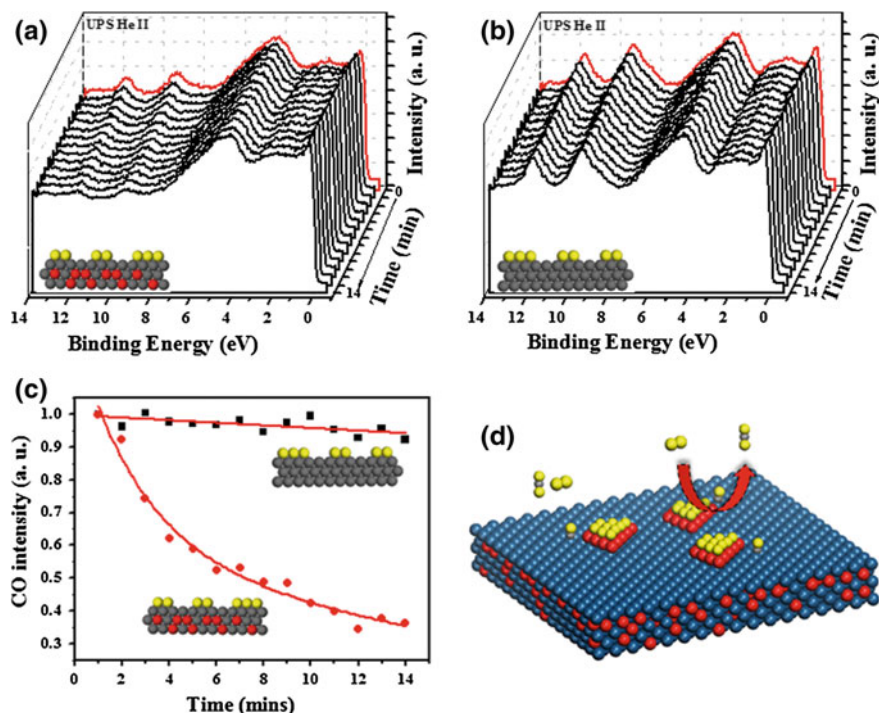
Fig. 3.9 In situ He II UPS spectra recorded from the CO pre-saturated surfaces exposed to 4.0×10^{-8} mbar O_2 at 220 K. **a** The 0.16 ML NiO_{1-X}/Pt/Ni/Pt(111) surface and **b** the 0.16 ML NiO_{1-X}/Pt(111) surface. **c** Plots of the CO 4σ peak area as a function of O_2 exposure time on the two surfaces. **d** Synergetic effect of surface NiO_{1-X} and subsurface Ni at Ni–Pt(111) model catalyst for CO oxidation. *Blue* Pt, *red* Ni, *yellow* O, *gray* C. Reprinted with permission from Ref. [42]. Copyright (2011) American Chemical Society

3.3 Supported Pt–Ni Nanoparticle Catalysts

Pt–Ni bicomponent catalysts supported on carbon black (Pt–Ni/CB) were prepared by traditional co-impregnation method, where the loading amount of Pt and Ni was controlled at 4 wt% and 0.3 wt%, respectively (mole ratio = 4:1). Fresh Pt–Ni/CB catalysts were obtained via reduction in H_2 at elevated temperatures. Since Pt precursor can be easier reduced to form metallic nanoparticles than 3d transition metal oxide, we propose the formation of Ni overlayers on the surface of Pt nanoparticles under low-temperature reduction (~ 400 K). As the reduction temperature increases, more 3d transition metals diffuse into the subsurface and even bulk region [12, 20, 44, 60–62]. Therefore, the surface structure of Pt–Ni/CB bicomponent catalysts may be simply modulated by reduction treatment at various temperatures.

First, the surface composition of Pt–Ni/CB catalysts reduced at various temperatures was investigated by acid leaching in HCl solution with the concentration

Fig. 3.10 Concentrations of Pt and Ni ions in the acid solutions from the fresh Pt–Ni/CB catalyst and the catalysts reduced at 423, 523, and 623 K. The concentrations were measured by ICP-AES, and the values from the fresh catalysts were normalized to 1. Reprinted with permission from Ref. [42]. Copyright (2011) American Chemical Society
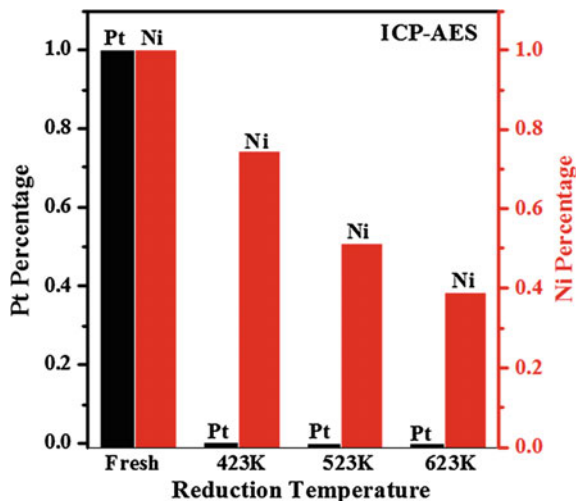
of 2.5×10^{-3} mol/L. The concentration of leached Pt and Ni ions in acid solution was determined by ICP-AES. As a reference, the concentration of Pt and Ni from freshly dried Pt–Ni/CB was also included and normalized to 1. As shown in Fig. 3.10, the concentration of Pt is negligible from all reduced samples indicating Pt precursor can be reduced to metallic state completely. In contrast, Ni from reduced Pt–Ni/CB catalysts presents a high concentration in acid solution. After the reduction at 423 K, about 75% of Ni can be dissolved in acid solution. As the reduction temperature increases, less Ni can be leached away from Pt–Ni/CB catalysts. Only a third of Ni was dissolved in acid solution after the reduction treatment at 623 K. Based on the previous studies, acid leaching Pt-3d transition metal bicomponent systems dissolve only 3d-TMs on surface in acid solution, whereas those in bulk are unchanged due to the protection of Pt outlayer [63–66]. Therefore, the results of acid leaching experiments illustrated that the reduction treatment induces the inward diffusion of Ni into subsurface and bulk region at elevated temperature. At a medium reduction temperature, i.e., 523 K, half of Ni remains on Pt surface and others diffuse into the Pt subsurface and bulk.

As an in situ characterization technique, the X-ray absorption fine structure (XAFS) study based on synchrotron light has been widely employed in heterogeneous catalysis [67–72]. Here, XAFS Ni–K edge was acquired to determine the chemical state of Ni under reduction treatment (20% H_2 with He balance) and CO oxidation condition (1% CO, 20% O_2 and He balance). As shown in Fig. 3.11a, Pt–Ni/CB samples reduced at 423, 523, and 623 K present the similar white peak features of Ni–K edge of metallic Ni foil. In addition, the position of Ni–K adsorption edge is 8333.0 eV which is same as metallic Ni foil (Fig. 3.11). Fourier transforms of Ni–K edge show the Ni–O interaction disappears after reduction at 423 K, indicating Ni can be reduced completely (Fig. 3.12).

We also study the chemical states of Ni species over Pt–Ni/HOPG sample after reaction treatments. Since the loading amount of Ni over Pt–Ni/CB is too low
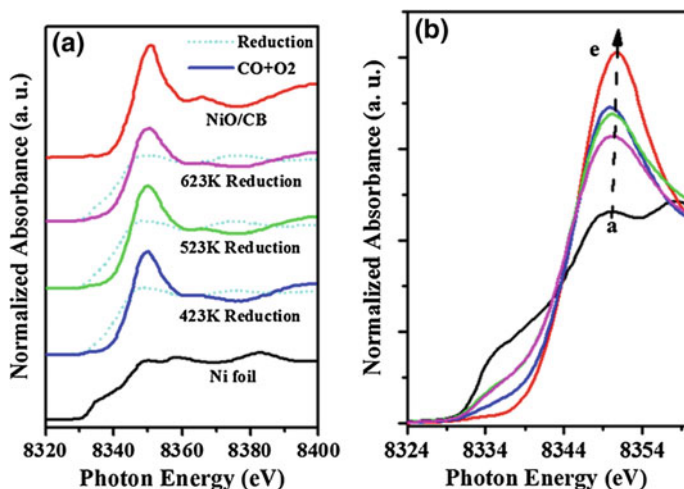
Fig. 3.11 a X-ray absorption near edge structure (XANES) Ni–K-edge spectra acquired from Ni foil, Pt–Ni/CB after reductions at different temperatures (*dashed line*) and exposed to air at room temperature, (*solid lines*) and NiO/CB sample. **b** Zoomed white line peaks in (**a**). *a* Ni foil, *b* Pt–Ni/CB catalysts reduced at 623 K for 2 h and then exposed to air at room temperature, *c* Pt–Ni/CB catalysts reduced at 523 K for 2 h and then exposed to air at room temperature, *d* Pt–Ni/CB catalysts reduced at 423 K for 2 h and then exposed to air at room temperature, and *e* NiO/CB catalysts. Reprinted with permission from Ref. [42]. Copyright (2011) American Chemical Society

Fig. 3.12 Fourier transforms of Ni–K edge of metallic Ni foil, Pt–Ni/CB reduced at 423 K for 2 h and NiO/CB. Reprinted with permission from Ref. [42]. Copyright (2011) American Chemical Society
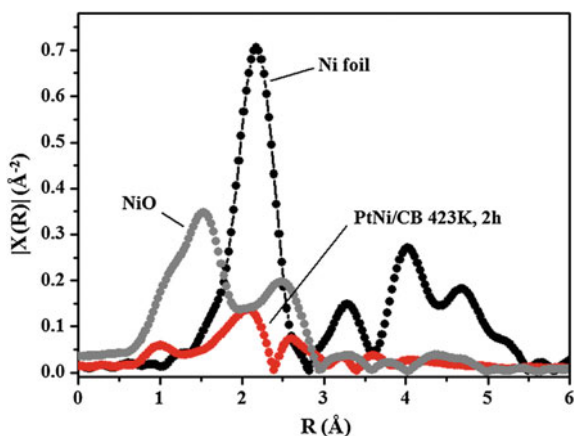
(0.3% wt) to obtain decent XPS signal, we prepare high-density Pt–Ni nanoparticles on sputtered HOPG surface. The preparation details and characterizations of Pt–Ni/HOPG samples can be found in Chap. 4. As shown in Fig. 3.13, the binding energy of XPS Ni2p3/2 peak is 852.7 eV after reductions at 423, 523, and 623 K. Both XAFS Ni–K edge and XPS studies illustrate Pt makes the reduction of Ni easier.
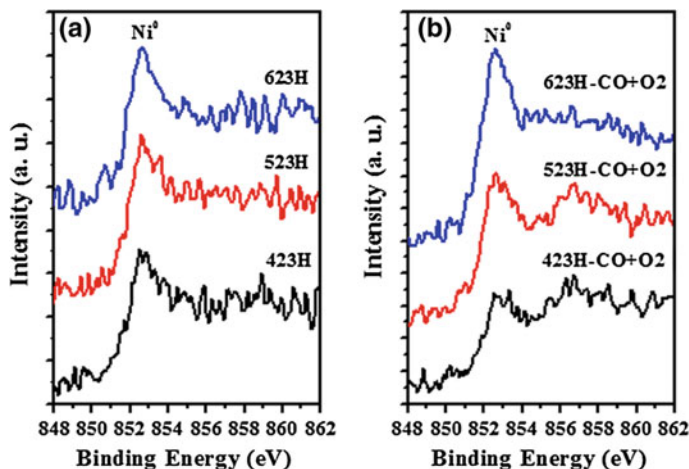
Fig. 3.13 The binding energy of Ni2p3/2 XPS peak from **a** Pt–Ni/HOPG samples reduced at different temperatures for 2 h and **b** Pt–Ni/HOPG samples reduced at different temperatures for 2 h and then exposed to reaction condition (1%CO, 20%O_2, 79%He) at 343 K for 1 h

The findings of XANES and XPS characterizations are well consistent with acid leaching results, which demonstrate the surface configuration of Pt–Ni bicomponent nanoparticles can be modulated through reduction treatments at different temperatures. After low-temperature reduction (423 K), most of Ni locates on the surface of Pt–Ni nanoparticles. High temperature reduction (623 K) induces most of Ni to diffuse into subsurface and even bulk region. While at a medium reduction temperature (523 K), 50% of Ni is still on the surface, whereas other Ni is inside. As thus, a sandwich-like structure of Pt–Ni bicomponent nanoparticle with both surface and subsurface Ni species can be prepared through reduction at a medium temperature. We note that XANES and XPS investigations show the subsurface Ni is stable in air and reaction condition.

At last, we study the reactivity of Pt–Ni/CB catalysts after reduction at different temperatures. The CO oxidation reactivity (1% CO, 20% O_2, He balance) depended on reduction temperature is shown in Fig. 3.14a. We find the 523 K-reduced Pt–Ni/CB catalyst presents the best reactivity. The CO conversion of 523 K-reduced catalyst reaches 70% at room temperature and 100% at 320 K shown in Fig. 3.14a. In contrast, the reactivity of 423 K-reduced and 623 K-reduced Pt–Ni/CB catalysts is lower. Figure 3.14b further shows the CO oxidation reactivity over various catalysts at room temperature. A "Goldilocks" relationship was found between the CO conversion and reduction temperatures over Pt–Ni/CB catalysts, i.e., the medium-temperature-reduced catalysts show the highest reactivity.

Figure 3.14a also shows the CO oxidation reactivity of Pt/CB catalysts reduced at 473 K. We find the CO conversion over Pt/CB reaches a maximum value (~80%) at about 423 K. For comparison, the influence of reduction temperature on the reactivity of Pt/CB catalyst is studied as well. As shown in Fig. 3.15, the Pt/CB
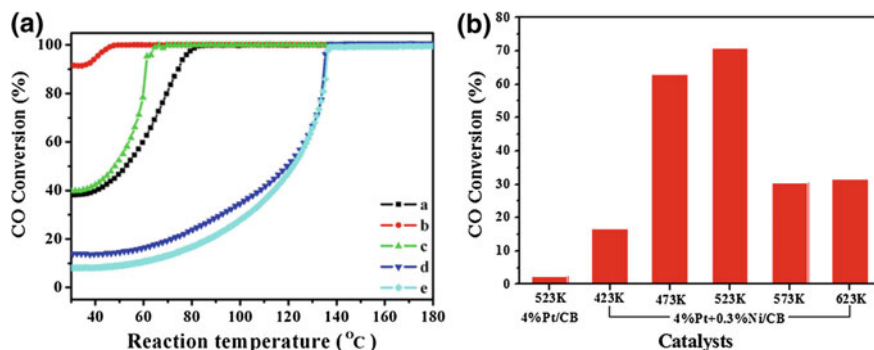
Fig. 3.14 a Temperature-dependent CO conversion in the CO oxidation over the Pt–Ni/CB catalysts reduced at *a* 423 K, *b* 523 K, and *c* 623 K, respectively. For comparison, the results of *d* the Pt/CB catalyst and *e* the leached Pt–Ni/CB catalyst are also included. **b** CO conversion at room temperature over Pt–Ni/CB catalysts reduced at various temperatures, Pt/CB reduced at 523 K is also included. Reprinted with permission from Ref. [42]. Copyright (2011) American Chemical Society
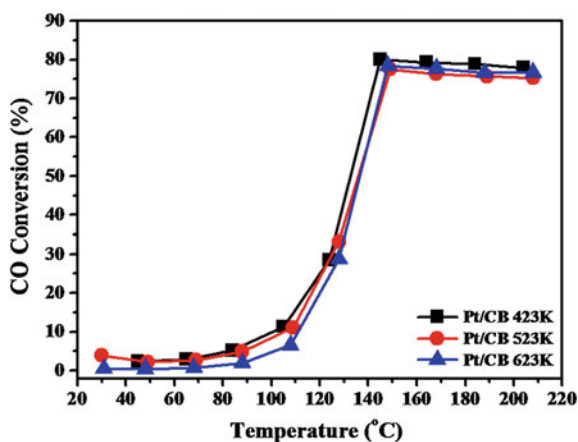
Fig. 3.15 Temperature-dependent CO conversion in the CO oxidation over the Pt/CB catalysts reduced at 423, 523, and 623 K, respectively

catalysts reduced at different temperatures present similar reactivity, indicating the influence of reduction temperature is negligible on the performance of Pt/CB catalysts.

At last, the size distribution of Pt–Ni/CB catalysts was investigated by TEM after reduction at different temperatures. We find the Pt–Ni/CB catalysts reduced at 423 and 623 K show the similar size distributions (Fig. 3.16). Therefore, the size effect on the performance of Pt–Ni/CB catalysts can be excluded. The chemical state of active components is another important factor which often influences the performance of Pt–Ni/CB catalysts significantly. In situ XANES and XPS studies
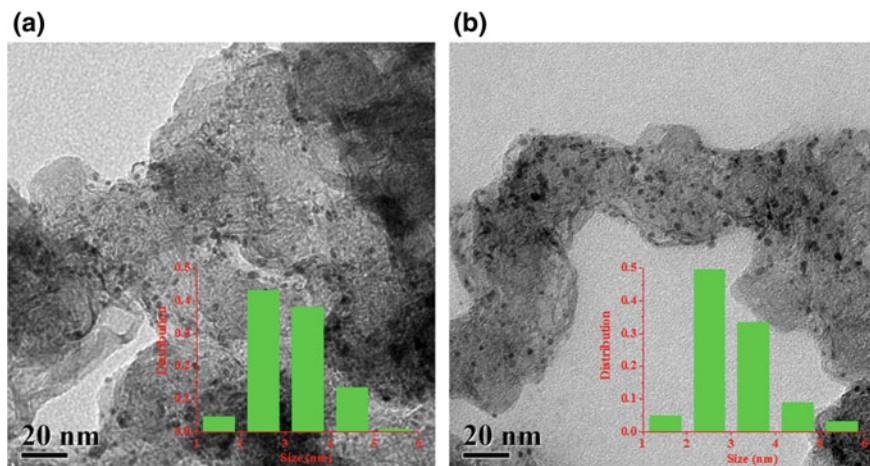
Fig. 3.16 TEM images of the Pt–Ni/CB catalysts reduced at **a** 423 K and **b** 623 K. Reprinted with permission from Ref. [42]. Copyright (2011) American Chemical Society

show Pt and Ni can be reduced to metallic state completely, even after the reduction at 423 K. So we exclude the effect of chemical state of Pt and Ni on the performance of Pt–Ni/CB catalysts as well. Based on the above discussions, we infer the observed "Goldilocks" catalytic performance depended on reduction temperature should be attributed to the different surface configurations of Pt–Ni/CB catalysts.

3.4   Resonable Design of Pt–Ni Bicomponent Catalysts

Based on the results from model catalytic systems, we find that the CO oxidation reactivity of Ni–Pt(111) surfaces increases in the sequence of *Pt(111) < Pt/Ni/Pt(111) < Ni/Pt(111) < NiO$_{1-x}$/Pt(111) < NiO$_{1-x}$/Pt/Ni/Pt(111)*. Two important factors for CO oxidation can be determined based on the results of the Ni–Pt(111) model systems. First, the highly dispersed NiO$_{1-x}$ nanoislands confined on Pt surface play a critical role in dissociative adsorption of O$_2$ at the edge sites, which helps to alleviate CO poisoning issue on Pt. Second, subsurface Ni promotes the CO oxidation on Pt surface by lowering the reaction barrier of elementary step of CO + O → CO$_2$. Therefore, the sandwich-like *NiO$_{1-x}$/Pt/Ni/Pt(111)* model structure performs the highest CO oxidation reactivity.

For supported Pt–Ni nanoparticles, acid leaching ICP, XAFS and XPS experiments clearly show the distribution of the surface and subsurface Ni species can be simply controlled by reduction treatment at different temperatures. We show the surface Ni gets oxidized while the subsurface Ni remains virgin when exposing to oxidative atmospheres (4 × 10^{-8} mbar O$_2$, air and CO oxidation gases with excess O$_2$). Therefore, we infer most of Ni species are still on the surface of the Pt

Fig. 3.17 Synergetic effect of surface Ni oxide and subsurface Ni species at Pt–Ni catalysts for catalytic CO oxidation. Surface Ni oxide structure activates dissociation of O_2 and subsurface Ni atoms promote CO reaction with O. O: *yellow*; Ni: *brown*; Pt: *cyan*; C: *light blue*. Reprinted with permission from Ref. [42]. Copyright (2011) American Chemical Society

O
C
Pt
Ni
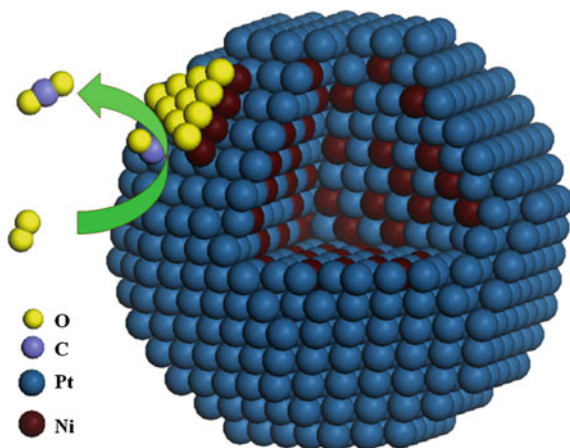
nanoparticles after reduction at 423 K, which resembles the *NiO_{1-X}/Pt(111)* model surface. High temperature reduction, e.g., 623 K, produces the Pt-rich surface, similar to *Pt/Ni/Pt(111)* model system. At an intermediate temperature of 523 K, around half of Ni is outside and the left is inside Pt nanoparticles. Under the reaction condition, this catalyst presents the characteristic structure as the sandwich-like *NiO_{1-X}/Pt/Ni/Pt(111)* surface. The highest CO oxidation reactivity of this sandwich-like *Pt–Ni/CB* catalyst again suggests the important role of both surface NiO_{1-X} and subsurface Ni at the practical catalysts in the CO oxidation (Fig. 3.17).

To further confirm the synergetic effect of the surface and subsurface Ni species on the performance of Pt–Ni nanoparticles, CO oxidation was performed on an acid-leached catalyst. The fresh *Pt–Ni/CB* sample was reduced at 523 K to form a sandwich-like structure. Then, it was leached in the acid solution to remove the surface Ni species. After activation again in H_2 at 423 K, temperature-dependent reactivity of the leached catalyst was shown in Fig. 3.14a–d. The reaction data indicates that the reactivity of the leached sample is quite similar to that of pure Pt/CB catalyst (Fig. 3.14a–e). Although ICP data shows that the leaching treatment only washes away half of Ni from the Pt–Ni NPs, removal of surface Ni species lowers the performance significantly.

3.5 Summary

The structural complexity of supported nanoparticles has made the molecular-level studies of their surface structure and reaction mechanism very challenging. In this chapter, we show the results from the Ni–Pt(111) model systems are in good agreement with those of the Pt–Ni practical catalysts, showing the synergetic effect of surface Ni oxide and subsurface Ni on the CO oxidation reaction. We believe that

the similar reaction mechanism may be active in other Pt-based bimetallic catalytic systems for CO oxidation. Second, the present work demonstrates that activation in H_2, which is frequently applied in catalyst preparation, is a simple but effective route to manipulate the surface configuration of multicomponent catalysts. The strong dependence of catalytic performance on the preparation condition as shown here indicates a need to transform the art of catalyst preparation into a science. Finally, it should be noted that the surface structure of the supported catalyst nanoparticles is quite complex, in particular, for the multicomponent catalysts. Nevertheless, a bridge between model catalytic systems and practical catalysts can be made, such that the fundamental understanding derived from the model catalytic systems helps the rational design of the highly efficient supported catalysts.

References

1. Rodriguez JA, Goodman DW (1992) The nature of the metal–metal bond in bimetallic surfaces. Science 257(5072):897–903
2. Rodriguez JA (1996) Physical and chemical properties of bimetallic surfaces. Surf Sci Rep 24 (7–8):225–287
3. Besenbacher F et al (1998) Design of a surface alloy catalyst for steam reforming. Science 279(5358):1913–1915
4. Nashner MS et al (1998) Core Shell inversion during nucleation and growth of bimetallic Pt/Ru nanoparticles. J Am Chem Soc 120(32):8093–8101
5. He JH et al (2003) Facile fabrication of Ag-Pd bimetallic nanoparticles in ultrathin TiO_2-gel films: nanoparticle morphology and catalytic activity. J Am Chem Soc 125(36):11034–11040
6. Chen MS et al (2005) The promotional effect of gold in catalysis by palladium-gold. Science 310(5746):291–293
7. Enache DI et al (2006) Solvent-free oxidation of primary alcohols to aldehydes using Au-Pd/TiO_2 catalysts. Science 311(5759):362–365
8. Stamenkovic V et al (2006) Changing the activity of electrocatalysts for oxygen reduction by tuning the surface electronic structure. Angew Chem Int Ed 45(18):2897–2901
9. Stamenkovic VR et al (2006) Effect of surface composition on electronic structure, stability, and electrocatalytic properties of Pt-transition metal alloys: Pt-skin Versus Pt-skeleton surfaces. J Am Chem Soc 128(27):8813–8819
10. Koh S, Strasser P (2007) Electrocatalysis on bimetallic surfaces: modifying catalytic reactivity for oxygen reduction by voltammetric surface dealloying. J Am Chem Soc 129(42):12624–12625
11. Zhang J et al (2007) Stabilization of platinum oxygen-reduction electrocatalysts using gold clusters. Science 315(5809):220–222
12. Chen JG, Menning CA, Zellner MB (2008) Monolayer bimetallic surfaces: experimental and theoretical studies of trends in electronic and chemical properties. Surf Sci Rep 63(5):201–254
13. Liu ZF, Jackson GS, Eichhorn BW (2010) PtSn intermetallic, core-shell, and alloy nanoparticles as co-tolerant electrocatalysts for H_2 oxidation. Angew Chem Int Ed 49 (18):3173–3176
14. Nilekar AU et al (2010) Preferential CO Oxidation in hydrogen: reactivity of core-shell nanoparticles. J Am Chem Soc 132(21):7418–7428
15. Alayoglu S et al (2008) Ru-Pt core-shell nanoparticles for preferential oxidation of carbon monoxide in hydrogen. Nat Mater 7(4):333–338

16. Alayoglu S, Eichhorn B (2008) Rh-Pt bimetallic catalysts: synthesis, characterization, and catalysis of core-shell, alloy, and monometallic nanoparticles. J Am Chem Soc 130 (51):17479–17486
17. Nashner MS et al (1996) Bimetallic catalyst particle nanostructure. evolution from molecular cluster precursors. J Am Chem Soc 118(51):12964–12974
18. Creemers C, Deurinck P (1997) Platinum segregation to the (111) surface of ordered $Pt_{80}Fe_{20}$: LEIS results and model simulations. Surf Interface Anal 25(3):177–190
19. Stamenkovic VR et al (2003) Surface chemistry on bimetallic alloy surfaces: adsorption of anions and oxidation of CO on $Pt_3Sn(111)$. J Am Chem Soc 125(9):2736–2745
20. Knudsen J et al (2007) A Cu/Pt near-surface alloy for water-gas shift catalysis. J Am Chem Soc 129(20):6485–6490
21. Koh S et al (2007) Structure-activity-stability relationships of Pt-Co alloy electrocatalysts in gas-diffusion electrode layers. J Phys Chem C 111(9):3744–3752
22. Stamenkovic VR et al (2007) Improved oxygen reduction activity on $Pt_3Ni(111)$ via increased surface site availability. Science 315(5811):493–497
23. Stamenkovic VR et al (2007) Trends in electrocatalysis on extended and nanoscale Pt-bimetallic alloy surfaces. Nat Mater 6(3):241–247
24. Chen S et al (2008) Enhanced activity for oxygen reduction reaction on "Pt_3CO" nanoparticles: direct evidence of percolated and sandwich-segregation structures. J Am Chem Soc 130(42):13818–13819
25. Scott RWJ et al (2011) Selective Aerobic oxidation of crotyl alcohol using AuPd core-shell nanoparticles. ACS Catal 1(5):425–436
26. Paulus UA et al (2002) Oxygen reduction on high surface area Pt-based alloy catalysts in comparison to well defined smooth bulk alloy electrodes. Electrochim Acta 47(22–23): 3787–3798
27. Stamenkovic V et al (2002) Surface composition effects in electrocatalysis: kinetics of oxygen reduction on well-defined Pt_3Ni and Pt_3Co alloy surfaces. J Phys Chem B 106 (46):11970–11979
28. Nilekar AU et al (2007) Bimetallic and ternary alloys for improved oxygen reduction catalysis. Top Catal 46(3–4):276–284
29. Yano H et al (2007) Oxygen reduction activity of carbon-supported Pt-M (M = V, Ni, Cr Co, and Fe) Alloys prepared by nanocapsule method. Langmuir 23(11):6438–6445
30. Chen S et al (2009) Origin of oxygen reduction reaction activity on "Pt_3Co" nanoparticles: atomically resolved chemical compositions and structures. J Phys Chem C 113(3):1109–1125
31. Zhou WP et al (2009) Improving electrocatalysts for O_2 reduction by fine-tuning the Pt-support interaction: Pt monolayer on the surfaces of a $Pd_3Fe(111)$ single-crystal alloy. J Am Chem Soc 131(35):12755–12762
32. Kim J, Lee Y, Sun SH (2010) Structurally ordered FePt nanoparticles and their enhanced catalysis for oxygen reduction reaction. J Am Chem Soc 132(14):4996–4997
33. Gokhale AA, Dumesic JA, Mavrikakis M (2008) On the mechanism of low-temperature water gas shift reaction on copper. J Am Chem Soc 130(4):1402–1414
34. Song CS et al (2011) Oxygen-Enhanced water gas shift on ceria-supported Pd-Cu and Pt-Cu bimetallic catalysts. J Catal 277(1):46–53
35. Mohamed MM, Khairou KS (2011) Fabrication and characterization of bimetallic Pt-Au nanowires supported on FSM-16 and their catalytic activities toward water-gas shift reaction. J Colloid Interf Sci. 354(1):100–108
36. Jugnet Y et al (2011) Preferential CO oxidation in a large excess of hydrogen on Pt_3sn surfaces. J Catal 278(2):239–245
37. Margitfalvi JL et al (2001) In situ characterization of $Sn-Pt/SiO_2$ catalysts used in low temperature oxidation of CO. J Catal 203(1):94–103
38. Kotobuki M et al (2005) Reaction Mechanism of preferential oxidation of carbon monoxide on Pt, Fe, and Pt-Fe/mordenite catalysts. J Catal 236(2):262–269
39. Liu XS, Korotkikh O, Farrauto R (2002) Selective catalytic oxidation of CO in H_2: structural study of Fe oxide-promoted Pt/alumina catalyst. Appl Catal A Gen 226(1–2):293–303

40. Ko EY et al (2007) Supported Pt-Co catalysts for selective CO oxidation in a hydrogen-rich stream. Angew Chem Int Ed 46(5):734–737

41. Ko EY et al (2006) Pt-Ni/Gamma-Al$_2$O$_3$ catalyst for the preferential CO oxidation in the hydrogen stream. Catal Lett 110(3–4):275–279

42. Mu R et al (2011) Synergetic effect of surface and subsurface Ni species at Pt-Ni bimetallic catalysts for CO oxidation. J Am Chem Soc 133(6):1978–1986

43. Castillejos E et al (2009) An efficient strategy to drive nanoparticles into carbon nanotubes and the remarkable effect of confinement on their catalytic performance. Angew Chem Int Ed 48(14):2529–2533

44. Kitchin JR et al (2003) Elucidation of the active surface and origin of the weak metal-hydrogen bond on Ni/Pt(111) bimetallic surfaces: a surface science and density functional theory study. Surf Sci 544(2–3):295–308

45. Wruck DA, Rubin M (1993) Structure and electronic-properties of electrochromic NiO films. J Electrochem Soc 140(4):1097–1104

46. Bender M, Alshamery K, Freund HJ (1994) Sodium adsorption and reaction on NiO(111)/Ni (111). Langmuir 10(9):3081–3085

47. Kinne M et al (2004) Coadsorption of D$_2$O and CO on Pt(111) studied by in situ high-resolution X-ray photoelectron spectroscopy. Langmuir 20(5):1819–1826

48. Hagendorf C et al (2006) Pressure-dependent Ni-O phase transitions and Ni oxide formation on Pt(111): an in situ STM study at elevated temperatures. Phys Chem Chem Phys 8 (13):1575–1583

49. Agnoli S et al (2005) Experimental and theoretical study of a surface stabilized monolayer phase of nickel oxide on Pd(100). J Phys Chem B 109(36):17197–17204

50. Tsilimis G, Kutzner J, Zacharias H (2003) Photoemission study of clean and c(4 × 2)-2CO-covered Pt(111) using high-harmonic radiation. Appl Phys A Mater 76(5):743–749

51. Tsilimis G et al (2004) Observation of high-energy Pt(111) surface resonances excited by laser-generated XUV radiation. Appl Phys A-mater 78(2):177–181

52. Xu Y, Ruban AV, Mavrikakis M (2004) Adsorption and dissociation of O$_2$ on Pt-Co and Pt-Fe alloys. J Am Chem Soc 126(14):4717–4725

53. Menning CA, Chen JG (2008) Thermodynamics and kinetics of oxygen-induced segregation of 3d metals in Pt-3d-Pt(111) and Pt-3d-Pt(100) bimetallic structures. J Chem Phys 128 (16):164703

54. Fu Q et al (2010) Interface-confined ferrous centers for catalytic oxidation. Science 328 (5982):1141–1144

55. Yao YX et al (2010) Growth and characterization of two-Dimensional FeO nanoislands supported on Pt(111). J Phys Chem C 114:17069–17079

56. Rodriguez JA et al (2007) Activity of CeOx and TiOx nanoparticles grown on Au(111) in the water-gas shift reaction. Science 318(5857):1757–1760

57. Besenbacher F et al (2007) Size-dependent structure of MoS$_2$ nanocrystals. Nat Nanotechnol 2(1):53–58

58. Tuxen A et al (2010) Size threshold in the dibenzothiophene adsorption on MoS$_2$ nanoclusters. ACS Nano 4(8):4677–4682

59. Su HY, Bao XH, Li WX (2008) Modulating the reactivity of Ni-containing Pt(111)-skin catalysts by density functional theory calculations. J Chem Phys. 128(19):194707

60. Ma YG, Balbuena PB (2008) Pt surface segregation in bimetallic Pt$_3$M alloys: a density functional theory study. Surf Sci 602(1):107–113

61. Menning CA, Chen JG (2010) Regenerating Pt-3d-Pt model electrocatalysts through oxidation-reduction cycles monitored at atmospheric pressure. J Power Sources 195 (10):3140–3144

62. Zheng F et al (2011) In-situ X-ray absorption study of evolution of oxidation states and structure of cobalt in Co and CoPt bimetallic nanoparticles (4 nm) under reducing (H$_2$) and oxidizing (O$_2$) environments. Nano Lett 11(2):847–853

63. Mayrhofer KJJ et al (2009) Adsorbate-induced surface segregation for core-shell nanocatalysts. Angew Chem Int Edit 48(19):3529–3531

64. Mani P, Srivastava R, Strasser P (2008) Dealloyed Pt-Cu core-shell nanoparticle electrocat-alysts for use in PEM fuel cell cathodes. J Phys Chem C 112(7):2770–2778
65. Strasser P et al (2010) Lattice-strain control of the activity in dealloyed core-shell fuel cell catalysts. Nat Chem 2(6):454–460
66. Strasser P (2009) dealloyed core-shell fuel cell electrocatalysts. Rev Chem Eng 25 (4):255–295
67. Iwasawa Y et al (2003) Time scale and elementary steps of Co-induced disintegration of surface rhodium clusters. Angew Chem Int Edit 42(39):4795–4799
68. Jacques SDM et al (2009) Recent progress in the use of in situ X-ray methods for the study of heterogeneous catalysts in packed-bed capillary reactors. Catal Today 145(3–4):204–212
69. Lobo RF, Foster AJ (2010) Identifying reaction intermediates and catalytic active sites through in situ characterization techniques. Chem Soc Rev 39(12):4783–4793
70. Caballero A et al (2008) Morphology changes induced by strong metal-support interaction on a Ni-Ceria catalytic system. J Catal 257(2):307–314
71. Iwasawa Y (2003) In situ Characterization of supported metal catalysts and model surfaces by time-resolved and three-dimensional XAFS techniques. J Catal 216(1–2):165–177
72. Grunwaldt JD et al (2011) Identification of the active species generated from supported Pd catalysts in heck reactions: an in situ quick scanning EXAFS investigation. J Am Chem Soc 133(11):3921–3930

Chapter 4
Modulating the Structure and Reactivity of Pt–Ni Catalysts

We show that the cycling oxidative and reductive treatments at variable temperatures can reversibly alternate the surface structure and reactivity of Pt–Ni bicomponent catalysts. Low-temperature ($\sim$423 K) oxidation of Pt-skin structure (Pt/Ni/Pt(111)) induces part of Ni diffuse outward and form NiO on surface. After further oxidation at a higher temperature of 623 K, the catalysts are completely encapsulated by NiO. When the Pt@NiO core–shell structure is reduced at low temperature ($\sim$423 K), part of Ni starts to diffuse inward. Upon the reduction at a high temperature of 623 K, the formation of Pt-skin surface is observed. The catalysts pretreated at low temperatures show high CO oxidation reactivity due to the formation of the sandwich-like structure with surface and subsurface Ni species.

4.1 Introduction

Modulating the performance of heterogeneous catalysts is often achieved through the controllable preparation of their size, shape, and other factors [1–7]. Therefore, numerous works are focused on the controllable preparation of catalysts. Furthermore, the post-treatments are also expected to influence the performance of catalysts significantly [8–15]. Nevertheless, the natures of preparation methods and post-treatments on the performance of catalysts are still unclear in a lot of catalytic reactions.

Among various post-treatment methods, reduction and oxidation (redox) are simple and often employed to activate nanoparticle catalysts. Numerous works have shown that the redox treatments could significantly influence the performance of catalysts, especially for bicomponent catalysts [16–20]. This is because the redox treatments will not only affect the size and shape of bicomponent catalysts, but also induce the surface segregation and other mass transfer processes [21–23]. For example, several recent works have shown the reversible modulation of surface

structures and reactivity of Pt–Fe [16], Pt–Co [19], Pt–Ni [20, 24], and RhPd [17, 18] bicomponent catalysts via redox treatments.

In Chap. 3, we investigated the influence of VT (Variable Temperature) reduction treatment on the surface structure and reactivity of Pt–Ni catalysts. We found the VT reductions exhibited a "Goldilocks effect" on the performance of Pt–Ni catalysts, i.e., the catalyst reduced at medium temperature showing the best reactivity. But how the oxidation treatments affect the Pt–Ni catalysts is still unclear. This chapter will focus on the effect of VT redox treatments on the surface structure and performance of Pt–Ni bicomponent catalysts.

4.2 Ni–Pt(111) Model Catalytic Systems

First, we prepare various Ni–Pt(111) model surfaces in UHV chamber. As shown in Chap. 3, Pt-skin surface with subsurface Ni (Pt/Ni/Pt(111)) can be obtained by annealing 1.3 ML Ni/Pt(111) in UHV condition at 800 K for 5 min. XPS studies show the ratio of Ni2p/Pt4f decreases as the annealing temperature increases (Annealing, UHV. Figure 4.1). The attenuation of XPS Ni2p peak can be attributed to the diffusion of Ni from surface to subsurface and bulk region during annealing treatments. The similar phenomena have been observed on other Pt-based bicomponent systems as well [16, 25–27]. Since the lattice mismatch between Pt and Ni, the Pt-skin surface with subsurface Ni shows the white line structure in STM image (Fig. 4.2a) [16, 25, 26].

The shadow region in Fig. 4.1 gives the evolution of XPS Ni2p/Pt4f ratio of Pt/Ni/Pt(111) surface as a function of oxidized temperature in 5.2×10^{-7} mbar O_2 atmosphere. We find the Ni2p/Pt4f ratio slightly increases at the oxidized temperatures lower than 600 K. Furthermore, both the binding energy of Ni2p3/2 peak and microscopic Pt-skin feature do not change after the oxidation in 5.2×10^{-7} mbar O_2 at 600 K for 5 min. This indicates the Pt-skin surface is stable in 5.2×10^{-7} mbar O_2 up to 600 K. While the Ni2p/Pt4f ratio increases with 80%

Fig. 4.1 XPS Ni2p/Pt4f ratio of 1.3 ML Ni/Pt(111) model surfaces after UHV annealing, VT oxidation and VT reduction at various temperatures for 5 min. *a–f* Room temperature, 400, 500, 600, 700, and 800 K
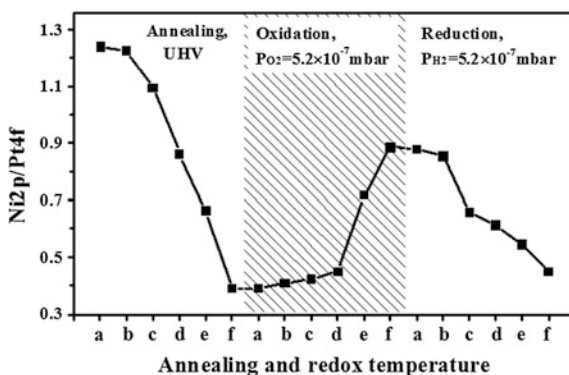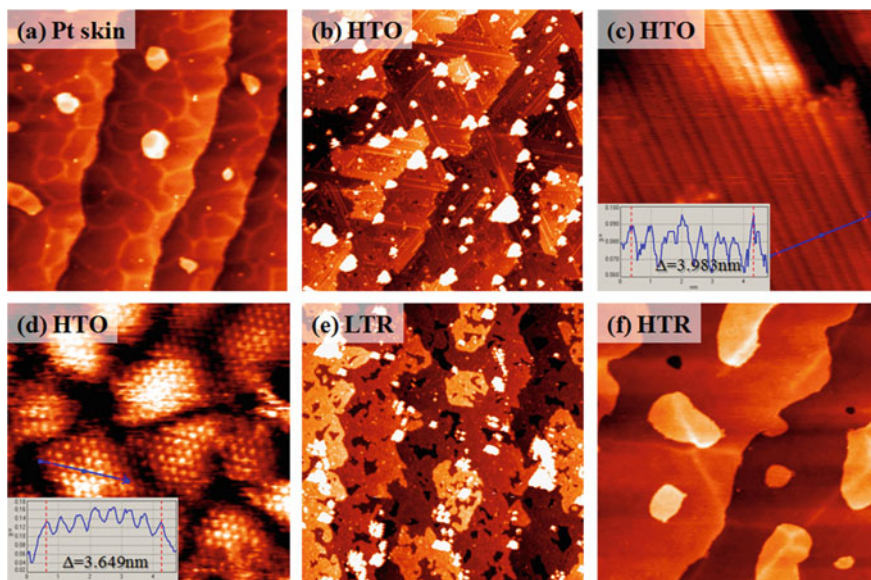
Fig. 4.2 STM images of **a** Pt-skin surface with subsurface Ni, Pt/Ni/Pt(111), **b** NiO/Pt(111) produced by the HTO treatment of Pt/Ni/Pt(111), **c** one-dimensional NiO nanowire in (**b**), **d** highly resolved three-dimensional NiO structure of white area in (**b**), **e** metallic Ni on Pt(111) produced by the LTR treatment of NiO/Pt (111), and **f** Pt-skin surface with subsurface Ni produced by HTR treatment from (**e**). Image conditions: **a** 200 nm × 200 nm, −0.275 V, 0.957 nA; **b** 200nm × 200 nm, 2.5 V, 0.015 nA; **c** 12 nm × 12 nm, −0.365 V, 1.553 nA; **d** 15 nm × 15 nm, −0.262 V, 1.1 nA; **e** 200 nm × 200 nm, −2.0 V, 0.015 nA; **f** 200 nm × 200 nm, −2.5 V, 1.0 nA. Adapted with permission from Ref. [28]. Copyright (2011) American Chemical Society

after the oxidation at 700 K for 5 min, indicating part of Ni is driven to surface. For oxidation of Pt/Ni/Pt(111) surface at 800 K, the Ni2p/Pt4f ratio increases from 0.41 to 0.91. So the oxidation condition of $P_{O2} = 5.2 \times 10^{-7}$ mbar at 700 K is named as low-temperature oxidation (LTO). In LTO of Pt/Ni/Pt(111) surface, the binding energy of Ni2p3/2 shifts from 852.7 to 853.1 eV, indicating subsurface region Ni segregates to surface and forms NiO (Fig. 4.3). As expected, high-temperature oxidation (HTO) of Pt/Ni/Pt(111) surface at 800 K induces more Ni to segregate to surface and form NiO.

STM results show the HTO-treated Pt/Ni/Pt(111) is fully covered by NiO (Fig. 4.2b). As shown in high-resolution STM images, the formed NiO presents two different structures, one-dimensional nano-lines (Fig. 4.2c) and three-dimensional islands (Fig. 4.2d) [29].

Reducing NiO/Pt(111) sample at various temperatures, the opposite mass transfer process between Ni and Pt substrate was observed (Fig. 4.1). We find the binding energy of Ni2p3/2 peak changes from 853.1 to 852.7 eV again after the reduction in 5.2×10^{-7} mbar H_2 at 400 K for 5 min. However, the Ni2p/Pt4f ratio
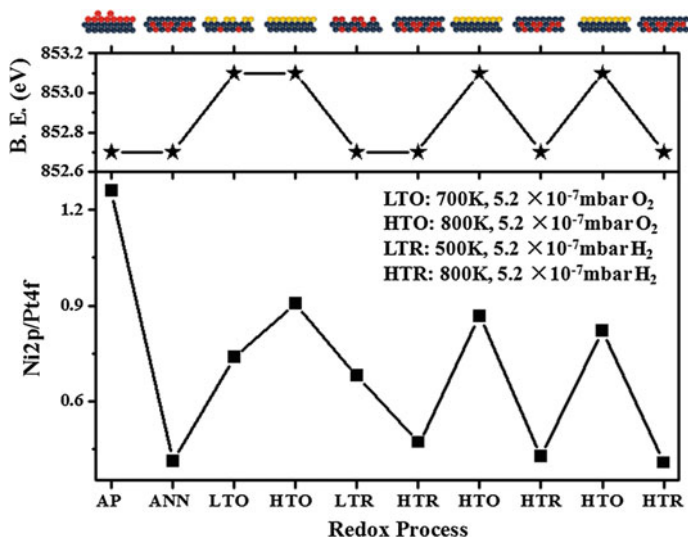
Fig. 4.3 XPS Ni2p/Pt4f ratio (*lower*) and binding energy (B. E.) of Ni2p3/2 (*upper*) as a function of the sequential redox treatments. AP: as-prepared 1.3 ML Ni/Pt(111); ANN: annealing the 1.3 ML Ni/Pt(111) in UHV at 800 K. The insets show schematics of the various surfaces. Pt: *gray ball*; metallic Ni: *red ball*; oxidized Ni: *yellow ball*. Reprinted with permission from Ref. [28]. Copyright (2011) American Chemical Society

is almost unchanged after reduction at 400 K. These indicate the surface NiO is reduced to metallic Ni, but still on the surface. Reduction of NiO/Pt(111) surface at 500 K induces the Ni2p/Pt4f ratio to decrease with 25%, as shown in Fig. 4.3, indicating part of surface Ni diffuses into subsurface region. It is found that some hole structures with one atomic height appear on surface after reduction at 500 K (Fig. 4.2e). As the reduction temperature increases, the Ni2p/Pt4f ratio decreases gradually (Fig. 4.1). We find the Ni2p/Pt4f ratio decreases with 48% after reduction at 800 K. Simultaneously, Pt-skin surface features are observed in STM image (Fig. 4.2f). So we define the reduction condition of $P_{H2} = 5.2 \times 10^{-7}$ mbar at 500 K as low-temperature reduction (LTR), where NiO can be reduced to metallic state and locate on Pt surface.

The driven forces which induce surface segregation of bicomponent systems can be mainly attributed to three aspects: (1) the component with lower surface free energy is prone to segregate to surface for lowering the total surface energy [30–32], (2) the component with large atomic radius is inclined to segregate to surface when the difference is larger than 10% [33], and (3) the exposing gas may also induce surface segregation of a component which interacts with gas stronger [20].

For Pt–Ni bicomponent systems, the reduction at elevated temperature and UHV annealing treatment may induce surface segregation of Pt, because atomic radius of Pt is larger than the atomic radius of Ni ($R_{Pt} = 1.39$ Å, $R_{Ni} = 1.24$ Å). Since the interaction of Ni and O is strong and the surface free energy of Ni is lower than that of

Pt, the oxidation treatment at elevated temperature is expected to drive Ni to surface and form NiO. More interestingly, Ni2p/Pt4f ratio presents a reversible oscillation under alternating redox treatments at various temperatures in Fig. 4.3. This means the Pt/Ni/Pt(111) and NiO/Pt(111) surfaces can be repeatedly generated in cycled redox treatments. DFT calculations have demonstrated that subsurface Ni was a thermodynamically stable structure, which played a critical role in the structural switch between Pt/Ni/Pt(111) and NiO/Pt(111) [34, 35]. Since part of Ni may diffuse into the deeper bulk region of Pt substrate after reduction, and since only subsurface Ni can be driven to surface in the following oxidation treatment, a small decrease of Ni2p/Pt4f ratio is observed after several alternating redox cycles (Fig. 4.3).

Then CO and O_2 are utilized as the probe molecules to detect surface structures of Ni–Pt(111) model systems after alternating VT redox cycles. As shown in Fig. 4.4a, the binding energy of XPS O1s on CO/Pt(111) surface locates at 531.3 and 533.0 eV, which are assigned to bridging and linear adsorbed CO, respectively [36]. Early works have reported that the subsurface metal atoms could induce the d-band center of surface Pt to shift away from Fermi level and thus weaken the interaction between adsorbates and Pt surface [25, 27, 37–42]. Since HTR treatment of Ni–Pt(111) model system produces a Pt-skin surface with subsurface Ni, only a weaker O1s peak from linear adsorbed CO is observed in Fig. 4.4a CO/HTR. The similar depression of bridging CO adsorption has been observed on Pt/Fe/Pt(111) surface as well [43]. After LTO treatment of Pt-skin surface (Pt/Ni/Pt(111)) and CO adsorption, XPS studies show two O1s peaks, the stronger peak at 529.7 eV is from NiO and the weaker peak at 533.0 eV is from bridging CO (Fig. 4.4a CO/LTO).
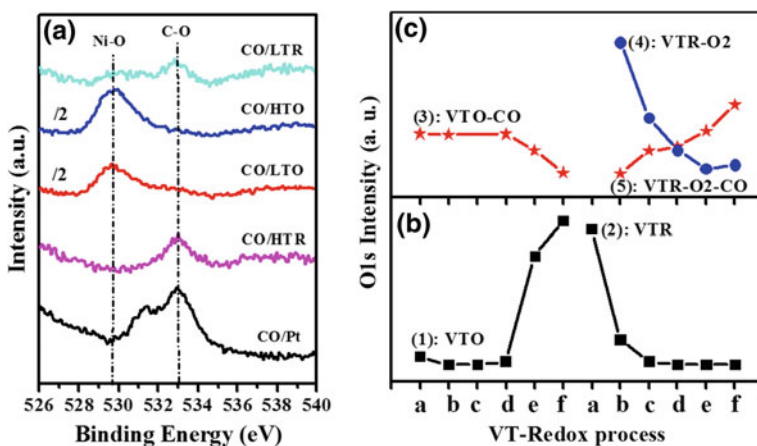
Fig. 4.4 **a** XPS O1s spectra from the CO-saturated surfaces treated by the various processes sequentially (from *bottom* to *up*); Adapted with permission from Ref. [28]. Copyright (2011) American Chemical Society. **b** XPS O1s intensity of Pt/Ni/Pt(111) surface treated by VT oxidation in 5.2×10^{-7} mbar O_2 for 5 min (VTO) and NiO/Pt(111) surface treated by VT reduction in 5.2×10^{-7} mbar H_2 for 5 min (VTR); **c** XPS O1s intensity of CO adsorbed on Pt/Ni/Pt(111) surfaces pretreated by VTO (VTO-CO), O_2 and then CO adsorbed on NiO/Pt(111) surfaces pretreated by VTR (VTR-O_2, and VTR-O_2-CO). *a–f* RT, 400, 500, 600, 700, and 800 K

This indicates the LTO treatment of Pt-skin surface can create a sandwich-like surface with Ni patches on surface and part of Ni in subsurface region. Since XPS O1s peak from CO molecules cannot be observed after HTO treatment, we infer a continuous NiO overlayer is formed on Pt surface (Fig. 4.4a CO/HTO). In addition, CO/LTR surface shows XPS O1s peaks from both NiO and bridging CO on bare Pt area, indicating LTR treatment of NiO/Pt(111) surface produces a sandwich-like structure again.

Figure 4.4b, c further illustrates the surface structures of Ni–Pt(111) model systems after VT redox treatments. The evolution of O1s peak intensity from Pt/Ni/Pt(111) surfaces as a function of oxidation temperature (Fig. 4.4b(1)) and the following CO adsorption (Fig. 4.4c(3)) indicate LTO treatment can generate a bicomponent surface configuration exposing both Ni and Pt on the surface.

As shown in Fig. 4.4b(2), NiO/Pt(111) can be completely reduced under LTR condition. It is well known that O_2 can dissociative adsorb on both Pt and Ni surfaces. The following CO exposure will eliminate O atoms adsorbed on Pt surface through $CO + O \rightarrow CO_2$ reaction. In contrast, the O atoms adsorbed on Ni surface are stable in CO atmosphere at room temperature due to the strong interaction between O and Ni. So the method consists of O_2 dosing and a followed CO exposure was adopted to determine the surface structure of NiO/Pt(111) after VT reduction (Fig. 4.4c(5)). At first, O_2 adsorption on NiO/Pt(111) after VT reductions was studied (Fig. 4.4c(4)). Based on the decreasing trend of O1s peak intensity from O_2 adsorbed surfaces, we infer more and more Ni diffuse into subsurface region with reduction temperature increases. The following CO exposure experiments also prove LTR treatment of NiO/Pt(111) surface lead to a sandwich-like structure.

4.3 Pt–Ni/CB Nanoparticle Catalysts

Over model Ni–Pt(111) catalytic systems, we show the NiO/Pt(111) and Pt/Ni/Pt (111) surfaces can be reversible achieved through alternating HTO and HTR treatments. LTO of Pt/Ni/Pt(111) and LTR of NiO/Pt(111) produce a sandwich-like surface with Ni patches on surface and part of Ni in subsurface. Since the material gap and pressure gap between model catalytic systems in UHV chamber and supported nanoparticle catalysts under working condition [7], we further investigate the influence of VT redox treatments on the structure and performance of supported Pt–Ni nanoparticle catalysts. The combination of surface science studies and supported nanoparticle catalyst provide a promising strategy to understand the correlation of treatment—structure—performance of Pt–Ni bicomponent catalysts.

From investigations of model surfaces, we find XPS is a very useful technique to study the surface structure of Pt–Ni bicomponent catalysts. In order to acquire decent XPS signal, we deposit high-density Pt–Ni bicomponent nanoparticles on sputtered HOPG surface (Pt–Ni/HOPG). TEM studies show the size distribution of Pt–Ni/HOPG model sample is very similar to that of supported Pt–Ni/CB catalysts (Fig. 4.5). Figure 4.6a displays the Ni2p/Pt4f ratio of Pt–Ni/HOPG model sample
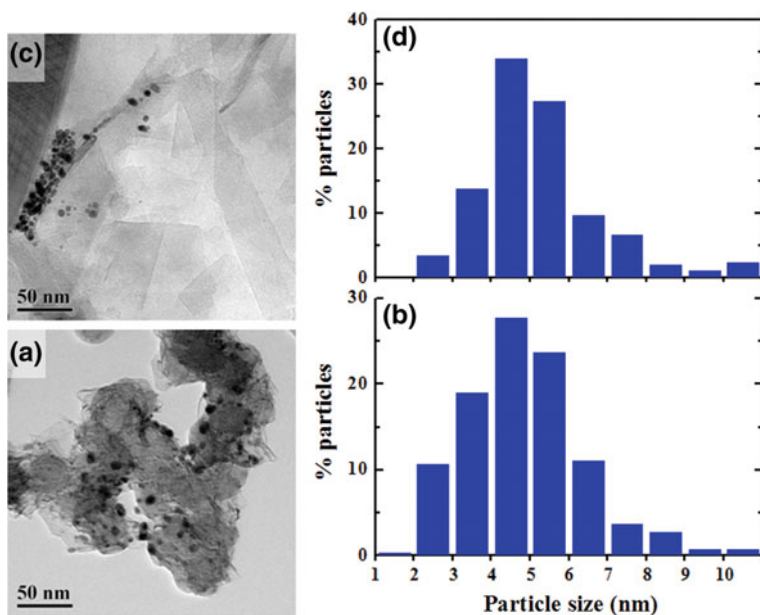
Fig. 4.5 TEM images and size distribution of Pt–Ni/CB catalysts (**a**, **b**) and exfoliated Pt–Ni/HOPG sample (**c**, **d**). High-density Pt–Ni nanoparticles were deposited on a sputtered HOPG surface by a solution deposition method, and the ratio of Pt to Ni is controlled at 1:1
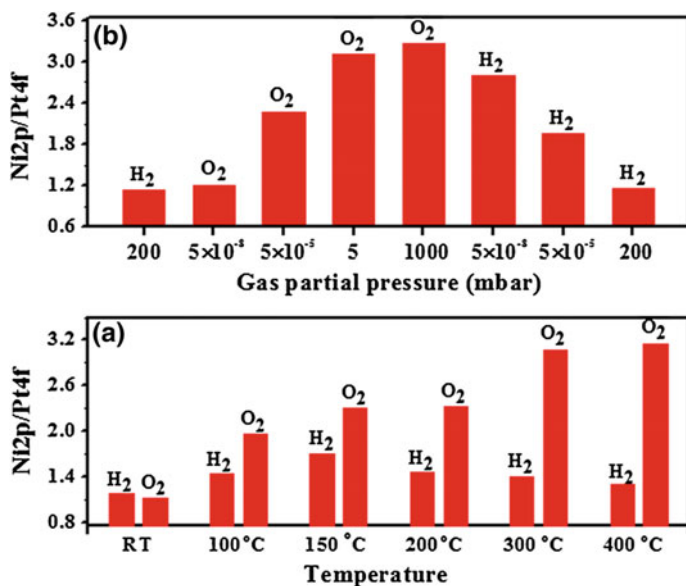

Fig. 4.6 a XPS intensity ratio of Ni2p/Pt4f on Pt–Ni/HOPG sample treated in alternating reduction (20% H_2, 0.1 MPa) and oxidation (100% O_2, 0.1 MPa) cycles at various temperatures in the high pressure reaction cell attached to the XPS chamber. **b** XPS intensity ratio of Ni2p/Pt4f on Pt–Ni/HOPG sample treated at 573 K in redox atmospheres with various partial pressures

as a function of redox temperatures. We find the oscillation of the Ni2p/Pt4f ratio reaches the maximum at 573 and 673 K, indicating the NiO overlayers and Pt-rich surface can be produced after oxidation and reduction, respectively. Since the oscillation of Ni2p/Pt4f ratio at 473 K is smaller than that at 573 K (Fig. 4.6a), we infer a sandwich-like Pt–Ni nanoparticle can be prepared at this medium temperature. In addition, the influence of gas partial pressure on the surface structure of Pt–Ni/HOPG model sample is also studied. As expected, we find the Ni2p/Pt4f ratio increases as the gas pressure increases at 573 K (Fig. 4.6b).

Figure 4.7a shows the reversible up-down oscillation of Pt4f peak intensity on Pt–Ni/HOPG model sample after alternating reduction and oxidation cycles at 573 K. Interestingly, the up-down oscillation of Pt4f peak differs from that of Ni2p peak which exhibits a opposite down-up oscillation under same redox cycles. For reduction of Pt–Ni/HOPG sample at 573 K, the binding energies of Pt4f7/2 and Ni2p3/2 peaks locate at 71.2 and 852.6 eV, indicating Pt and Ni can be reduced to metallic state completely (Figs. 4.7a, b, and 4.8c). Furthermore, Ni2p/Pt4f ratio is observed to decrease after reduction at 573 K. The reason should be attributed to the surface segregation of Pt under reduction. Deconvoluting of Pt4f peak on Pt–Ni/HOPG sample after oxidation at 573 K, we find the main Pt4f peak still locates at 71.2 eV along with a shoulder peak at 72.4 eV (Fig. 4.8d). We find that 20% of Pt from Pt–Ni/HOPG sample is oxidized after oxidation at 573 K. Simultaneously, only a sharp Ni2p peak located at 853.9 eV can be observed after oxidation, indicating that Ni is oxidized completely (Fig. 4.7b). After the oxidation at 573 K, the Ni2p/Pt4f ratio increases significantly due to the formation of NiO overlayers. More importantly, the reversible up-down oscillation of Ni2p/Pt4f ratio is also observed after alternating oxidation and reduction treatments, which illustrates a structural switch between NiO overlayers and Pt-rich surface.

For comparison, we investigate the mono-component Pt/HOPG sample under alternating redox treatments. As shown in Fig. 4.8e, the Pt4f/C1s ratio is almost constant under redox treatments indicating Pt nanoparticles do not agglomerate together. Since the bonding energy of Pt–Ni (5.52 eV) is close to that of Pt–Pt (5.77 eV) [45], the stability of Pt–Ni bicomponent nanoparticles should be similar to that of Pt nanoparticles. So the sintering of bicomponent can be excluded after redox treatments. In contrast to the Pt–Ni bicomponent nanoparticles, we find Pt/HOPG sample is more prone to be oxidized in oxidation. As shown in Fig. 4.8b, about 46% of Pt from Pt/HOPG sample was oxidized, while only ∼20% of Pt from Pt–Ni/HOPG sample was oxidized. This difference can be attributed to the formation of NiO overlayers on Pt surface, which protects Pt nanoparticles from further oxidation.

Studies of Pt–Ni/HOPG model samples reveal the surface structure of Pt–Ni nanoparticles can be reversible modulated by alternating redox treatments. High-temperature oxidation (573 K, 2 h) of Pt–Ni bicomponent nanoparticles produces a core–shell structure where NiO overlayers encapsulate on Pt surface, i.e., Pt@NiO. High-temperature reduction (573 K, 2 h) of Pt–Ni bicomponent nanoparticles creates a Pt-rich surface. Furthermore, a sandwich-like structure of
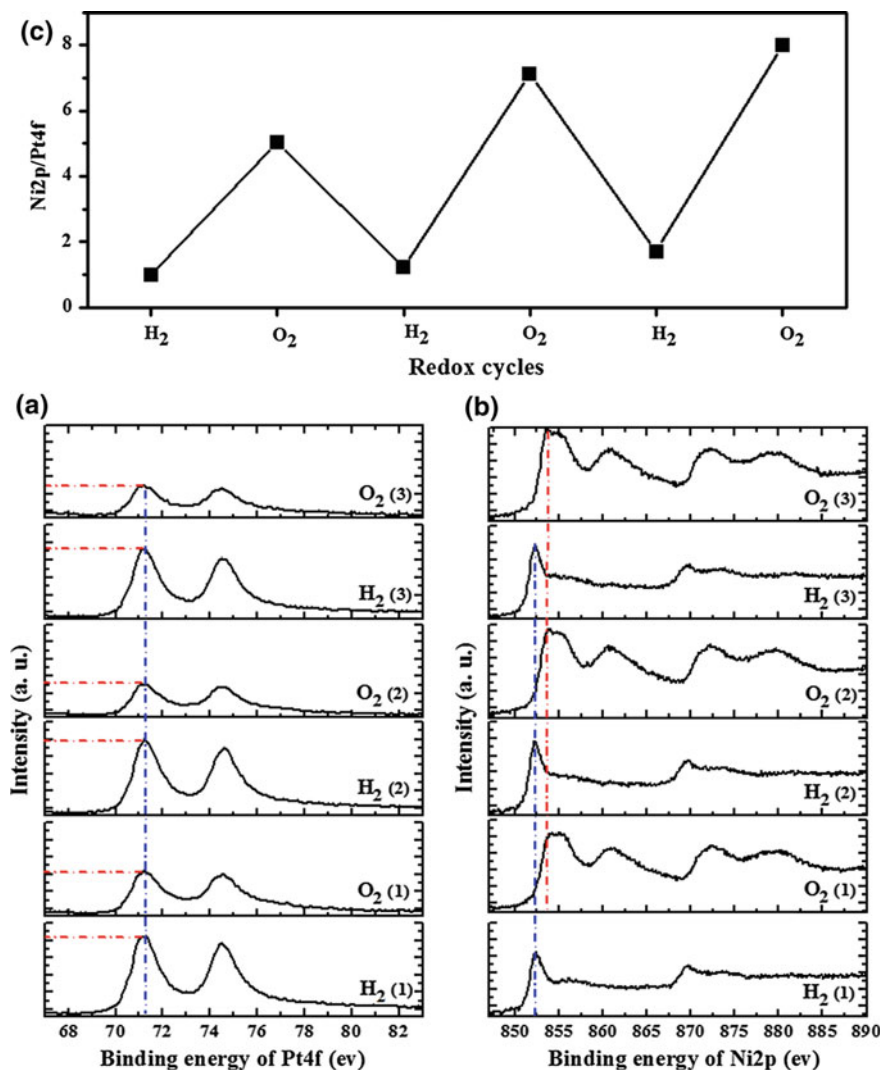
Fig. 4.7 a XPS Pt4f and **b** Ni2p peaks from the Pt–Ni/HOPG sample treated in alternating oxidizing (100% O_2, 0.1 MPa) and reducing (20% H_2, 0.1 MPa) atmospheres at 573 K. **c** XPS Ni2p/Pt4f intensity ratio as a function of the sequential redox treatments. Reprinted from Ref. [44], Copyright (2009), with permission from Elsevier

Pt–Ni nanoparticles with both surface and subsurface Ni can be achieved under low-temperature redox treatment (473 K, 2 h).

Based on the results from model catalytic systems, the practically Pt–Ni bicomponent catalysts were prepared on carbon black (Pt–Ni/CB). The loading amount of Pt and Ni was controlled at 4 wt% and 1.2 wt%, respectively (mole
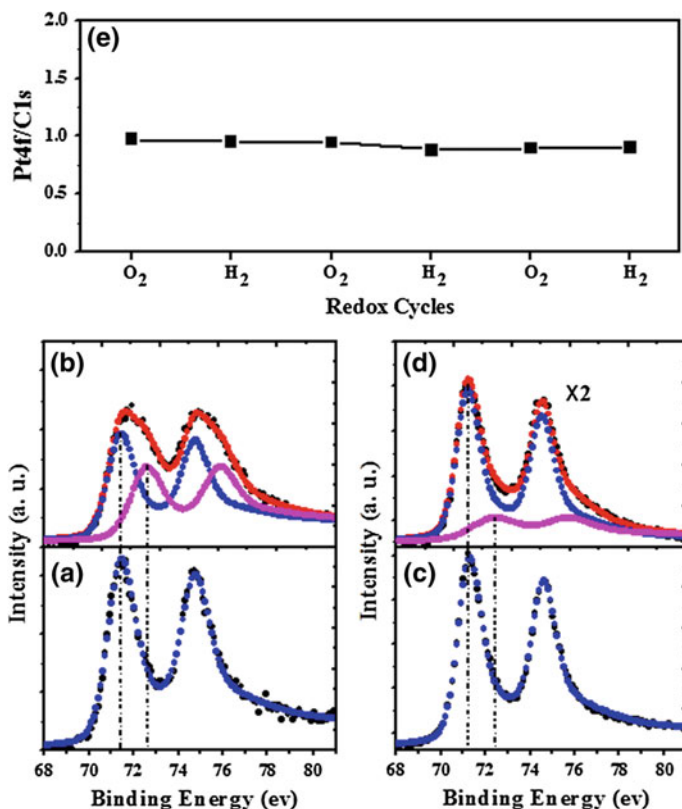
Fig. 4.8 XPS Pt4f peaks of Pt/HOPG (**a**, **b**) and Pt–Ni/HOPG (**c**, **d**) samples treated in alternating reducing (**a**, **c**) and oxidizing (**b**, **d**) atmospheres at 573 K for 2 h, and **e** the Pt4f/C1s ratio of Pt/HOPG sample as a function of redox cycles

ratio = 1:1). First, in situ XRD was employed to study the structural changes of Pt–Ni/CB catalysts under alternating redox treatments (Fig. 4.9a). After HTO treatments, XRD pattern shows a main peak at 39.9° which is from the (111) plane of Pt [46]. However, the HTR treatments induce the shift of 2θ diffraction peak to 40.6° indicating the formation of Pt–Ni alloy phase [47]. We further utilize in situ XAFS to characterize the chemical states of Ni in Pt–Ni/CB catalysts under same alternating redox treatments (Fig. 4.9b). After HTO treatment a strong white line at 8351 eV is observed in the Ni–K-edge structure, which is well consistent with the spectrum from NiO sample. Previous studies have shown the Ni–O interaction could increase the intensity of Ni–K-edge white line [20]. In a HTR-treated sample the white line intensity decreases due to the reduction of NiO. Both in situ XRD and XAFS studies demonstrate that the HTO treatment induces outward diffusion of Ni to form Pt@NiO core–shell nanoparticles while the HTR results in inward diffusion of Ni producing a Pt-rich surface with Pt–Ni alloy phase inside.
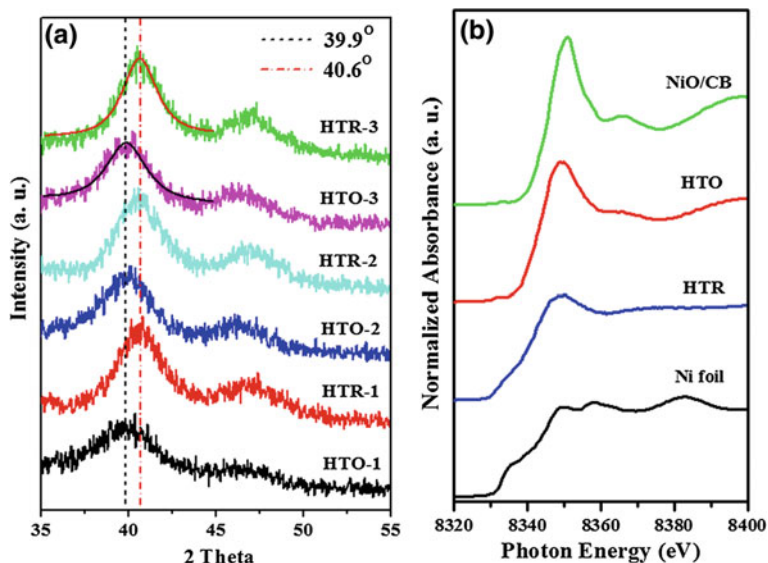
Fig. 4.9 a In situ XRD patterns and **b** in situ Ni–K-edge XANES spectra acquired from the supported Pt–Ni catalysts treated in alternating oxidizing (100% O2, 0.1 MPa) and reducing (20% H2, 0.1 MPa) atmospheres at 573 K. Reprinted with permission from Ref. [28]. Copyright (2011) American Chemical Society

Similar to the CO adsorption experiment over model catalytic surfaces, the surface composition of Pt–Ni nanoparticles was detected by combination of CO adsorption and in situ Raman characterization. As shown in Fig. 4.10, no obvious peak is observed on HTO-treated sample due to the encapsulation of NiO

Fig. 4.10 Raman spectrum of CO-saturated Pt–Ni nanoparticles pretreated by VT redox conditions
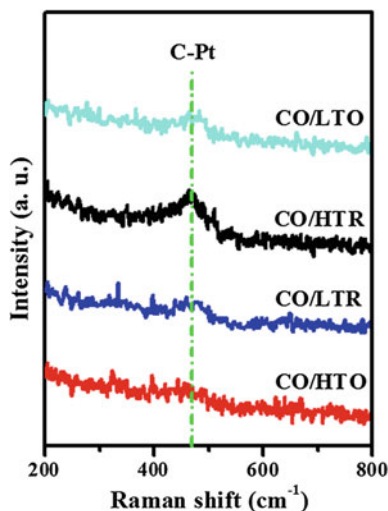
overlayers on Pt surface. In contrast, a strong peak from Pt–C bond (~480 cm^{-1}) appears on HTR-treated sample, indicating the formation of Pt-rich surface. Furthermore, we also observe clear Pt–C peaks on LTR- and LTO-treated samples. Therefore, we suggest a metastable structure with both Pt and Ni(O) on surface is achieved through LTR of Pt@NiO and LTO of Pt-rich surface.

The surface distribution of Pt–Ni bicomponent nanoparticles was further investigated by acid leaching combined with inductively coupled plasma atomic emission spectrometry (ICP-AES) measurement (Table 4.1). In acid leaching process, the 3d transition metals on Pt surface can be dissolved in acid solution, whereas those inside nanoparticles are stable due to the protection of Pt surface [12, 15, 48, 49]. Our data show that most of Ni on oxidized Pt–Ni nanoparticles can be leached away (18.1/22.1) (Table 4.1). In contrast, only a small part of Ni is removed from the reduced catalysts. As reduction temperature increases, less Ni can be dissolved in acid solution. These ICP results well support the above-proposed Pt@NiO and Pt-rich surface configurations prepared after HTO and HTR, respectively. For LTO and LTR treatments, the surface mass transfer becomes kinetically limited, as thus part of the Ni remains on the surface along with other Ni inside. These results are well consistent with our finding on the model Ni–Pt(111) catalytic system.

The CO oxidation reactivity of Pt–Ni/CB catalysts after VT redox treatments was tested at 348 K (1% CO, 20% O_2 with He balance). First, Pt–Ni/CB catalyst was treated by HTO and HTR treatments. The CO oxidation reaction was carried out in between HTO and HTR. We find that the CO conversion of HTO-treated sample is about 10%, whereas the CO conversion of HTR-treated catalyst is $\sim50\%$ (Fig. 4.11). Moreover, CO conversion shows a nicely reversible up-down dependence on two HTR and HTO cycles. Our studies from model catalytic systems and supported nanoparticles demonstrate the HTR treatment produces a Pt-rich surface with subsurface Ni. Nevertheless, the Pt-rich surface shows a moderate CO oxidation reactivity at low temperature because the activation of O_2 is still limited. After the HTO treatments, the encapsulation of NiO overlayers on Pt surface depresses the reactivity largely.

As shown in Fig. 4.11, CO conversion of the LTR-treated Pt–Ni/CB catalyst reaches above 90%. Interestingly, a large oscillation of the CO conversion is observed ranging from below 10% to above 90% after the alternating HTO and LTR treatments. Furthermore, the catalyst treated by LTO presents a CO conversion as high as >99% (Fig. 4.11). Again a nicely up-down oscillation of the CO conversion is observed after LTO, HTO, and HTR treatments.

Table 4.1 The concentrations of Ni and Pt in the leached solutions from the Pt–Ni/CB catalysts after redox treatments

Concentration (μg/mL)	AP[a]	LTR	HTR	LTO	HTO
Ni	22.2	9.2	6.1	16.0	18.1
Pt	58.5	0.1	0.0	0.0	0.1

[a]The as-prepared (AP) Pt–Ni/CB catalyst without reduction was dissolved in the acid solution as a reference

Fig. 4.11 The reactivity of Pt–Ni/CB catalysts for CO oxidation at 348 K after various redox treatments. Reprinted with permission from Ref. [28]. Copyright (2011) American Chemical Society
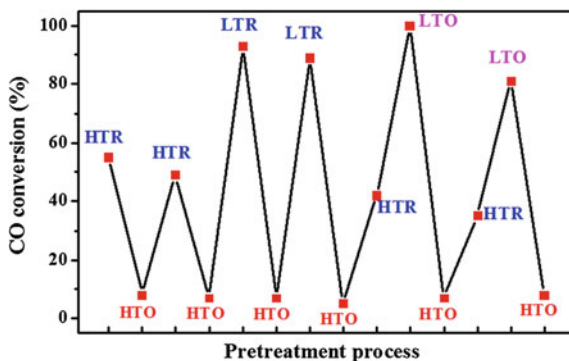
Results from model Ni–Pt(111) catalytic systems combined with supported Pt–Ni/CB catalysts show low-temperature reduction of Pt@NiO sample induces part of Ni to diffuse into subsurface region, and thus produces discontinuous Ni on surface (Ni-on-Pt). On the other hand, low-temperature oxidation of Pt-skin surface induces the surface segregation of part subsurface Ni and form highly dispersed NiO-on-Pt surface (NiO-on-Pt). Therefore, a unique sandwich-like surface configuration consisting of surface Ni(O), surface Pt, and subsurface Ni species can be achieved after LTR and LTO treatments. The formed "NiO-on-Pt" structure with subsurface Ni catalyzes the CO oxidation more efficiently through the bifunctional role of surface Pt and Ni sites and the synergetic effect of subsurface Ni. More importantly, our results show the reversible switch between these three surface structures can be simply established by redox treatments at different temperatures (Fig. 4.12). The CO oxidation reactivity, which is direct dependent on the surface structures of Pt–Ni bicomponent catalysts, presents the similar reversible changes after redox treatments.

Fig. 4.12 Treatment–structure–reactivity correlation of the Pt–Ni catalysts. Reversible transformation between Pt@NiO core–shell structure, Ni(O)-on-Pt structure, and Pt-rich structure can be observed after the VT redox treatments. Pt: *cyan ball*; metallic Ni: *red ball*; oxidized Ni: *yellow ball*. Reprinted with permission from Ref. [28]. Copyright (2011) American Chemical Society
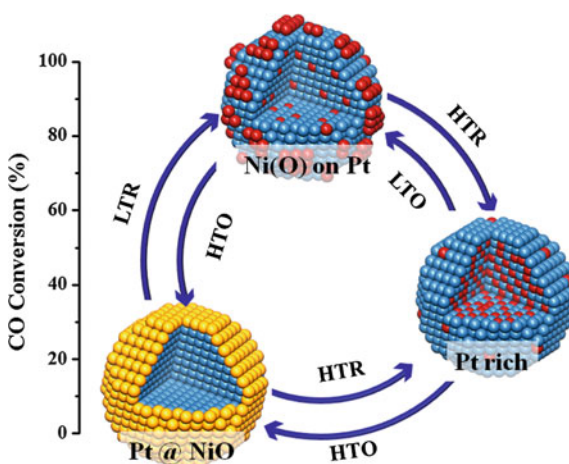
Fig. 4.13 The dependence of the XPS Co2p/Pt4f ratio on Pt–Co/HOPG sample after alternating oxidation (100% O2, 0.1 MPa) and reduction (20% H2, 0.1 MPa) cycles at 573 K. Reprinted from Ref. [44], Copyright (2009), with permission from Elsevier
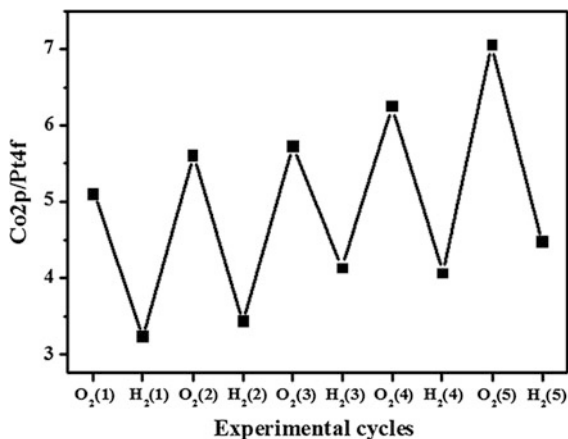
In addition, we also investigate the effect of redox treatment on surface structures of Pt–Fe, Pt–Co, and Pt–Cu bicomponent nanoparticles supported on HOPG surface. Figure 4.13 shows the reversible up-down oscillation of XPS Co2p/Pt4f ratio after alternating HTO and HTR treatments. This indicates the encapsulation of CoO overlayers on Pt surface and the formation of Pt-rich surface after HTO and HTR, respectively. At last, we find Pt–Fe and Pt–Cu bicomponent nanoparticles present similar reversible changes of surface structure under alternating redox treatments.

4.4 Summary

Reduction and oxidation are frequently applied for the preparation of practical catalysts, such as sintering in air and activation in reductive condition. But the nature of the influences of redox treatment on the performance of catalysts is often ignored. In this chapter we have shown how sensitively the surface structure and catalytic reactivity of Pt–Ni bicomponent catalysts depends on the treatment conditions. The best reactivity for the CO oxidation was observed on a catalyst treated through low-temperature reduction or low-temperature oxidation because of the formation of highly active Ni(O)-on-Pt surface structure. In contrast, high-temperature oxidation and high-temperature reduction produce NiO@Pt and Pt-rich surfaces, presenting the deactivation and moderate reactivity, respectively. The displayed treatment–structure–performance relationship for Pt–Ni bicomponent catalysts illustrates the science of preparation. Pt–Fe, Pt–Co, and Pt–Cu bicomponent nanoparticles present similar modulation of surface structures under alternating redox treatment processes, i.e., HTO produces encapsulated layers of 3d transition metal oxide on Pt surface, whereas HTR induces surface segregation of Pt.

References

1. Ahmadi TS et al (1996) Shape-controlled synthesis of colloidal platinum nanoparticles. Science 272(5270):1924–1926
2. Haruta M (1997) Size- and support-dependency in the catalysis of gold. Catal Today 36 (1):153–166
3. Roduner E (2006) Size matters: why nanomaterials are different. Chem Soc Rev 35(7):583–592
4. Yang PD et al (2006) Morphological control of catalytically active platinum nanocrystals. Angew Chem Int Edit 45(46):7824–7828
5. Xia Y et al (2009) Shape-controlled synthesis of metal nanocrystals: simple chemistry meets complex physics? Angew Chem Int Ed 48(1):60–103
6. Somorjai GA, Li YM (2010) Nanoscale advances in catalysis and energy applications. Nano Lett 10(7):2289–2295
7. Somorjai GA, Li YM (2011) Impact of surface chemistry. Proc Natl Acad Sci 108(3):917–924
8. Yang H (2011) Platinum-based electrocatalysts with core-shell nanostructures. Angewandte Chem Int Ed 50(12):2674–2676
9. Zhou SH et al (2005) Pt-Cu core-shell and alloy nanoparticles for heterogeneous NOx, reduction: anomalous stability and reactivity of a core-shell nanostructure. Angewandte Chem Int Ed 44(29):4539–4543
10. Christensen CH, Norskov JK (2008) A molecular view of heterogeneous catalysis. J Chem Phys 128(18):182503
11. Besenbacher F et al (1998) Design of a surface alloy catalyst for steam reforming. Science 279(5358):1913–1915
12. Strasser P et al (2010) Lattice-strain control of the activity in dealloyed core-shell fuel cell catalysts. Nat Chem 2(6):454–460
13. Chen S et al (2009) Origin of Oxygen reduction reaction activity on "Pt_3Co" nanoparticles: atomically resolved chemical compositions and structures. J Phys Chem C 113(3):1109–1125
14. Mayrhofer KJJ et al (2009) Adsorbate-induced surface segregation for core-shell nanocatalysts. Angew Chem Int Ed 48(19):3529–3531
15. Mayrhofer KJJ et al (2009) Degradation of carbon-supported pt bimetallic nanoparticles by surface segregation. J Am Chem Soc 131(45):16348–16349
16. Hellman A, Klacar S, Gronbeck H (2009) Low temperature CO oxidation over supported ultrathin MgO films. J Am Chem Soc 131(46):16636–16637
17. Tao F et al (2008) Reaction-driven restructuring of Rh-Pd and Pt-Pd core-shell nanoparticles. Science 322(5903):932–934
18. Tao F et al (2010) Evolution of structure and chemistry of bimetallic nanoparticle catalysts under reaction conditions. J Am Chem Soc 132(25):8697–8703
19. Zheng F et al (2011) In-situ X-ray absorption study of evolution of oxidation states and structure of cobalt in Co and CoPt bimetallic nanoparticles (4 nm) under reducing (H_2) and oxidizing (O_2) environments. Nano Lett 11(2):847–853
20. Menning CA, Chen JG (2010) Regenerating Pt-3d-Pt model electrocatalysts through oxidation-reduction cycles monitored at atmospheric pressure. J Power Sources 195 (10):3140–3144
21. Surnev S et al (2002) Reversible Dynamic behavior in catalyst systems: oscillations of structure and morphology. Phys Rev Lett 89(24):246101
22. Kitchin JR, Reuter K, Scheffler M (2008) Alloy surface segregation in reactive environments: first-principles atomistic thermodynamics study of $Ag_3Pd(111)$ in oxygen atmospheres. Phys Rev B 77(7):075437
23. Tenney SA et al (2011) CO-induced diffusion of Ni atoms to the surface of Ni-Au clusters on $TiO_2(110)$. J Phys Chem C 115(22):11112–11123

24. Mu RT et al (2009) Reversible surface structural changes in Pt-based bimetallic nanoparticles during oxidation and reduction cycles. Appl Surf Sci 255(16):7296–7301
25. Knudsen J et al (2007) A Cu/Pt near-surface alloy for water-gas shift catalysis. J Am Chem Soc 129(20):6485–6490
26. Kitchin JR et al (2003) Elucidation of the active surface and origin of the weak metal-hydrogen bond on Ni/Pt(111) bimetallic surfaces: a surface science and density functional theory study. Surf Sci 544(2–3):295–308
27. Stamenkovic VR et al (2007) Trends in electrocatalysis on extended and nanoscale Pt-Bimetallic alloy surfaces. Nat Mater 6(3):241–247
28. Mu R et al (2011) Oscillation of surface structure and reactivity of PtNi bimetallic catalysts with redox treatments at variable temperatures. J Phys Chem C 115(42):20590–20595
29. Hagendorf C et al (2006) Pressure-dependent Ni-O phase transitions and Ni oxide formation on Pt(111): an in situ STM study at elevated temperatures. Phys Chem Chem Phys 8 (13):1575–1583
30. Bouwman R, Sachtler WM, Lippits GJM (1972) Photoelectric investigation of surface composition of equilibrated Ag-Pd alloys in ultrahigh-vacuum and in presence of Co. J Catal 25(3):350
31. Bouwman R, Sachtler WM (1972) Photoelectric investigation of surface composition of equilibrated Pt-Ru alloy films in ultrahigh-vacuum and in presence of Co. J Catal 26(1):63
32. Bouwman R et al (1976) Surface enrichment in Ag-Au alloys. Surf Sci 59(1):72–82
33. McLean D (ed) (1957) Grain boundaries in metals. Clarendon Press, Oxford
34. Su HY, Bao XH, Li WX (2008) Modulating the reactivity of Ni-containing Pt(111)-skin catalysts by density functional theory calculations. J Chem Phys 128(19):194707
35. Chen JG, Menning CA, Zellner MB (2008) Monolayer bimetallic surfaces: experimental and theoretical studies of trends in electronic and chemical properties. Surf Sci Rep 63(5):201–254
36. Kinne M et al (2004) Coadsorption of D_2O and CO on Pt(111) studied by in situ high-resolution X-ray photoelectron spectroscopy. Langmuir 20(5):1819–1826
37. Kitchin JR et al (2004) Modification of the surface electronic and chemical properties of Pt (111) by subsurface 3d transition metals. J Chem Phys 120(21):10240–10246
38. Stamenkovic V et al (2006) Changing the activity of electrocatalysts for oxygen reduction by tuning the surface electronic structure. Angew Chem Int Ed 45(18):2897–2901
39. Kitchin JR et al (2004) Role of strain and ligand effects in the modification of the electronic and chemical Properties of bimetallic surfaces. Phys Rev Lett 93(15):156801
40. Alayoglu S, Eichhorn B (2008) Rh-Pt bimetallic catalysts: synthesis, characterization, and catalysis of core-shell, alloy, and monometallic nanoparticles. J Am Chem Soc 130 (51):17479–17486
41. Alayoglu S et al (2008) Ru-Pt core-shell nanoparticles for preferential oxidation of carbon monoxide in hydrogen. Nat Mater 7(4):333–338
42. Nilekar AU, Mavrikakis M (2008) Improved oxygen reduction reactivity of platinum monolayers on transition metal surfaces. Surf Sci 602(14):L89–L94
43. Ma T et al (2009) Reversible structural modulation of Fe-Pt bimetallic surfaces and its effect on reactivity. Chem Phys Chem 10(7):1013–1016
44. Mu R et al (2009) Reversible surface structural changes in Pt-based bimetallic nanoparticles during oxidation and reduction cycles. Appl Surf Sci 255(16):7296–7301
45. Wang GF et al (2005) Monte carlo simulations of segregation in Pt-Ni catalyst nanoparticles. J Chem Phys 122(2):02470
46. Deivaraj TC, Chen WX, Lee JY (2003) Preparation of PtNi nanoparticles for the electrocatalytic oxidation of methanol. J Mater Chem 13(10):2555–2560
47. Leonard BM et al (2011) Facile synthesis of PtNi intermetallic nanoparticles: influence of reducing agent and precursors on electrocatalytic activity. Chem Mater 23(5):1136–1146
48. Strasser P (2009) Dealloyed core-shell fuel cell electrocatalysts. Rev Chem Eng 25(4):255–295
49. Mani P, Srivastava R, Strasser P (2008) Dealloyed Pt-Cu core-shell nanoparticle electrocatalysts for use in PEM fuel cell cathodes. J Phys Chem C 112(7):2770–2778

Chapter 5
Comparison of Pt–Fe and Pt–Ni Catalysts

In this chapter, we compare the reactivity and stability of Pt–Fe and Pt–Ni bicomponent catalysts. The interfacial confinement effect results in the formation of monolayer-thick FeO_{1-X} and NiO_{1-X} nanoislands on Pt(111). The edge structures of the FeO_{1-X} and NiO_{1-X} nanoislands provide the active sites for O_2 dissociative adsorption, and thus promote CO oxidation reaction. But the stabilities of FeO_{1-X}/Pt(111) and NiO_{1-X}/Pt(111) systems are different after the oxidation at 473 K with a O_2 partial pressure of 1.3×10^{-6} mbar. FeO_{1-X} nanoisland is oxidized to O–Fe–O trilayer structure after oxidation, while the chemical state of NiO_{1-X} is unchanged after same oxidative treatment. The result of model catalytic systems is well consistent with the observation of supported Pt–Fe/CB and Pt–Ni/CB catalysts. In situ XANES investigations show the chemical state of Fe is 2+ under CO oxidation with excess H_2, whereas the Fe is further oxidized in O_2-rich atmosphere. In contrast, the chemical state of Ni is constant under H_2-rich and O_2-rich CO oxidation conditions. Therefore, the CO conversion over Pt–Ni/CB catalyst increases when the concentration of O_2 is increasing.

5.1 Introduction

Transition metal oxides (TMOs) are widely used as the support to prepare the highly dispersed catalysts, because they often present unique redox properties themselves and thus promote the performance of noble metal catalysts [1–3]. For example titania, ceria and iron oxide are used as the support to prepare Au, Pd, and Pt nanoparticle catalysts [4–7].

On the other hand, the so-called *inverse model catalysts* are also constructed by depositing oxide on the surface of noble metals (O/M) [1–3, 8–12]. Over O/M inverse catalysts, two main reaction mechanisms are often proposed. One case is that the intact oxide films on noble metal surface act as the active structure for catalytic reaction. For example, monolayer FeO_X film supported on Pt(111) surface

performed better reactivity of CO oxidation than bare Pt(111) surface [8]. STM investigations have shown that the intact FeO_X film was transformed to highly dispersed nanoparticles on Pt(111) surface and thus part of Pt surface was exposed. Subsequently, the catalytic CO oxidation was carried out through the Langmuir–Hinshelwood mechanism [8, 13]. Similarly, the Pt–Fe bicomponent catalysts supported on SiO_2 also showed high reactivity and selectivity for preferential CO oxidation in excess H_2 [14]. Another case is the O/M perimeters act as active site. For example, $TiO_{2-X}/Au(111)$ and $CeO_{2-X}/Au(111)$ inverse catalysts showed superior reactivity of water–gas shift reaction where water was found to dissociate at O-vacancies of oxide islands and CO was adsorbed on bare Au(111) surface. Then the reaction occurred at oxide-Au(111) perimeters [11]. On the basis of surface science approaches and density functional calculations, Bao's group has shown the interface-confined coordinatively unsaturated ferrous (CUF) sites were the active centers to activate O_2 molecule and thus catalyzed CO oxidation [10, 15].

Though the structure and reactivity of *inverse model catalysts* have been studied extensively, the investigations of their stabilities are still lack. In this chapter, we compare the (un)flexibility of chemical states and reactivity of interface-confined FeO_{1-X} and NiO_{1-X} under the reductive and oxidative conditions, which are the most frequently countered reaction atmospheres.

5.2 FeO_X/Pt(111) Model Catalytic Systems

In order to obtain highly dispersed oxide islands on the Pt(111) surface, the preparation of 0.38 ML FeO_{1-X}/Pt(111) model surface was divided into two steps [15]. First, Fe was deposited in 1.3×10^{-6} mbar O_2 at 165 K. Second, FeO_{1-X}/Pt (111) surface was annealed to 573 K in UHV for 3 min. XPS studies show the binding energy of Fe2p3/2 on this as-prepared FeO_{1-X}/Pt(111) surface locates at 709.3 eV (Fig. 5.1a-*a*), indicating the chemical state of Fe is 2+ [17]. STM study illustrates the FeO_{1-X} nanoislands are monolayer (Fig. 5.1b).

The oxidation of FeO_{1-X}/Pt(111) was carried out in 5.2×10^{-6} mbar O_2 at 473 K for 5 min. After the oxidation, the Fe^{2+} species are further oxidized to FeO_{1+X} with the binding energy of Fe2p3/2 shifting to 709.9 eV (Fig. 5.1a-*b*). Earlier works have found the intact FeO film on Pt(111) surface was oxidized to O–Fe–O trilayer structure under near ambient O_2 pressure [18, 19]. For 0.38 ML FeO_{1-X}/Pt(111) surface, the size of FeO_{1-X} nanoislands is about $5 \sim 10$ nm (Fig. 5.1b). So we expect that the FeO_{1-X} nanoislands should be easier to be oxidized, when compared with intact FeO thin films. Furthermore, STM image in Fig. 5.1c exhibits a new $(\sqrt{3} \times \sqrt{3})$ R30° structure with respect to FeO, indicating the formation of O–Fe–O trilayer structure [18, 19].

The reactivity of the as-prepared and oxidized FeO_{1-X}/Pt(111) model catalytic systems was characterized by in situ UPS He II studies. All the surfaces were pre-adsorbed with 10 L CO at RT. The peaks locating at 9.4 and 11.8 eV originated from $5\sigma + 1\pi$ to 4σ molecular orbits of CO adsorbed on Pt(111) surface were
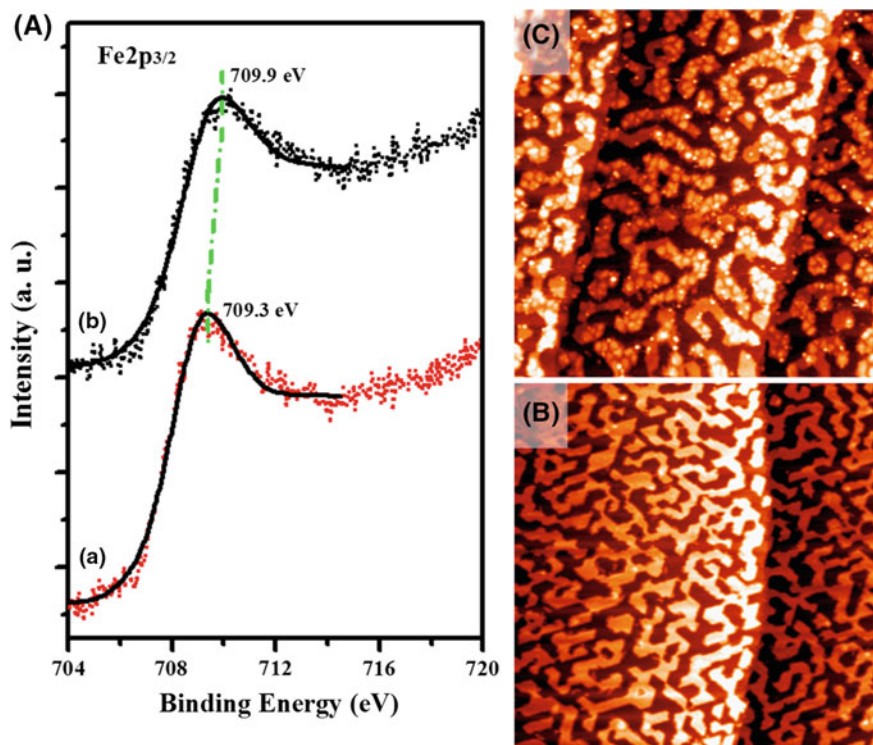
Fig. 5.1 a XPS Fe2p3/2 of (*a*) as-prepared 0.38 ML FeO$_{1-X}$/Pt(111) and (*b*) the oxidized 0.38 ML FeO$_{1+X}$/Pt(111) in 1.3×10^{-6} mbar O$_2$ at 473 K for 5 min. From Ref. [16]. With permission of Springer. **b** STM images of the as-prepared 0.38 ML FeO$_{1-X}$/Pt(111). **c** STM image of the oxidized 0.38 ML FeO$_{1+X}$/Pt(111) surface. (b, c): 200 nm × 200 nm

recorded [20–22], which stands for the relative amount of CO adsorbed on Pt(111) surface. To test the reactivity, the CO-adsorbed surfaces were exposed in 4.0×10^{-8} mbar O$_2$ at RT, and UPS spectrums were recorded simultaneously with one line per minute. The gradual decrease of peak intensity of adsorbed CO along with reaction time was monitored to characterize the reactivity.

Over the as-prepared FeO$_{1-X}$/Pt(111) model surface, CO can be removed completely in 10 min in 4.0×10^{-8} mbar O$_2$. Fu and Li et al. have established that the interface-confined CUF sites at the perimeters of FeO$_{1-X}$ nanoislands provided active sites for O$_2$ dissociative adsorption, and thus promoted the CO + O→CO$_2$ reaction [10]. After the first removal of CO on the Pt(111) surface, two more reaction cycles are carried out continuously and no decrease of CO oxidation reactivity of the as-prepared FeO$_{1-X}$/Pt(111) is observed (Fig. 5.2a). In contrast, the reactivity of oxidized FeO$_{1+X}$/Pt(111) surface was also studied. Over the oxidized FeO$_{1+X}$/Pt(111) model surface, a worse CO oxidation reactivity is observed. CO on the oxidized surface can be eliminated in 18 min in 4.0×10^{-8} mbar O$_2$ for the first reaction cycle, 30 min for the second reaction cycle (Fig. 5.2b). The dramatic

Fig. 5.2 The CO oxidation
reactivity of (**a**) the
as-prepared 0.38 ML FeO_{1-X}/
Pt(111) and (**b**) the oxidized
FeO_{1+X}/Pt(111). From Ref.
[16]. With permission of
Springer
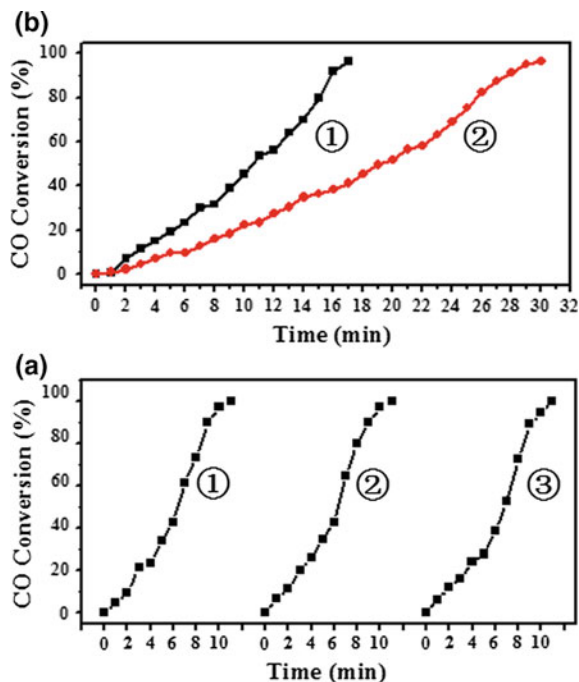
decrease of CO oxidation reactivity on oxidized FeO_{1+X}/Pt(111) should be attributed to the transformation of interface-confined Fe^{2+} cations to high chemical state, i.e., Fe^{2+X}.

5.3 NiO_X/Pt(111) Model Catalytic Systems

The highly dispersed NiO_{1-X} nanoislands can be obtained at the preparation temperature up to 300 K. The preparation of 0.38 ML NiO_{1-X}/Pt(111) was carried out in 1.3×10^{-6} mbar O_2 at room temperature, then annealed in UHV at 523 K for 3 min. XPS Ni2p3/2 peak recorded from the as-prepared NiO_{1-X}/Pt(111) surface locates at 853.6 eV, according with Ni^{2+} state (Fig. 5.3a-*a*) [23, 24]. STM results show the NiO_{1-X} nanoislands present monolayer height on Pt(111) surface.

Different from FeO_X/Pt(111) model systems, XPS result shows that the chemical state of NiO_X on Pt(111) does not change after the oxidation treatment in 5.2×10^{-6} mbar O_2 at 473 K for 5 min (Fig. 5.3a-*b*). Furthermore, the dispersion and structure of NiO_{1-X} nanoislands are unchanged as well (Fig. 5.3c).

Similar to the FeO_{1-X}/Pt(111) systems, we suggest that the interface-confined Ni^{2+} cations at the perimeters of NiO_{1-X} nanoislands provide active sites for O_2 dissociative adsorption and enhance catalytic CO oxidation reaction. Furthermore, since the dispersion of NiO_{1-X} nanoislands is higher than the dispersion of FeO_{1-X}
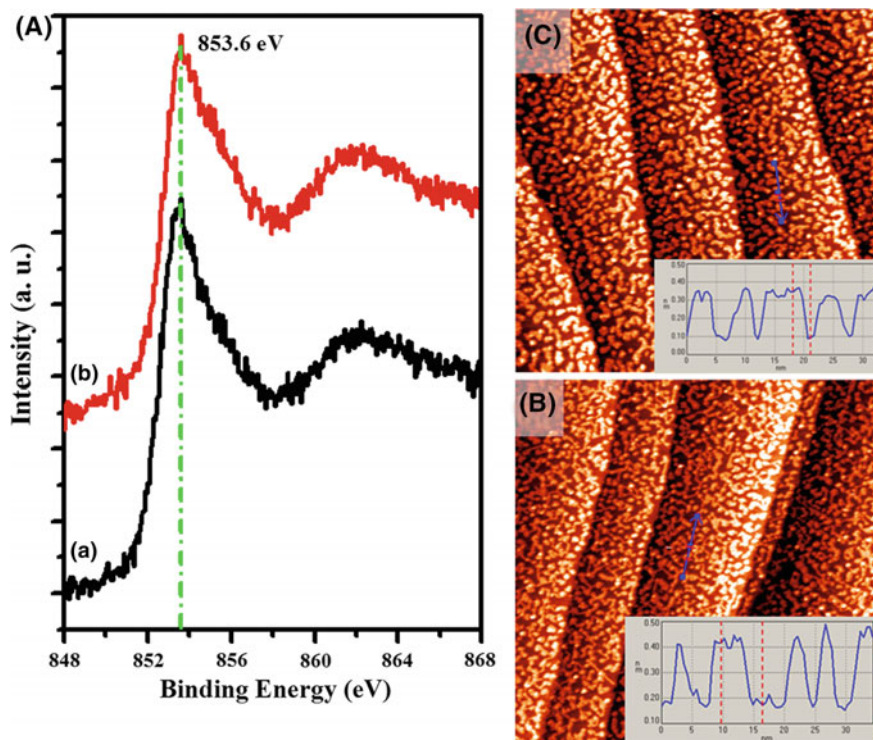
Fig. 5.3 a XPS Ni2p3/2 of (*a*) as-prepared 0.38 ML NiO$_{1-X}$/Pt(111) prepared at room temperature and (*b*) the oxidized 0.38 ML NiO$_{1-X}$/Pt(111) in 1.3×10^{-6} mbar O$_2$ at 473 K for 5 min. From Ref. [16]. With permission of Springer. **b** STM images of the as-prepared 0.38 ML NiO$_{1-X}$/Pt(111) prepared at room temperature. **c** STM image of the oxidized 0.38 ML NiO$_{1-X}$/Pt (111). (b, c): 200 nm × 200 nm

nanoislands, we find the as-prepared NiO$_{1-X}$/Pt(111) surface performs better reactivity than the as-prepared FeO$_{1-X}$/Pt(111) surface. As shown in Fig. 5.4a, CO on the as-prepared NiO$_{1-X}$/Pt(111) surface can be removed in 3 min in 4.0×10^{-8} mbar O$_2$ for three reaction cycles at room temperature. To study the reactivity of the oxidized surface, NiO$_{1-X}$/Pt(111) was oxidized in 5.2×10^{-6} mbar O$_2$ at 473 K for 5 min. In spite of the oxidation treatment, the oxidized NiO$_{1-X}$/Pt(111) surface still shows similar CO oxidation reactivity (Fig. 5.4b). As revealed in XPS studies, the chemical state of NiO$_{1-X}$ keeps at +2 before and after oxidation.

In surface science studies, the stability of interface-confined Fe^{2+} and Ni^{2+} cations under oxidation conditions was revealed. Over FeO$_{1-X}$/Pt(111) model system, the as-prepared FeO$_{1-X}$ nanoislands are further oxidized to FeO$_{1+X}$ in oxidative atmosphere which induces the CO oxidation reactivity to decrease [10]. In contrast, NiO$_{1-X}$/Pt(111) surface is stable after identical oxidation treatment. Therefore, the NiO$_X$–Pt catalyst may be a good candidate for catalytic CO oxidation reaction in oxidative atmospheres.

Fig. 5.4 The CO oxidation reactivity of (**a**) the as-prepared 0.38 ML NiO_{1-X}/Pt(111) and (**b**) the oxidized NiO_{1-X}/Pt(111). From Ref. [16]. With permission of Springer
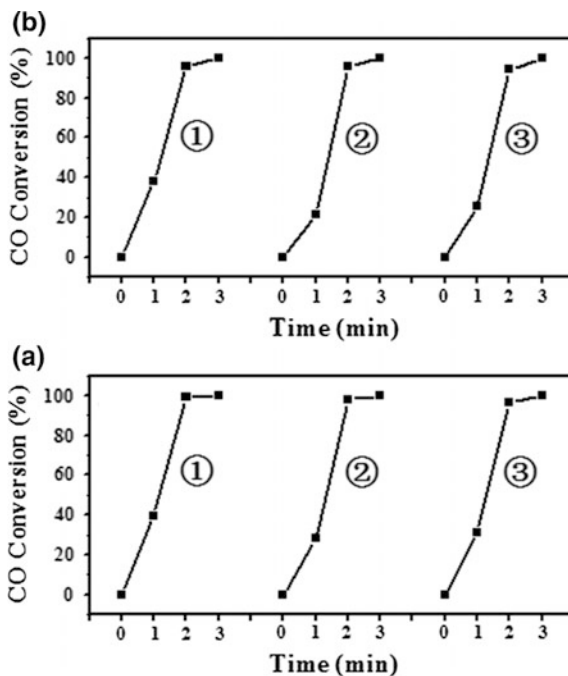

5.4 Pt–Fe/CB and Pt–Ni/CB Nanoparticle Catalysts

We prepare Pt–Fe and Pt–Ni nanoparticles supported on carbon black using co-impregnation method. The loading of Pt and Fe (Ni) was controlled at 4 and 0.3 wt%, respectively (molar ratio = 4:1).

Based on the surface science studies, we expect that the Pt–Fe and Pt–Ni bicomponent catalysts may show high CO oxidation reactivity with excess hydrogen and oxygen, respectively. Herein, we use common reductive and oxidative reaction gases, i.e., preferential CO oxidation with excess hydrogen (PROX, 1% CO, 0.5% O_2, 50% H_2, and 48.5% He) and CO oxidation with excess oxygen (COOX, 1% CO, 20% O_2, and 79% He) to test the performance of Pt–Fe/CB and Pt–Ni/CB catalysts.

Before the CO oxidation reaction, fresh Pt–Fe/CB and Pt–Ni/CB catalysts were reduced in H_2 at 473 K for 2 h. The components of Pt, Fe, and Ni can be reduced to metallic state completely. The conversion of CO was determined by online chromatograph. The weight hourly space velocity (WHSV) was set at 30000 mL·h^{-1}·g^{-1}. As shown in Fig. 5.5, CO conversion keeps above 90% on the Pt–Fe/CB catalyst in PROX reaction condition at 353 K, while the CO conversion only reaches about 40% on Pt–Ni/CB catalyst in identical reaction condition. In COOX reaction condition, the CO conversion of Pt–Fe/CB catalyst decreases to

Fig. 5.5 The performance of
Pt–Fe/CB and Pt–Ni/CB
catalysts in alternating CO
oxidation (1% CO, 20% O_2,
He balance) and CO oxidation
with excess hydrogen (1%
CO, 0.5% O_2, 50% H_2 and
48.5% He) at 353 K. From
Ref. [16]. With permission of
Springer
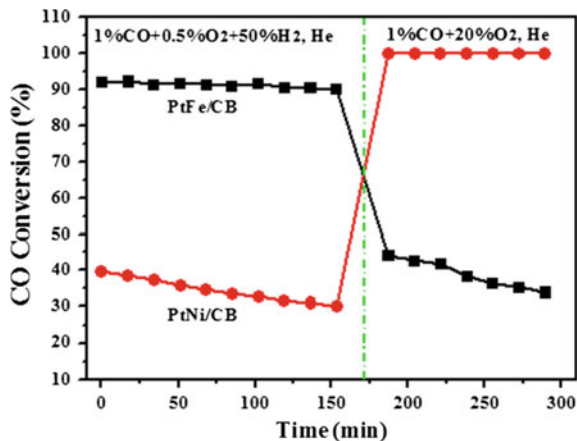
below 50%. Surprisingly, the CO conversion reaches >99% on Pt–Ni/CB catalyst
when the reaction gas switched to oxygen rich atmosphere.

In situ XAFS measurements were applied to characterize the chemical states of
Fe and Ni under various reaction conditions [25–28]. Fe–K-edge XANES spec-
trums show clear difference between reduced Pt–Fe/CB sample and Pt–Fe/CB
catalysts under alternating PROX and COOX reaction conditions. After the
reduction at 473 K for 2 h, Fe was reduced to metallic state with the peak position
of white line locating at 7125.6 eV (Fig. 5.6a). XPS studies also proved that Fe
could be reduced to metallic state at 473 K. After the exposure in PROX condition
for 1 h, the peak position of white line shifts with ~ 5 eV to higher energy, indi-
cating the oxidation of metallic Fe to FeO_X. Under COOX condition, the peak
position of Fe–K-edge white line shifts to higher energy further and resembles that
of Fe_2O_3 spectrum. Therefore, the deactivated performance of Pt–Fe/CB catalyst
under CO oxidation with excess oxygen can be attributed to the transformation of
active FeO_{1-X} to Fe_2O_3. In contrast, Ni–K-edge XANES studies in Fig. 5.6b
demonstrate NiO_X is stable in various reaction conditions. Under the CO oxidation
condition with excess oxygen, the peak position the Ni–K-edge white line locates at
8350.4 eV, which is almost the same as that of Pt–Ni/CB catalysts in PROX
condition.

Based on the surface science results, we show that the FeO_{1-X} and NiO_{1-X}
nanoislands can be obtained by depositing metal in O_2 atmosphere. The coordi-
natively unsaturated cations (Fe^{2+} and Ni^{2+}) at the perimeters of oxide nanoislands
provide active sites for O_2 dissociative adsorption and thus promote CO oxidation
on model catalytic systems. After the oxidation of 1.3×10^{-6} mbar O_2 at 473 K,
FeO_{1-X} is further oxidized to O–Fe–O trilayer structure while NiO_{1-X} is relative
stable (Fig. 5.7).
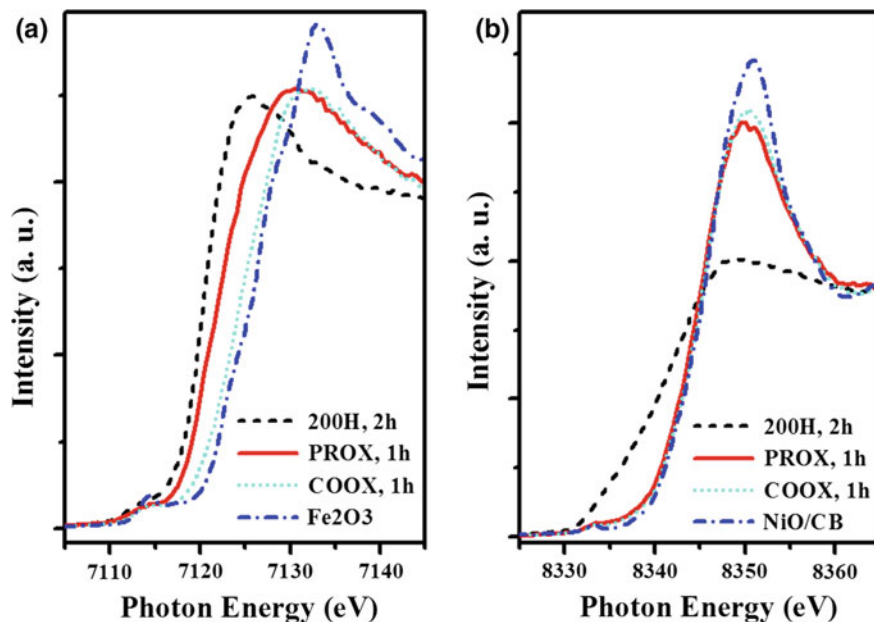
Fig. 5.6 In situ XANES studies of (**a**) Pt–Fe/CB and (**b**) Pt–Ni/CB catalysts in different reaction conditions. The spectra of Fe_2O_3 and NiO were included as reference. From Ref. [16]. With permission of Springer
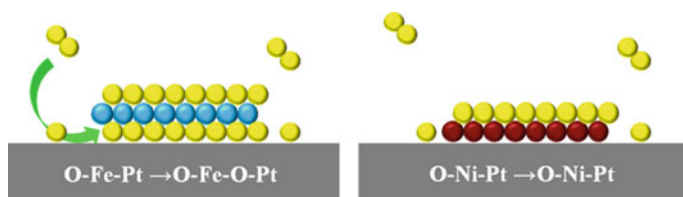
Fig. 5.7 Schematics of the structural changes of Pt–Fe and Pt–Ni bicomponent catalysts in oxidative atmosphere

We suppose that the stability difference of FeO_{1-X}/Pt(111) and NiO_{1-X}/Pt(111) interfaces may derive from the electronegativity difference of Fe^{2+} and Ni^{2+}. The electronegativities of Fe^{2+} and Ni^{2+} are 1.83 and 1.93, respectively, while the electronegativity of Fe^{3+} is 1.96 [29]. For supported nanoparticle catalysts, the Pt–Fe/CB catalyst shows superior CO oxidation reactivity with excess hydrogen. However, under CO oxidation reaction with excess oxygen, Fe^{2+} can be further oxidized to Fe^{2+X}. The chemical transformation of FeO_X induces the deactivation of Pt–Fe catalysts in oxidative atmosphere. Over Pt–Ni/CB catalyst, the chemical state

of Ni^{2+} is stable in the alternating CO oxidation reactions with excess hydrogen and oxygen. As expected, the Pt–Ni/CB converts more CO to CO_2 with higher O_2 concentration.

5.5 Summary

In this chapter, we compare the structure and reactivity of Pt–Fe and Pt–Ni bicomponent catalysts under reductive and oxidative reaction conditions from the model catalytic systems to supported nanoparticle catalysts.

(1) The interfacial confinement effect allows us to prepare FeO_{1-X} and NiO_{1-X} nanoislands on Pt(111) surface.
(2) The deposition of FeO_{1-X} and NiO_{1-X} nanoislands promotes the CO oxidation reaction of Pt(111) surface. We suggest the coordinatively unsaturated cations at the perimeters of oxide nanoislands provide the active sites for O_2 dissociative adsorption and then react with CO on Pt surface.
(3) After the oxidation treatment of 1.3×10^{-6} mbar O_2 at 473 K, the transformation of FeO_{1-X} to O–Fe–O trilayer structure induces the deactivation of FeO_X–Pt(111) model catalytic system. In contrast, NiO_{1-X} nanoislands are stable after identical oxidation treatment.
(4) Over supported nanoparticle catalysts, the opposite trends are observed on Pt–Fe/CB and Pt–Ni/CB catalysts when we switch the reaction condition from PROX to COOX. Under PROX condition, the Pt–Fe/CB catalyst presents high reactivity. But FeO is further oxidized to higher chemical state as the reaction is switched to COOX, which induces the deactivation of Pt–Fe/CB catalyst. The same reaction procedures are also conducted over Pt–Ni/CB catalyst. Different from Pt–Fe/CB catalyst, we show the chemical state of NiO_X is stable under different reaction conditions. Therefore, Pt–Ni/CB catalyst exhibits superior CO oxidation reactivity with excess oxygen.

References

1. Tauster SJ, Fung SC, Garten RL (1978) Strong metal-support interactions—Group8 noble-metals supported on TiO_2. J Am Chem Soc 100(1):170–175
2. Tauster SJ (1987) Strong metal-support interactions. Acc Chem Res 20(11):389–394
3. Fu Q, Wagner T (2007) Interaction of nanostructured metal overlayers with oxide surfaces. Surf Sci Rep 62(11):431–498
4. Hensen EJM, Ligthart DAJM, van Santen RA (2011) Supported rhodium oxide nanoparticles as highly active co oxidation catalysts. Angew Chem Int Edit 50(23):5306–5310
5. Valden M, Lai X, Goodman DW (1998) Onset of catalytic activity of gold clusters on titania with the appearance of nonmetallic properties. Science 281(5383):1647–1650

6. Kiely CJ et al (2008) Identification of active gold nanoclusters on iron oxide supports for co oxidation. Science 321(5894):1331–1335
7. Qiao BT et al (2011) Single-Atom catalysis of co oxidation using Pt_1/FeO_x. Nat Chem 3 (8):634–641
8. Sun YN et al (2008) When an encapsulating oxide layer promotes reaction on noble metals: dewetting and in situ formation of an "Inverted" FeOx/Pt catalyst. Catal Lett 126(1–2):31–35
9. Surnev S et al (2002) Reversible dynamic behavior in catalyst systems: oscillations of structure and morphology. Phys Rev Lett 89(24):246101
10. Fu Q et al (2010) Interface-confined ferrous centers for catalytic oxidation. Science 328 (5982):1141–1144
11. Rodriguez JA et al (2007) Activity of CeOx and TiOx nanoparticles grown on Au(111) in the water-gas shift reaction. Science 318(5857):1757–1760
12. Qin ZH et al (2008) Encapsulation of Pt nanoparticles as a result of strong metal-support interaction with Fe_3O_4(111). J Phys Chem C 112(27):10209–10213
13. Sun YN et al (2009) Monolayer iron oxide film on platinum promotes low temperature CO oxidation. J Catal 266(2):359–368
14. Kotobuki M et al (2005) Reaction mechanism of preferential oxidation of carbon monoxide on Pt, Fe, and Pt-Fe/mordenite catalysts. J Catal 236(2):262–269
15. Yao YX et al (2010) Growth and characterization of two-dimensional feo nanoislands supported on Pt(111). J Phys Chem C 114:17069–17079
16. Mu R et al (2015) A comparative study in structure and reactivity of "FeOx -on-Pt" and "NiOx -on-Pt" Catalysts. Sci China Chem 58(1):162–168
17. SchedelNiedrig T, Weiss W, Schlogl R (1995) Electronic structure of ultrathin ordered iron oxide films grown onto Pt(111). Phys Rev B 52(24):17449–17460
18. Sun YN et al (2010) The interplay between structure and CO oxidation catalysis on metal-supported ultrathin oxide films. Angew Chem Int Edit 49(26):4418–4421
19. Freund HJ et al (2011) CO oxidation as a prototypical reaction for heterogeneous processes. Angewandte Chem-Int Ed 50(43):10064–10094
20. Ma T et al (2009) Reversible structural modulation of Fe-Pt bimetallic surfaces and its effect on reactivity. ChemPhysChem 10(7):1013–1016
21. Tsilimis G, Kutzner J, Zacharias H (2003) Photoemission study of clean and c(4 x 2)-2CO-Covered Pt(111) using high-harmonic radiation. Appl Phys A-mater 76(5):743–749
22. Tsilimis G et al (2004) Observation of high-energy Pt(111) surface resonances excited by laser-generated XUV radiation. Appl Phys A-mater 78(2):177–181
23. Bender M, Alshamery K, Freund HJ (1994) Sodium adsorption and reaction on NiO(111)/Ni (111). Langmuir 10(9):3081–3085
24. Wruck DA, Rubin M (1993) Structure and electronic-properties of electrochromic NiO films. J Electrochem Soc 140(4):1097–1104
25. Boudart M et al (1985) Study by synchrotron radiation of the structure of a working catalyst at high-temperatures and pressures. Science 228(4700):717–719
26. George GN, Hedman B, Hodgson KO (1998) An edge with XAS. Nat Struct Biol 5:645–647
27. Nishihata Y et al (2002) Self-regeneration of a Pd-Perovskite catalyst for automotive emissions control. Nature 418(6894):164–167
28. Bell AT (2003) The impact of nanoscience on heterogeneous catalysis. Science 299 (5613):1688–1691
29. Huheey JE, Keiter EA, Keiter RL (1997) Inorganic chemistry: principles of structure and reactivity, 4th edn. Prentice Hall

Chapter 6
Reactivity of Graphene-Confined Pt(111) Surface

By employing real-time microscopic techniques, the confinement effect of single-layer graphene on the chemistry of CO/Pt(111) system is studied. We find that the CO molecules can easily intercalate between graphene and Pt(111) even under UHV condition at room temperature. Interestingly, CO desorb from the interfacial space between graphene and Pt(111) around room temperature. In contrast, the desorption temperature of CO from bare Pt(111) is ~ 420 K. DFT calculations show the adsorption energy of CO on Pt(111) is decreased by the confinement effect of graphene on top. Furthermore, the dynamic process of CO oxidation is also studied. We find that the graphene wrinkles act as the reaction channels for CO desorption and CO oxidation processes.

6.1 Introduction

The earlier studies in this Thesis were mainly focused on the understanding of correlation between surface structure and performance of Pt-3d transition metal bi-component catalysts. We demonstrated the synergetic effect of surface NiO_{1-X} and subsurface Ni metal significantly improved the reactivity of Pt catalyst for catalytic CO oxidation. In this chapter, we prepare single graphene on Pt(111) surface and further investigate the confinement effect of single-layer graphene on catalytic properties of Pt(111). Using the newly built Deep Ultraviolet Photoemission Electron Microscopy (DUV-PEEM) System combined with in situ spectroscopic characterizations, the dynamics of surface reactions, such as CO intercalation, CO desorption, and CO oxidation confined under graphene, are studied intensively.

CO oxidation on Pt single crystal surface has been studied extensively by microscopic techniques [1–3]. For example, Ertl and coworkers have used PEEM to study the CO oxidation reaction on Pt(110) surface. The observed reaction process was explained by nonlinear dynamics theory [2]. Low-Energy Electron Microscopy

(LEEM) method showed better spatially resolution, which has been widely employed in the characterization of material growth and phase transformation, etc. [4–6]. But the image contrast of PEEM and LEEM images on Pt(111) surface before and after CO adsorption does not change significantly. So we need more aid combined with PEEM and LEEM to direct study CO adsorption on Pt(111). Theoretical calculation has shown the change of graphene–substrate distance could induce the distinct contrast change of LEEM images [7]. Therefore, the adsorption and desorption of CO between graphene and Pt(111) surface should be visualized with the aid of the imaging effect of single-layer graphene, because CO intercalation and removal can increase and decrease graphene–substrate distance, respectively.

In this chapter, we use real-time microscopic characterizations combined with DFT calculations to investigate CO intercalation, desorption, and oxidation in the interfacial space between graphene and Pt(111) surface. More importantly, we find the confinement effect of graphene layer alters the chemistry of CO molecules on Pt (111) surface. Further, a small amount of CO_2 generated from CO oxidation is detected under graphene layer at elevated temperature.

6.2 Preparation of Graphene on Pt(111) Surface

On a clean Pt(111) surface, smooth steps and flat terraces can be observed in LEEM image (Fig. 6.1a). To prepare single-layer graphene (SLG) with μm size on Pt(111) surface [μSLG/Pt(111)], we employ surface segregation process. At first, Pt(111) surface was exposed to 2 Langmuir ethylene at 700–800 K. Then the carbon source was dissolved into near-surface and even bulk region of Pt substrate by annealing to 1100 K for 2 min. Surface segregation of bulk carbon was carried out to form SLG on Pt(111) surface by slowly cooling Pt substrate to 900–950 K. The size of SLG patches can be controlled by segregation time. Figure 6.1f shows a μm-sized graphene patch across several terraces. In addition, some wrinkles appeared on the graphene during cooling process (~ 600 K). The formation of wrinkle structures has been attributed to the different thermal expansion coefficients of graphene and Pt(111) surface [8–10]. The nanobubble structure had also been observed on graphene-Pt(111) system, because of the same reason [11].

We also prepare SLG by chemical vapor deposition (CVD) method. At first, a clean Pt(111) was heated up to 950 K. Then Pt(111) was exposed in ethylene with the pressure of 5.2×10^{-8} mbar. The coverage of SLG can be simply controlled by exposure time of ethylene. Through this route, patch structure and monolayer SLG can be prepared on Pt(111) surface (Figs. 6.1b, c). When monolayer SLG/Pt(111) surface is cooled to room temperature, large-scale wrinkles can be observed as well (Fig. 6.1d). Figure 6.2 shows the XPS C1 s peaks from graphene and O1 s peak from CO on SLG/Pt(111) surface as a function of graphene coverage. We should note that CO exposure was carried out at the partial pressure of 5.2×10^{-9} mbar. XPS and LEEM results illustrate CO molecules do not intercalate into graphene/Pt
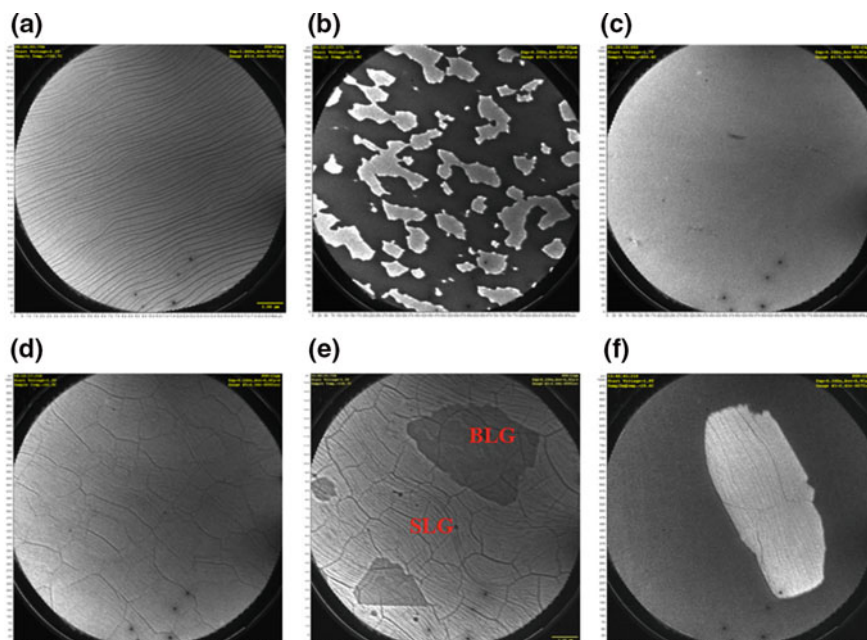
Fig. 6.1 LEEM images of **a** clean Pt(111) surface, **b** sub-monolayer graphene on Pt(111) surface in ethylene doping at 927 K, **c** intact single-layer graphene film at 927 K, **d** graphene film in **c** cooled down to 328 K, **e** bilayer graphene at black area, **f** graphene patch on Pt(111) surface prepared via surface segregation. Imaging condition: **a** 20 μm, 2.1 eV; **b**, **c** 20 μm, 1.7 eV; **d** 15 μm, 1.5 eV; **e** 15 μm, 1.7 eV; **f** 10 μm, 1.8 eV
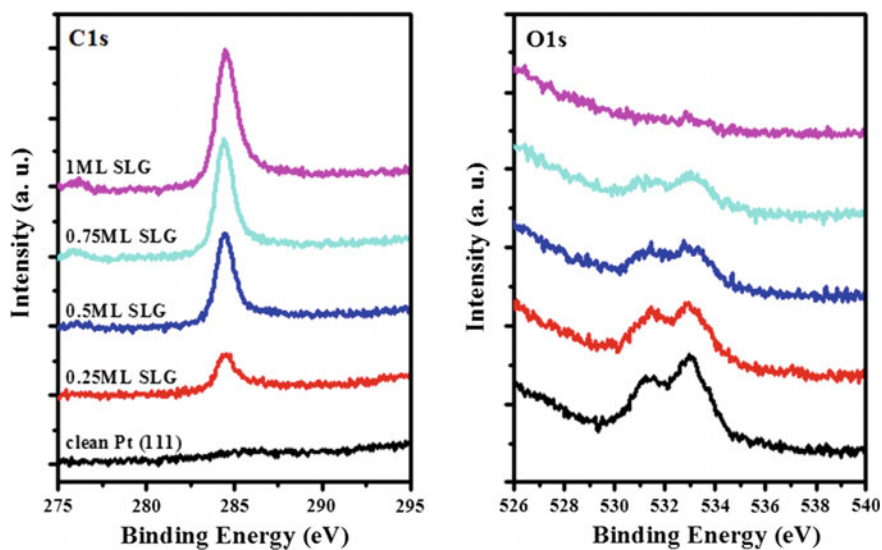
Fig. 6.2 XPS C1 s peak of fresh SLG on Pt(111) surface with various coverages prepared by CVD method (*left*), and O1 s peak of CO adsorbed on SLG/Pt(111) surfaces corresponding to *left* figure in 5.2×10^{-9} mbar CO at room temperature (*right*)

(111) interface at the partial pressure lower than 10^{-8} mbar region. We further show the XPS O1 s peak is negligibly small on monolayer SLG/Pt(111) surface after the exposure of 5.2×10^{-9} mbar CO, indicating CO molecules do not adsorb on graphene surface in UHV condition at room temperature.

At last, bilayer graphene (BLG) structure can be prepared through surface segregation of monolayer SLG/Pt(111) surface at 900–950 K. As shown in Fig. 6.1e, we assign bright area to SLG film and dark areas to BLG patches, respectively.
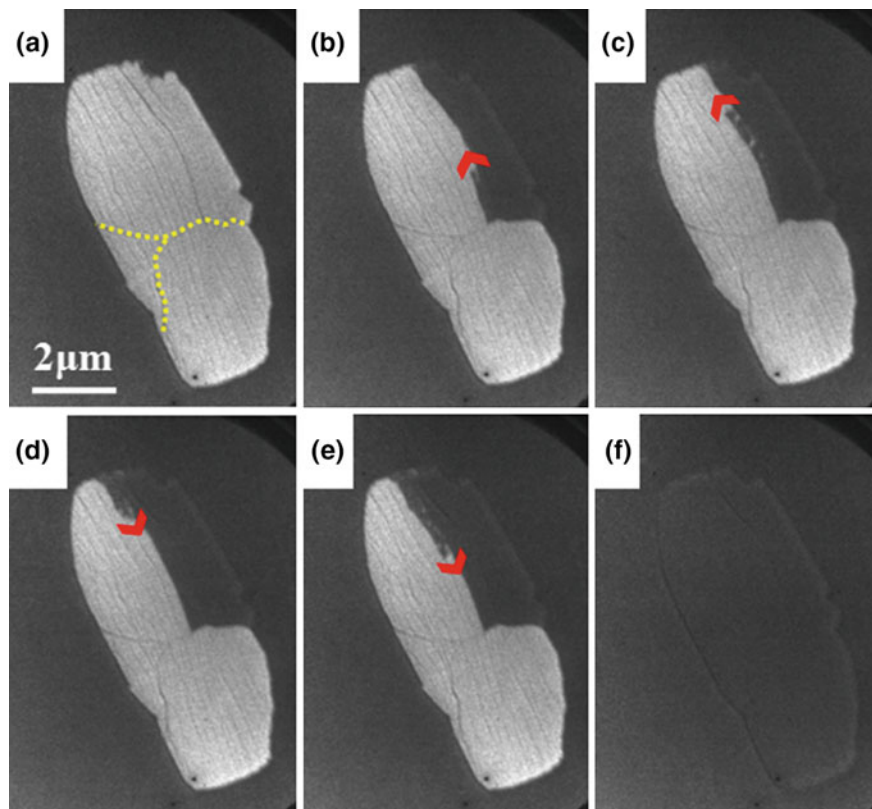
6.3   CO Intercalation

In order to apply the imaging effect of SLG for CO oxidation process on Pt(111), we first need to construct a CO/Pt(111) surface covered by SLG [SLG/CO/Pt(111)]. In principle, this SLG/CO/Pt(111) surface can be achieved by two different processes: (1) prepare a CO/Pt(111) surface, then transfer SLG cover on its top; and (2) prepare SLG/Pt(111) surface and then CO intercalate into graphene-Pt(111) interface. Obviously, the second process is more convenient to carry out in UHV system. In previous studies, the intercalation of H, O, F, Au, and Pb atoms has been found between the graphene–substrate interface [13–17]. In this section, we utilize in situ spectroscopic and real-time microscopic techniques to investigate CO intercalation process on SLG/Pt(111) surface.

As is known to us, CO binds with Pt(111) surface very strongly and its saturated coverage can reach 0.5 ML in UHV condition at room temperature [18]. The SLG/Pt(111) surface in Fig. 6.3a contains bare Pt area (dark) and a SLG patch (bright). In situ LEEM studies show CO start to intercalate into graphene–Pt(111) interface when the pressure of backfilling CO increases to 2.6×10^{-7} mbar.

We find that the CO intercalation darkens the contrast of graphene in LEEM video with a start voltage of 1.8 eV (Fig. 6.3a–f). Dynamical multiple-scattering low-energy electron diffraction theory had revealed the dependence of diffraction electron intensity on start voltage (I–V curve) was determined by the distance between graphene and substrate [7, 19]. Compared to the distance between graphene and Pt(111) ($\sim$3.30 Å), CO molecule has a larger kinetic diameter of 3.76 Å [20, 21]. So the CO intercalation should increase the distance between graphene and Pt(111) surface, resulting in distinct intensity of diffraction electron. In contrast to the I–V curve of fresh SLG/Pt(111) surface, two intensity minima of diffraction electron on CO-intercalated graphene surface are found at 1.8 and 5.5 eV (Fig. 6.4a). With the aid of SLG, we find the CO intercalation and desorption can be visualized by real-time LEEM studies at the start voltage of 1–2.5 and 4–7 eV. However, the I–V curve of CO/Pt(111) surface is similar to that of clean Pt(111) surface (Fig. 6.4b).

More interestingly, a zigzag CO intercalation process is observed from Fig. 6.3b–e. We find CO molecules intercalate from the edge of graphene patch, and then diffuse along Pt step. When the interfacial CO molecules arrive at wrinkles which are vertical to the Pt step direction (yellow dash line in Fig. 6.3a), CO

Fig. 6.3 a–f Consecutive LEEM images of CO intercalation in 2.6×10^{-7} mbar CO atmosphere at room temperature. Imaging condition: Start Voltage (STV) = 1.8 eV. The positions of wrinkles are marked with *yellow dash lines*. Reproduced from Ref. [12] by permission of John Wiley & Sons Ltd

molecules start to diffuse along opposite direction on the next Pt terrace. Subsequently, CO molecules reach another end, i.e., the edge of graphene patch, which tightly binds with Pt via the strong interaction between coordinatively unsaturated edge carbon atoms and substrate [22]. So CO was impelled to opposite direction again on the sequent Pt terrace. Through this zigzag diffusion mode (Fig. 6.5), the entire graphene island appears dark, indicating the interface between graphene and Pt was fully filled with CO molecules (Fig. 6.3f).

To further illustrate the interaction of graphene with Pt(111) surface, the schematic of graphene wrinkle structure is shown in Fig. 6.6a. The convex part of graphene wrinkle is further away from Pt substrate. While the concave is close to Pt and bind with Pt strongly, the concave carbon atoms are bend and sp^2-hybrid [23]. The strong interaction of graphene wrinkle with Pt(111) inhibits CO diffusion and results in a zigzag CO intercalation process. We should note that the CO intercalation
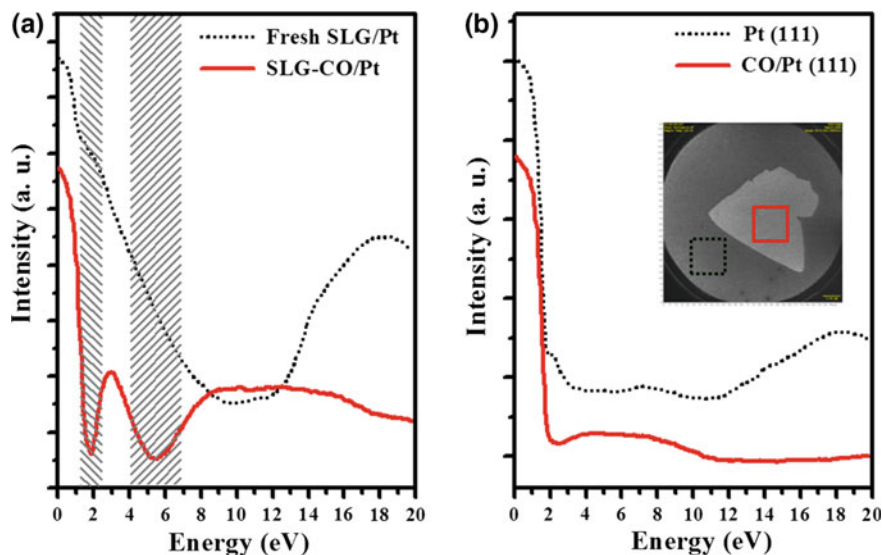
Fig. 6.4 a The dependence of diffraction electron intensity on incident energy from fresh graphene surface (*black dash line*) and CO-intercalated graphene (*red line*); (b) The dependence of diffraction electron intensity on incident energy from bare Pt(111) surface (*black dash line*) and CO/Pt(111) surface (*red line*). The analyzed surface was marked in LEEM image inserted in **b**: *red square*, graphene area *black square*; bare Pt(111) surface. Reproduced from Ref. [12] by permission of John Wiley & Sons Ltd
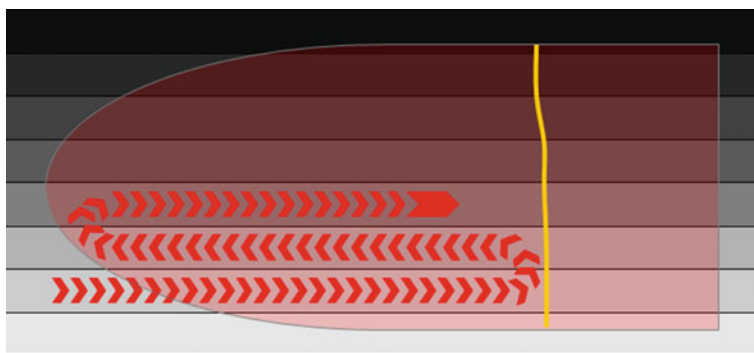
Fig. 6.5   Scheme of the CO intercalation between graphene/Pt(111) interface

has not been observed on monolayer SLG/Pt(111) surface in CO atmosphere with a partial pressure of 2.6×10^{-7} mbar at room temperature (Fig. 6.7).

We also use in situ XPS to investigate CO intercalation process. For comparison, the CO adsorption on clean Pt(111) surface is studied at different CO partial pressures. As shown in Fig. 6.8a, two XPS O1 s peaks from adsorbed CO are found
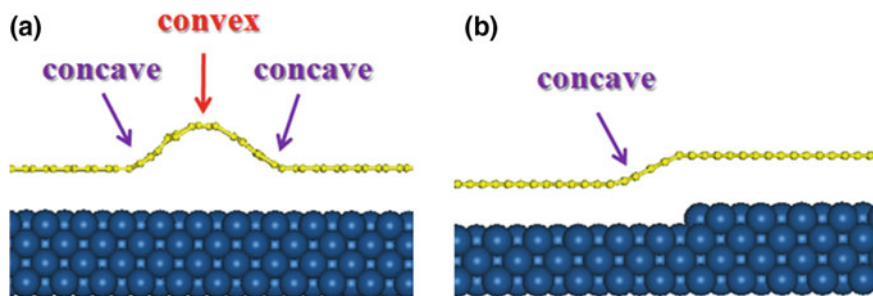
Fig. 6.6 a A scheme showing the concave sites at the edges of a wrinkle, which interact strongly with the substrate and function as barriers for CO diffusion, and the hollow structure under the convex graphene sheet, functioning as a nanosized inlet or outlet for gases. **b** A scheme illustrating the case of putting an atomically continuous graphene sheet on a substrate step; the deformed graphene sheet contains both concave and convex sites
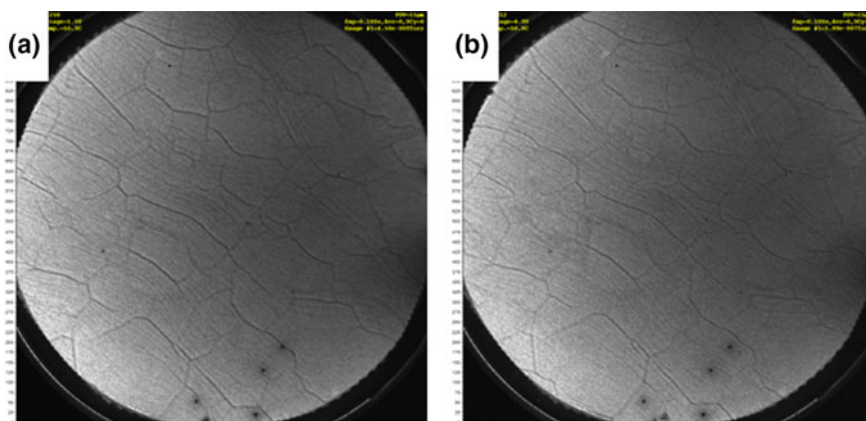

Fig. 6.7 LEEM images of **a** fresh 1 ML SLG/Pt(111) and **b** 1 ML SLG/Pt(111) exposed in 2.6×10^{-7} mbar CO at room temperature for 20 min. Reproduced from Ref. [12] by permission of John Wiley & Sons Ltd

at 531.3 and 533.0 eV, which are from bridging CO and top-CO, respectively [24]. The ratio of bri-CO/top-CO is determined to be 1:1.9. Subsequently, the CO pressure was increased to 5.2×10^{-6} mbar and kept for 15 min. XPS O1 s spectra were acquired in CO atmosphere at a pressure of 5.2×10^{-8} mbar. We find the amount of bridging and top-CO does not change significantly (Fig. 6.8a).

In contrast, both the amount of CO and the ratio of bri-CO/top-CO are distinct on 0.7 ML μSLG/Pt(111) surface in CO atmosphere with different partial pressures. We find the amount of CO adsorbed on 0.7 ML μSLG/Pt(111) is only about 31% of that on clean Pt(111) in CO atmosphere at a pressure of 5.2×10^{-9} mbar (Fig. 6.8a). Since 70% of Pt surface was covered by graphene on 0.7 ML μSLG/Pt
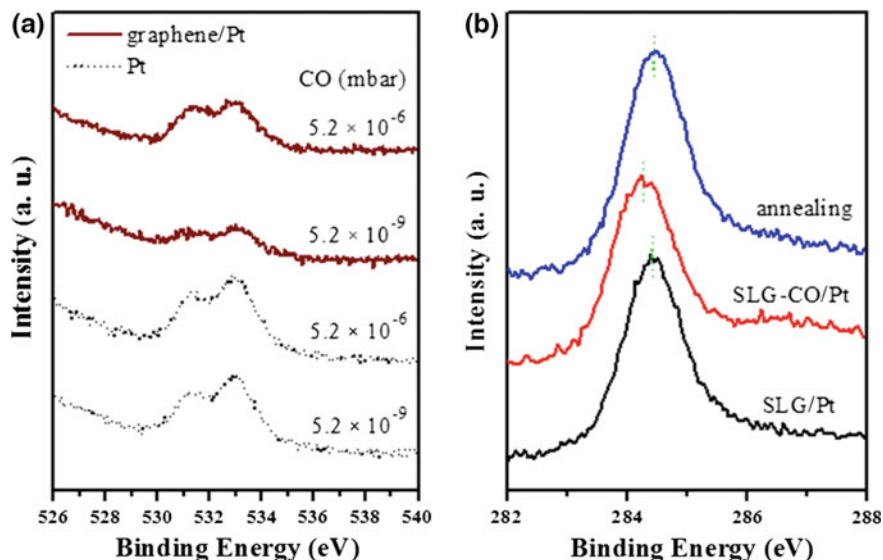
Fig. 6.8 a XPS O1 s peak of CO adsorbed on bare Pt(111) surface and 0.7 ML μSLG/Pt(111) surface in various CO pressures at room temperature; **b** XPS C1 s peak of 0.7 ML μSLG/Pt(111) surface, CO-intercalated single-layer graphene (μSLG-CO/Pt) and μSLG-CO/Pt annealed at 500 K for 2 min. Reproduced from Ref. [12] by permission of John Wiley & Sons Ltd

(111) sample, we infer that CO molecules adsorb on only bare Pt surface area in 5.2×10^{-9} mbar CO atmosphere at room temperature. Subsequently, the partial pressure of CO was increased to 5.2×10^{-6} mbar and kept for 15 min. After that CO pressure was decreased to 5.2×10^{-8} mbar and XPS O1 s spectra was acquired (Fig. 6.8a). Interestingly, we find the amount of CO increases with 3 times when the CO pressure increases from 5.2×10^{-9} mbar to 5.2×10^{-6}, indicating CO molecules intercalate into graphene-Pt(111) interface. We further calculate the amount of CO in graphene-Pt(111) interface. It is found that graphene cover lowers the saturated coverage of CO with 20%. More importantly, the ratio of bri-CO/top-CO was determined to be 1:1.2 under graphene cover. While the ratio of bri-CO/top-CO is 1:1.9 on a clean Pt(111). The graphene cover decreases the ratio of bri-CO/top-CO on Pt. The reason should be attributed to higher steric position of top-CO molecules [25, 26], which makes them less stable under graphene cover.

XPS results show the graphene cover can alter the adsorption geometry of CO on Pt(111). On the other hand, CO intercalation may conversly change the properties of graphene. Previous studies have shown that the strong interaction between graphene and metal substrate induced the binding energy of XPS C1 s peak of graphene to shift higher [27]. The order of the interaction between graphene and metal substrate from weak to strong has been determined to be Pt < Ir < Rh < Ru. Therefore, the binding energy of C1 s peak from graphene is highest on Ru(0001) and lowest on Pt(111). For graphene/Pt(111) system, the charge transfer has been

estimated to be 0.01 e/C from carbon to metal [28]. As shown in Fig. 6.8b, the binding energy of C1 s peak from CO-intercalated graphene is 0.2 eV lower than that of pristine graphene. A similar phenomena has been observed over graphene-SiC system, because of the formation of quasi-free-standing graphene layer after intercalation [17]. But graphene interacts with Pt(111) very weakly, so it is indiscreet to attribute the lower binding energy of C1 s peak to the formation of quasi-free-standing graphene. Furthermore, the electronic interaction of graphene and underneath CO may also induce the binding energy shift of C1 s peak.

In situ LEED with micrometer scale apertures (μ-LEED) was further employed to investigate the local graphene-Pt(111) interaction before and after CO intercalation. As shown in Fig. 6.9a, six satellite diffraction spots were observed around (00) spot, which should be attributed to the interaction of graphene and Pt(111) [8, 29]. After CO intercalation, the satellite diffraction spots disappear, indicating the interaction of graphene and Pt(111) surface is weakened by CO intercalation.

At last, the locally electronic structure of graphene was studied by spatially resolved EELS. Geim and coworkers have found the free-standing graphene film presented a π-plasmon energy loss peak between 4 and 7 eV [30]. Figure 6.10a shows the electronic structure of clean graphene surfaces. The single-layer graphene surface does not present a clear energy loss peak. While a characteristic energy loss peak is observed at 4.5 eV on the bilayer graphene surface, the similar EELS results have been observed on graphene–Ni and graphene–6H-SiC (0001) systems as well [31, 32]. The π electronic structure of single-layer graphene was depressed, because of the direct interaction between graphene and substrate. For bilayer graphene system, the bottom graphene layer direct couples with substrate and thus weakens the interaction between top graphene layer and substrate. So the electronic structure of top graphene layer resembles that of free-standing graphene [31, 32]. Interestingly, we find the CO-intercalated graphene presents an energy loss peak at 4.8 eV, indicating the electronic structure of graphene was healed after CO intercalation (Fig. 6.10b). We should note that the contribution of intercalated CO to this energy loss peak cannot be excluded.
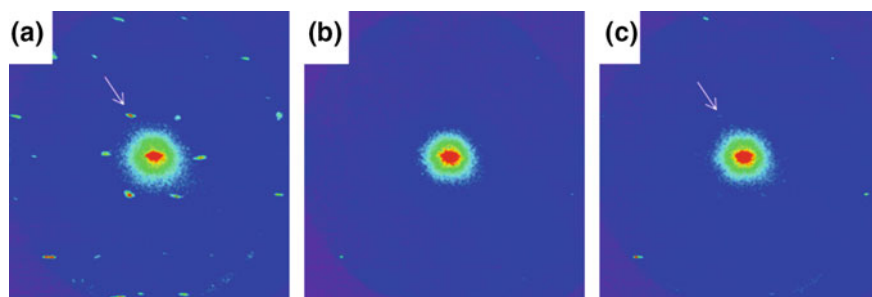
Fig. 6.9 μ-LEED patterns from **a** the μSLG/Pt(111), **b** the μSLG-CO/Pt(111) in CO atmosphere, and **c** the μSLG-CO/Pt(111) kept in UHV and at room temperature. The *arrows* mark the satellite spots due to the Moiré structures of the graphene island. Reproduced from Ref. [12] by permission of John Wiley & Sons Ltd
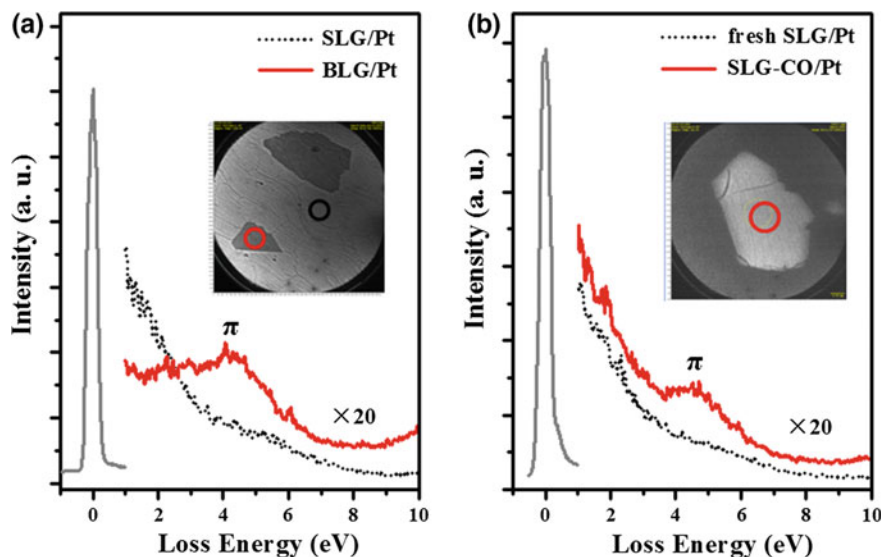
Fig. 6.10 Spatially resolved EELS studies of **a** the area of single-layer and bilayer graphene presented simultaneously, **b** μSLG/Pt(111) and μSLG-CO/Pt(111) surfaces. The incident energy of EELS studies is 20 eV. The marked cycles in inserted LEEM images indicate the analyzing area. Reproduced from Ref. [12] by permission of John Wiley & Sons Ltd

XPS, LEED, and EELS investigations show the "zigzag" CO intercalation alters the electronic properties of single-layer graphene. On the other hand, a graphene cover changes the adsorption geometry of CO molecules on Pt(111) surface.

6.4   The Confinement Effect of Graphene

Graphene has been widely studied and applied in many physical and material science fields. For example, electrons were found to mobilize in graphene-like massless Dirac fermions, which induced quantum phenomena up to room temperature [33, 34]. As a one-atom-thick material, graphene with tiny nanopores was used for speeding up DNA sequencing [35–37]. Furthermore, the design and manufacture of graphene devices also attracted great interests, such as transistors, gas sensors, and touch screen [38–40]. But the application of graphene in chemistry field has been rarely reported, in particular for catalytic reactions, owing to its chemical inertia. In this section, we further show the confinement effect of graphene cover for CO desorption and oxidation on Pt(111).

First, we study the stability of intercalated CO molecules and find they are stable when the partial pressure of CO is higher than 2×10^{-8} mbar at room temperature. Surprisingly, when the backfilling CO is pumped away, part of intercalated CO

molecules desorb from Pt(111) (Fig. 6.11a–c). Real-time LEEM investigations show the bright rows first appear close to wrinkle structures, indicating the wrinkle structures function as outlet for CO outward diffusion to desorb. At elevated temperature in UHV condition, the bright area of CO-intercalated graphene surface increases, indicating more CO molecules desorb from underneath. However, a small amount of dark rows are still observed after UHV annealing at 487 K (Fig. 6.11d). This surface is named as SLG/1D-CO/Pt(111).
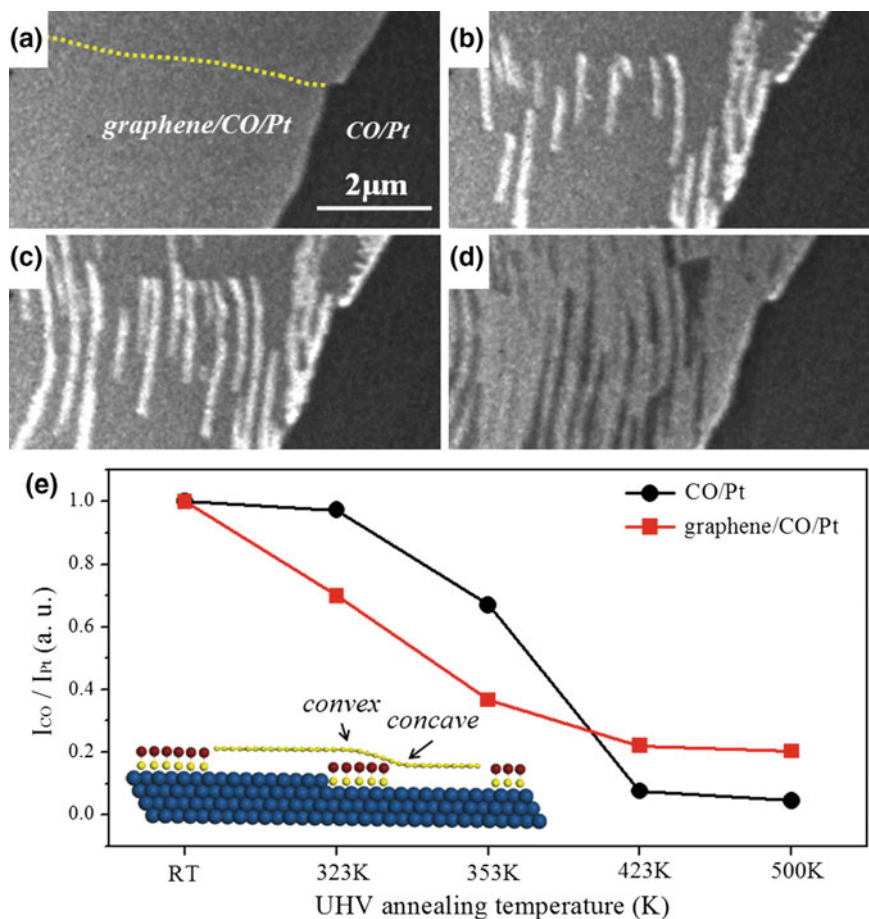
Fig. 6.11 **a–d** A series of LEEM images from the μSLG-CO/Pt(111) surface in UHV and at room temperature for different times. **a**: 0 s; **b**: 200 s; **c**: 302 s; **d**: at 487 K. The start voltage is 2.4 V. The *dashed line* in **a** marks the position of graphene wrinkle. **e**: XPS O1 s intensity from the CO/Pt (111) surface and μSLG-CO/Pt(111) surface annealed at various temperatures in UHV. The O1 s intensity has been normalized by the Pt4f intensity. Each annealing step was kept for 2 min. The inset in **e** shows the desorption of the intercalated CO molecules. Reproduced from Ref. [12] by permission of John Wiley & Sons Ltd
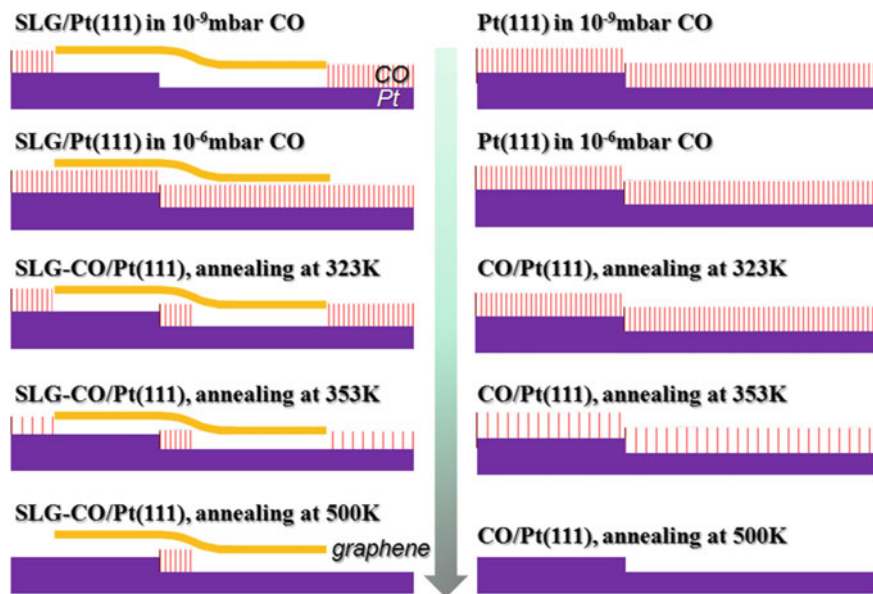
Fig. 6.12 Schemes of μSLG/Pt(111) and clean Pt(111) in CO atmospheres with various partial pressures at room temperature, and then UHV annealing

We also use in situ XPS to study the desorption of intercalated CO at different UHV annealing temperatures. Compared to real-time LEEM/PEEM technique, it is often required several minutes to obtain a decent XPS spectrum. Therefore, in order to avoid the desorption of intercalated CO during characterization, μSLG-CO/Pt (111) surface was first annealed at each temperature for 2 min and then XPS O1 s spectrum was obtained. We note that the CO molecules from both bare Pt area and graphene–Pt interface contribute to XPS O1 s peak on a μSLG-CO/Pt(111) surface. As shown in Fig. 6.11e, the intensity of CO decreases to 70% on μSLG-CO/Pt(111) surface after UHV annealing at 323 K. In contrast, the CO amount does not change significantly on clean Pt(111) after same annealing treatment. So we can infer that the decrease of XPS O1 s peak intensity over μSLG-CO/Pt(111) surface can be attributed to the desorption of CO from graphene–Pt interface (Fig. 6.12). Both LEEM and XPS results indicate the confinement effect of single-layer graphene lowers the desorption temperature of CO on Pt(111), part of CO molecules can desorb from graphene–Pt interface even at room temperature, while the clean Pt is easy to be poisoned by CO molecules at room temperature [41].

To further understand the confinement effect of graphene in destabilizing adsorbed CO, we carried out density functional theory (DFT) calculations with a model consisting of CO molecule in between a (3×3) graphene layer and a $(\sqrt{7} \times \sqrt{7})$ Pt four-layer slab (Fig. 6.13).

The adsorption energies of CO (E_{ad}) at the top and bridge sites are calculated at various graphene–Pt(111) distances ($D_{graphene–Pt}$). At the equilibrium state of fully
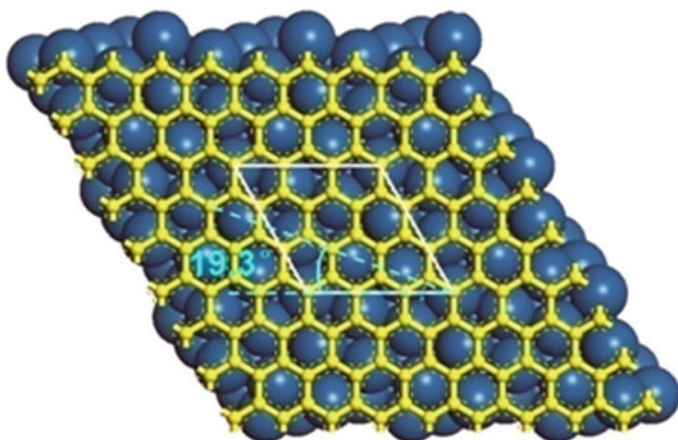
Fig. 6.13 Supercell of graphene on Pt(111), which is denoted by *solid white lines*

relaxed graphene, $D_{graphene\text{-}Pt}$ with CO adsorbed at the top site is 5.91 Å and E_{ad} (t-CO) decreases by 0.06 eV, compared with E_{ad} of CO on bare Pt(111). Moving the graphene cover closer to the substrate leads to even smaller adsorption energies, and the tendency can be clearly described by the dependence of E_{ad} on $D_{graphene-Pt}$ (Fig. 6.14). When CO is located at bridging site, the equilibrium distance between graphene and Pt(111) is 5.30 Å. As the space reduces, CO adsorption on Pt(111) gets even more weakened. For example, E_{ad} (b-CO) is −1.65 eV in the case of $D_{graphene-Pt} = 5.20$ Å. DFT calculations show that CO adsorption on Pt(111) is weakened by the presence of graphene cover. The smaller the nanospace, the lower the adsorption energy of CO. Meanwhile, the confinement effect is stronger on the adsorption of t-CO than b-CO. Therefore, theoretical calculation results agree with experimental observations of the weakened CO adsorption and the change of

Fig. 6.14 Adsorption energies of t-CO on Pt(111) under the cover of graphene at various graphene/Pt(111) interfacial structures. D represents the distance between graphene and Pt surface ($D_{graphene-Pt}$). The freely relaxed D for t-CO corresponds to 5.91 Å. Reproduced from Ref. [12] by permission of John Wiley & Sons Ltd
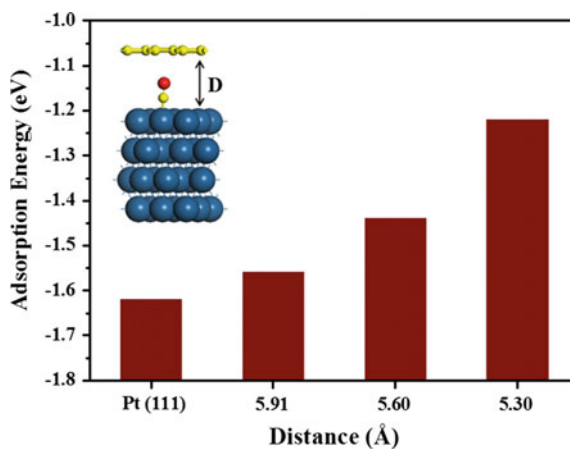
adsorption sites, i.e., from t-CO to b-CO, under the graphene cover. XPS C1 s measurements of graphene show the binding energy shift accompanying CO intercalation (Fig. 6.8b). Accordingly, the electronic interaction between graphene and CO is present, which may be attributed to the confinement effect.

In situ characterizations combined with DFT calculations reveal the confinement effect of graphene lowers the adsorption energy of CO on Pt(111) surface without deeply reducing the active sites of Pt. We find part of CO molecules desorb from Pt (111) surface at room temperature with a graphene cover on top.

On the other hand, XPS results show that 20% of intercalated CO remains on μSLG-CO/Pt(111) after UHV annealing at 500 K. This finding is in a good agreement with the appearance of 1D black CO rows in LEEM images at elevated temperature. In contrast, CO can be removed from clean Pt(111) surface completely at a annealing temperature higher than 420 K [42]. When putting a large-scale graphene film onto Pt(111) surface, carbon atoms close to the steps should get distorted from a planar structure, forming concave and convex regions with nm width (Scheme in Fig. 6.11e). These distorted carbon atoms interact strongly with Pt and act as barriers for outward diffusion of CO to desorb (Fig. 6.12).

In the 2D nanoconfined interface between the graphene cover and flat Pt(111) terraces, the onset for CO desorption is observed at room temperature. We find the binding energy of C1 s peak from graphene shifts higher with 0.2 eV, compared to that from CO-intercalated graphene (Fig. 6.8b). In addition, the Moiré pattern appears again in the μ-LEED study after CO desorption, though it is weaker than the pristine graphene/Pt(111) before CO intercalation (Fig. 6.9c). These indicate the interaction of graphene with Pt(111) somewhat resumes after CO desorption. At the same time, the graphene cover also traps a small amount of intercalated CO close to Pt steps (Fig. 6.12).

Previous works have shown the confinement effect of carbon nanotube could alter the redox properties of metal oxide and also the diffusion of molecules inside the carbon nanotube [43–45]. In this section, we show the confinement effect of graphene cover can alter the adsorption behavior of CO molecules on Pt(111). In the 2D interfacial space confined between graphene cover and flat Pt(111) terraces, the onset temperature for CO desorption is found around room temperature. On the other hand, a small amount of the intercalated CO molecules can be still trapped close to Pt steps at elevated temperature. Combined with the imaging effect of single-layer graphene, we think μSLG/1D-CO/Pt(111) should be a ideally model system for visualizing chemical reaction in confined space.

6.5   In Situ Visualizing Single-Channel Reaction

For comparison, the μSLG-CO/Pt(111) is first exposed in 1.3×10^{-6} mbar O_2 atmosphere at room temperature, and we find CO molecules on bare Pt area and in graphene–Pt interface cannot be eliminated, because the dissociative adsorption of O_2 is inhibited on CO/Pt(111) [41]. However, CO can be removed completely from
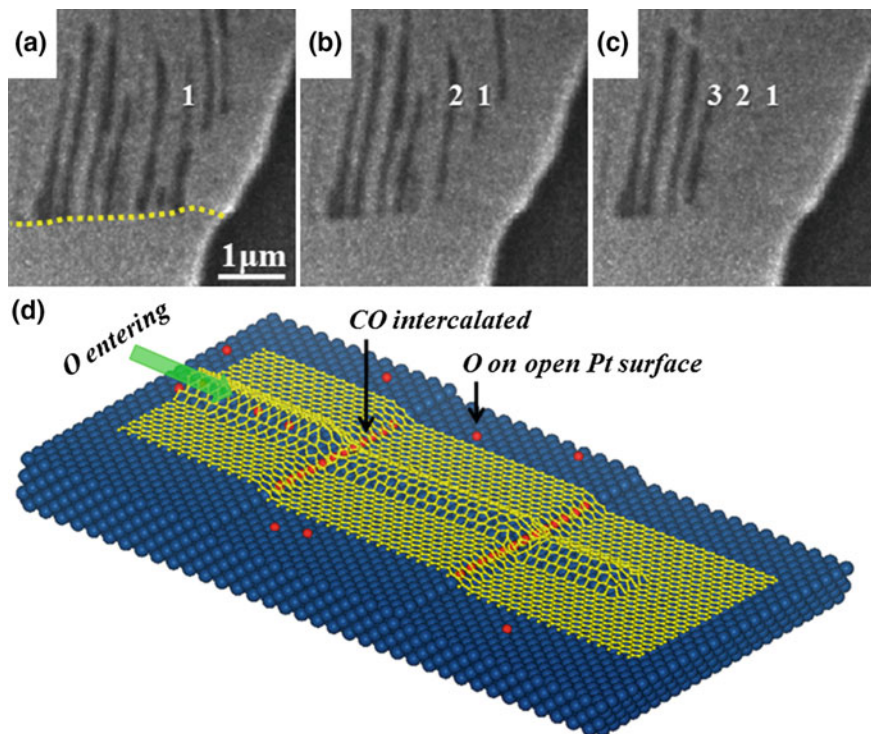
Fig. 6.15   a–c LEEM images of CO oxidation process in confined space in 1.3×10^{-6} mbar O_2 atmosphere at 493 K. **d** The dissociated O atoms on bare Pt(111) surface diffuse into graphene wrinkle and react with intercalated CO molecular under graphene patch. Pt, *cyan*; C, *gray*; O, *red*. Imaging condition: **a** 20 μm, 2.4 eV. *yellow line*: the position of wrinkle. Reproduced from Ref. [12] by permission of John Wiley & Sons Ltd

bare Pt surface after UHV annealing above 423 K. As thus, bare Pt area provide active sites for O_2 dissociative adsorption on μSLG/1D-CO/Pt(111) surface and then react with trapped 1D CO rows under graphene cover.

The CO oxidation reaction on μSLG/1D-CO/Pt(111) is carried out in 1.3×10^{-6} mbar O_2 atmosphere at 493 K (Fig. 6.15). We find the reaction starts from the wrinkles and proceeds along the steps. Again, the graphene wrinkle functions as a nanosized inlet for O_2 to react with the trapped CO molecules close to Pt steps intersecting with the wrinkle. The marginal CO columns are reacted preceding the central ones since the marginal CO has quicker access to O_2 supplied through the wrinkle. After the oxidation at the graphene/1D-CO/Pt(111) surface, XPS measurement was carried out. The results show that the confined CO has been completely eliminated.

With the aid of the imaging effect of single-layer graphene, we study CO oxidation reaction and determine its reaction rate:

$$r = \frac{1}{N} \times \frac{d[CO]}{dt} = \frac{1}{N} \times \frac{\theta dA}{\pi r_{Pt}^2 dt} = \frac{\theta dL}{2 r_{Pt} dt},$$

N   route numbers of CO oxidation reaction (i.e., amount of Pt atoms in the reaction front);
[CO]   amount of intercalated CO;
t   reaction time (s);
A   area of black row;
L   length of black row;
r_{Pt} radius of Pt atom;
θ   coverage of intercalated CO = coverage of CO on bare Pt(111) surface × 80% = 0.4 ML.

As shown in Fig. 6.16, the reaction rate of CO oxidation confined under graphene cover can be determined through plotting the length of a black row as a function of time. In O_2 atmosphere with a partial pressure of 1.3×10^{-6} mbar at 493 K, the reaction rate r = 0.123 × 10^4 × 0.4/2.78 = 177, i.e., 177 CO molecules can be converted to CO_2 one Pt atom per second.

After the oxidation, XPS measurement was carried out. The results show that the confined CO has been completely eliminated. Instead, O1 s peak at 534.4 eV was observed (Fig. 6.17), which may be from the trapped CO_2 [46]. Since CO_2 is typically physisorbed on metals [46, 47], the appearance of CO_2 signals on Pt above
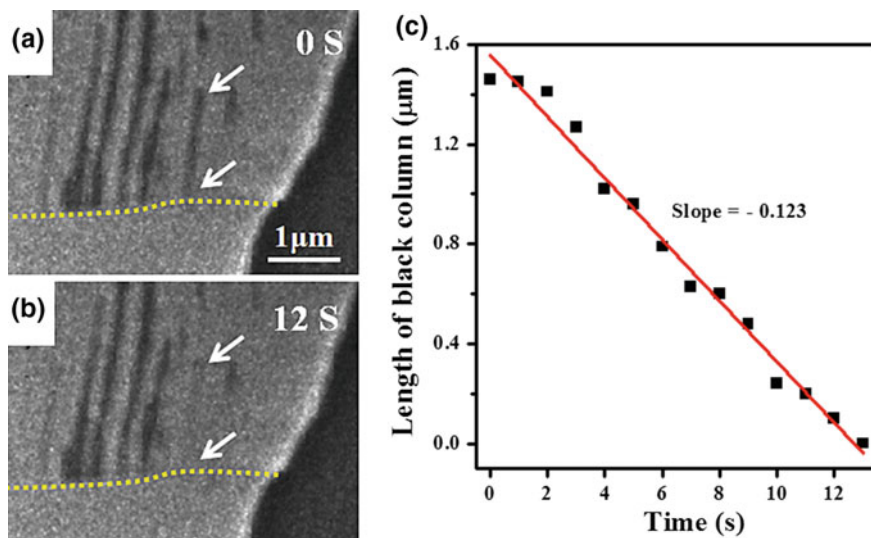
Fig. 6.16 Plots of the *black row* length as the function of reaction time in 1.3×10^{-6} mbar O_2 atmosphere at 493 K. Reproduced from Ref. [12] by permission of John Wiley & Sons Ltd

Fig. 6.17 XPS O1 s spectra of SLG–CO/Pt(111) after oxidation in O_2 atmosphere with partial pressure of 1.3×10^{-6} mbar at 493 K
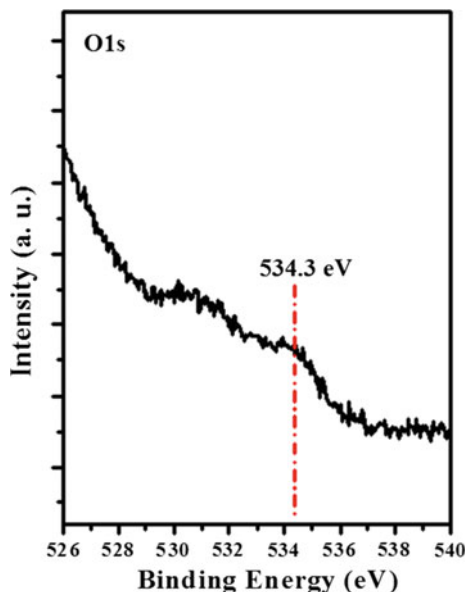
room temperature again indicates the strong geometric confinement effect at the nanospace between the deformed graphene sheet and the surface steps.

6.6 Summary

With the aid of the imaging effect of single-layer graphene, we use real-time LEEM technique to study CO intercalation, desorption, and oxidation processes on Pt(111) surface. Combined with other spectroscopic characterizations, the confinement effect of graphene cover on surface chemical reactions is found.

1. The edges of the graphene patches and the wrinkles strongly interact with Pt and act as barriers for CO diffusion, resulting in the zigzag intercalation of CO.
2. In the 2D interfacial space between graphene cover and flat Pt terraces, top-sited CO becomes less favorable.
3. The confinement effect of graphene cover significantly lowers the desorption temperature of intercalated CO, while a small amount of CO close to Pt steps can be trapped by graphene.
4. Graphene wrinkles function as nano-outlet for CO desorption and nano-inlet for O_2 inward diffusion.

In this chapter, we show the graphene cover exhibits a strong confinement effect on chemistry of molecules underneath. The 2D interfacial space between graphene cover and catalysts surface provides an intriguing confinement environment for surface chemistry and heterogeneous catalysis.

References

1. Vogel D et al (2011) Mapping the local reaction kinetics by PEEM: CO oxidation on individual (100)-type grains of Pt foil. Surf Sci 605(23–24):1999–2005
2. Kim M et al (2001) Controlling chemical turbulence by global delayed feedback: pattern formation in catalytic CO oxidation on Pt(110). Science 292(5520):1357–1360
3. Ertl G (2008) Reactions at surfaces: from atoms to complexity (Nobel Lecture). Angewandte Chemie-Int Ed 47(19):3524–3535
4. Hannon JB et al (2006) The influence of the surface migration of Gold on the growth of Silicon nanowires. Nature 440(7080):69–71
5. Yim CM et al (2008) Low-energy electron microscopy of CO/Pt(111) surface diffusion by nonequilibrium coverage profile evolution. Phys Rev B 78(15)
6. Altman MS, Chung WF, Liu CH (1998) LEEM phase contrast. Surf Rev Lett 5(6):1129–1141
7. Sutter PW, Flege JI, Sutter EA (2008) Epitaxial Graphene on Ruthenium. Nat Mater 7 (5):406–411
8. Sutter P, Sadowski JT, Sutter E (2009) Graphene on Pt(111): growth and substrate interaction. Phys Rev B 80(24):245411
9. N'Diaye AT et al (2009) In situ observation of stress relaxation in Epitaxial Graphene. New J Phys 11:113056
10. Loginova E et al (2009) Defects of Graphene on Ir(111): rotational domains and ridges. Phys Rev B 80(8):085430
11. Levy N et al (2010) Strain-induced pseudo-magnetic fields greater than 300 Tesla in Graphene Nanobubbles. Science 329(5991):544–547
12. Mu R et al (2012) Visualizing chemical reactions confined under Graphene. Angew Chem Int Edit 51(20):4856–4859
13. Sutter P, Sadowski JT, Sutter EA (2010) Chemistry under cover: tuning Metal-Graphene interaction by reactive intercalation. J Am Chem Soc 132(23):8175–8179
14. Huang L et al (2011) Intercalation of metal islands and films at the interface of epitaxially grown Graphene and Ru(0001) surfaces. Appl Phys Lett 99(16)
15. Riedl C et al (2009) Quasi-free-standing Epitaxial Graphene on SiC obtained by hydrogen intercalation. Phys Rev Lett 103(24):246804
16. Oida S et al (2010) Decoupling Graphene from SiC(0001) via oxidation. Phys Rev B 82 (4):041411
17. Wong SL et al (2011) Quasi-free-standing Epitaxial Graphene on SiC (0001) by Fluorine intercalation from a molecular source. ACS Nano 5(9):7662–7668
18. Kinne M et al (2002) Kinetic parameters of CO adsorbed on Pt(111) studied by in situ high resolution X-ray photoelectron spectroscopy. J Chem Phys 117(23):10852–10859
19. Blum V, Heinz K (2001) Fast LEED intensity calculations for surface crystallography using Tensor LEED. Comput Phys Commun 134(3):392–425
20. Baker RW 2004 Membrane technology and applications, 2nd ed. Wiley
21. Predescu L, Tezel FH, Chopra S (1996) Adsorption of Nitrogen, Methane, Carbon Monoxide, and their binary mixtures on Aluminophosphate molecular sieves. Adsorption 3(1):7–25
22. Lacovig P et al (2009) Growth of dome-shaped Carbon Nanoislands on Ir(111): the intermediate between carbidic clusters and quasi-free-standing Graphene. Phys Rev Lett 103 (17):166101
23. Feibelman PJ (2008) Pinning of Graphene to Ir(111) by Flat Ir Dots. Phys Rev B 77 (16):165419
24. Kinne M et al (2004) Coadsorption of D_2O and CO on Pt(111) studied by in situ high-resolution X-ray photoelectron spectroscopy. Langmuir 20(5):1819–1826
25. Wang JX et al (2005) Adsorbate-geometry specific subsurface relaxation in the CO/Pt(111) system. J Phys Chem B 109(1):24–26
26. Lynch M, Hu P (2000) A density functional theory study of CO and atomic oxygen chemisorption on Pt(111). Surf Sci 458(1–3):1–14

27. Preobrajenski AB et al (2008) Controlling Graphene corrugation on lattice-mismatched substrates. Phys Rev B 78(7):073401
28. Khomyakov PA et al (2009) First-principles study of the interaction and charge transfer between Graphene and Metals. Phys Rev B 79(19)
29. Gao M et al (2010) Tunable interfacial properties of Epitaxial Graphene on metal substrates. Appl Phys Lett 96(5)
30. Eberlein T et al (2008) Plasmon spectroscopy of free-standing Graphene films. Phys Rev B 77 (23):233406
31. Sun JB et al (2010) Spatially-resolved structure and electronic properties of Graphene on Polycrystalline Ni. ACS Nano 4(12):7073–7077
32. Langer T et al (2009) Graphitization process of SiC(0001) studied by electron energy loss spectroscopy. Appl Phys Lett 94(11)
33. Zhang YB et al (2005) Experimental observation of the quantum hall effect and Berry's phase in Graphene. Nature 438(7065):201–204
34. Novoselov KS et al (2007) Room-temperature quantum hall effect in Graphene. Science 315 (5817):1379
35. Schneider GF et al (2010) DNA translocation through Graphene Nanopores. Nano Lett 10 (8):3163–3167
36. Siwy ZS, Davenport M (2010) Nanopores Graphene opens up to DNA. Nat Nanotechnol 5 (10):697–698
37. Postma HWC (2010) Rapid sequencing of individual DNA molecules in Graphene Nanogaps. Nano Lett 10(2):420–425
38. Meric I et al (2008) Current saturation in zero-bandgap, topgated Graphene field-effect transistors. Nat Nanotechnol 3(11):654–659
39. Farmer DB et al (2009) Utilization of a buffered dielectric to achieve high field-effect carrier mobility in Graphene transistors. Nano Lett 9(12):4474–4478
40. Fowler JD et al (2009) Practical chemical sensors from chemically derived Graphene. ACS Nano 3(2):301–306
41. Yeo YY, Vattuone L, King DA (1997) Calorimetric heats for CO and Oxygen Adsorption and for the catalytic CO oxidation reaction on Pt(111). J Chem Phys 106(1):392–401
42. Hellman A, Klacar S, Gronbeck H (2009) Low temperature CO Oxidation over supported ultrathin MgO films. J Am Chem Soc 131(46):16636–16637
43. Pan XL, Bao XH (2011) The effects of confinement inside Carbon Nanotubes on catalysis. Acc Chem Res 44(8):553–562
44. Castillejos E et al (2009) An efficient strategy to drive Nanoparticles into Carbon Nanotubes and the remarkable effect of confinement on their catalytic performance. Angew Chem Int Edit 48(14):2529–2533
45. Pan XL et al (2007) Enhanced Ethanol production inside Carbon-Nanotube reactors containing catalytic particles. Nat Mater 6(7):507–511
46. Atkinson SJ, Brundle CR, Roberts MW (1974) Ultraviolet and X-Ray photoelectron-spectroscopy (UPS and XPS) of CO, CO_2, O_2 and H_2O on Molybdenum and gold-films. Faraday Discuss 58:62–79
47. Kiss J, Revesz K, Solymosi F (1988) Photoelectron spectroscopic studies of the adsorption of CO_2 on Potassium-Promoted Rh(111) surface. Surf Sci 207(1):36–54

Chapter 7
Conclusions

This thesis focuses on the correlation between the structure and CO oxidation reactivity of Pt–Ni bicomponent catalysts from model catalytic systems to supported nanoparticle catalysts. In addition, with the aid of the imaging effect of single-layer graphene, the CO intercalation, CO desorption, and CO oxidation processes are investigated on Pt(111) surface.

1. First, we construct and study the catalytic properties of various Ni–Pt(111) model surfaces. We find the sandwich-like structure which consists of surface NiO_{1-X} and subsurface Ni performs best CO oxidation reactivity. The surface NiO_{1-X} provides active sites for O_2 dissociatively adsorption. The subsurface Ni lowers the barrier for CO+O elemental reaction. As thus, the synergetic effect of surface NiO_{1-X} and subsurface Ni promotes CO oxidation on Pt. The effect of reduction temperature on the surface structure and reactivity of catalysts has often been overlooked. In our studies, we show the surface structure of Pt–Ni/CB nanoparticles can be simply modulated by reduction temperatures. The XANES investigations combined with ICP measurements indicate that the high reduction temperature can induce more Ni diffuse inwards. Upon the reduction at 523 K, the sandwich-like structure with half Ni on the surface and another half Ni inside the nanoparticle can be formed, which shows high CO oxidation reactivity.

2. We also show that the cycling oxidative and reductive treatments at variable temperatures can reversibly alternate the surface structure and reactivity of Pt–Ni bicomponent catalysts. Low temperature (~ 423 K) oxidation of Pt-skin structure [Pt/Ni/Pt(111)] induces part of Ni diffuse outwards and form NiO on surface. After further oxidation at a higher temperature of 623 K, the catalysts are completely encapsulated by NiO. When the Pt@NiO core–shell structure is reduced at low temperature (~ 423 K), part of Ni starts to diffuse inwards. Upon the reduction at a high temperature of 623 K, the formation of Pt-skin surface is observed. The catalysts pretreated at low temperatures show high CO oxidation

reactivity due to the formation of the sandwich-like structure with surface and subsurface Ni species.

3. We compare the reactivity and stability of Pt–Fe and Pt–Ni catalysts. The interfacial confinement effect results in the formation of monolayer-thick FeO_{1-X} and NiO_{1-X} nanoislands on Pt(111). The edge structures of the FeO_{1-X} and NiO_{1-X} nanoislands provide the active sites for O_2 dissociatively adsorption, and thus promote CO oxidation reaction. But the stabilities of FeO_{1-X}/Pt (111) and NiO_{1-X}/Pt(111) systems are different after the oxidation at 473 K with a O_2 partial pressure of 1.3×10^{-6} mbar. FeO_{1-X} nanoislands are oxidized to O–Fe–O trilayer structure after oxidation, while the chemical state of NiO_{1-X} is unchanged after same oxidative treatment. The result of model catalytic systems is well consistent with the observation of supported Pt–Fe/CB and Pt–Ni/CB catalysts. In situ XANES investigations show the chemical state of Fe is 2+ under CO oxidation with excess H_2, whereas the Fe is further oxidized in O_2−rich atmosphere. In contrast, the chemical state of Ni is constant under H_2−rich and O_2−rich CO oxidation conditions. Therefore, the CO conversion increases over Pt–Ni/CB catalyst when the concentration of O_2 is increasing.

4. By employing real-time microscopic techniques, the confinement effect of single-layer graphene on the chemistry of CO/Pt(111) system is studied. We find that the CO molecules can easily intercalate between graphene and Pt(111) even under UHV condition at room temperature. Interestingly, CO desorbs from the interfacial space between graphene and Pt(111) around room temperature. In contrast, the desorption temperature of CO from bare Pt(111) is ∼420 K. DFT calculations show the adsorption energy of CO on Pt(111) is decreased by the confinement effect of graphene on top. Furthermore, the dynamic process of CO oxidation is also studied. We find that the graphene wrinkles act as the reaction channels for CO desorption, CO oxidation processes.